POLITECNICO DI TORINO

Master's Degree in Aerospace Engineering

Politecnico di Torino

SIEMENS energy

Master's Degree Thesis

Experimental investigation of heat transfer in additive manufactured channels with different Prandtl

Supervisors

Prof. Andrea FERRERO

Ph.D. Mats KINELL

Candidate

Aaron BRUGNERA

October 2024

Summary

Additive manufacturing of metal alloys allows to create completely new designs for components that require to be actively cooled, such as gas turbines. The parts can now be printed with an uniform and distributed pattern of internal microchannels, leading to a better heat exchange. These channels, however, present a roughness pattern different from the one observed on conventionally manufactured channels, and this changes the flow behaviour in terms of pressure drop and heat exchange performance. This thesis aims to study the different behaviour of AM-manufactured channels and the impact that their relative roughness has on two adimensional parameters: *Darcy friction factor* for the pressure losses and *Nusselt number* for the heat exchange performance. The fluid used was distilled water, which allowed to test at various *Prandtl* numbers by changing its temperature.
This test rig concept started two years ago, and the procedures and theoretical models have been improved by each student. In September 2023, a new model has been developed to gather more accurate results, using the Joule effect to internally generate heat in the metallic test object. An important part of the work has been creating a numerical model to estimate the heat transfer coefficient at the interface between the wall and the water, using *Siemens Star CCM+* thermal and electrical solvers.
The pressure loss results resemble what is already found in literature for conventional sand-grain roughness on the *Moody diagram*. The Nusselt number is affected in a different way, and the different roughness type has different results when compared to previous sand-grain correlations. Another different phenomenon observed is the effect of the Prandtl number, not following previous correlations such as *Dittus-Boelter*.

Keywords: Heat transfer, Additive Manufacturing, Friction Factor, Microchannels, Surface Roughness, Selective Laser Melting, Water

Summary

La fabbricazione additiva per leghe metalliche permette la realizzazione di nuove geometrie per componenti che richiedono il raffreddamento attivo, come le turbine a gas. I componenti possono essere realizzati con una rete interna di micro-canali, i quali permettono un migliore e più uniforme scambio termico. Questi canali, però, hanno una rugosità superficiale differente dai canali realizzati con macchinari tradizionali, e questo cambia il comportamento del flusso, in particolare le perdite per caduta di pressione e lo scambio termico. L'obiettivo di questa tesi è studiare questo comportamento differente nei canali stampati in 3D e l'influenza che la loro rugosità relativa ha su due parametri adimensionali: il *Darcy friction factor* per le cadute di pressione e il numero di *Nusselt* per le prestazioni di scambio termico. Il fluido impiegato è stato acqua distillata, la quale ha permesso di effettuare test al variare del numero di *Prandtl* semplicemente cambiandone la temperatura.
Questo studio è iniziato due anni fa ed è stato progressivamente migliorato dai precedenti studenti sia dal lato teorico che dal lato sperimentale. A settembre 2023 è stato sviluppato un nuovo set up sperimentale per ottenere risultati più accurati, utilizzando l'effetto Joule per generare il calore internamente al provino metallico. Una parte importante di questo lavoro è stata il creare un modello numerico per stimare il coefficiente di scambio termico tra la parete interna e l'acqua, utilizzando i solver termici ed elettrici dentro *Siemens Star CCM+*.
Le perdite di pressione ottenute sono paragonabili ai risultati trovati per la convenzionale rugosità sand-grain, vista nel *diagramma di Moody*. Il numero di Nusselt, invece, si comporta in maniera differente da quanto studiato per la rugosità sand-grain. Un altro comportamento differente è l'effetto del numero di Prandtl, il quale non segue correlazioni come la più comune di *Dittus-Boelter*.

Keywords: Trasmissione del calore, Fabbricazione additiva, Perdite di carico, Micro canali, Rugosità superficiale, Selective Laser Melting, Acqua

Table of Contents

List of Tables

List of Figures

Acronyms

AM
: Additive Manufacturing

CNC
: Computer Numerical Control

htc
: Heat Transfer Coefficient

f_d
: Darcy friction factor

ε
: Relative Roughness

FDM
: Fused Deposition Modeling

Nu
: Nusselt Number

PBF
: Powder Bed Fusion

Pr
: Prandtl Number

qSSHT
: quasi-Steady State Heat Transfer

Re

Reynolds Number

RMS

Root Mean Square

SLM

Selective Laser Melting

SLS

Selective Laser Sintering

TC

Thermocouple

TO

Test Object

Chapter 1

Introduction

Injection molding is still the most popular method when it comes to manufacturing plastic parts on an industrial scale. The basic principle consists of injecting a molten polymer into a cavity inside a mold and then waiting for it to solidify when cooled down. The most crucial part is the cool down, which can take up to 50% of the total production time. Because of these reasons, the molds have to be designed with internal cooling channels for keeping the temperature as uniform as possible [1]. These channels are difficult to manufacture in a conventional way (usually done by drilling the mold) because they have to follow the shape of the plastic parts. This problem is exacerbated if the part is larger or if it has complex geometrical features, where the cooling channels cannot be properly drilled into the mold.
A possible solution found is by using Additive Manufacturing for creating the metallic molds, e.g. using Selective Laser Melting (SLM). When using SLM it is possible to add features at the printed mold, like internal cooling channels instead of drilling them. This innovative design is called "Conformal Cooling Channel (CCC)", because these channels can follow the manufactured part's geometry closer than the traditional ones; the cooling is based on smaller channels uniformly distributed, instead of some bigger ducts. The improvement in cooling can be seen from figure 1.1: the temperature of the part is more evenly distributed and its temperature range is much smaller, drastically reducing the temperature gradients and thus the warping effects on the finished product, which could break during cooling.
When looking at the thermal exchange performance of a component, the SLM printed parts are different from machined ones, mainly because they have higher surface roughness and lower thermal and electrical conductivity. The roughness is a positive aspect because it anticipates the turbulent transition of the flow regime, allowing better thermal mixing in the fluid. Another positive feature is that higher roughness equals to a larger contact surface with the fluid, compared to the smooth channel, which also is an improvement to the convective heat exchange. The drawback of the roughness is a higher friction factor, that brings a bigger

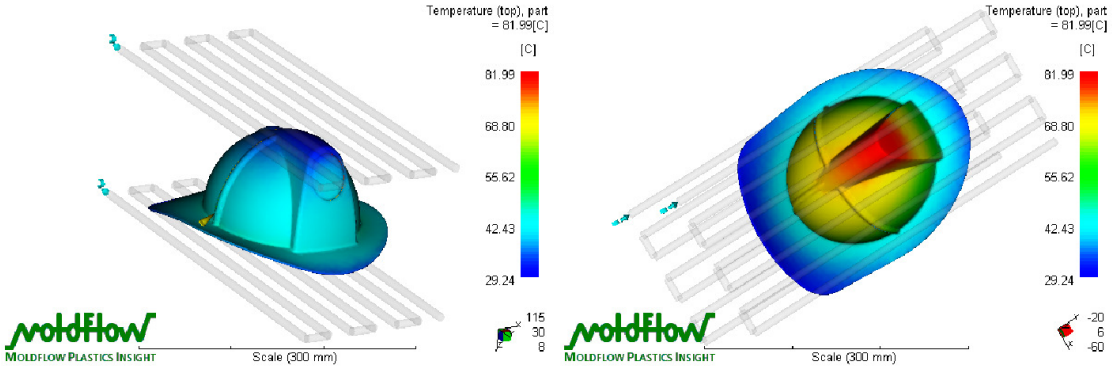

(a) Conventional channel design

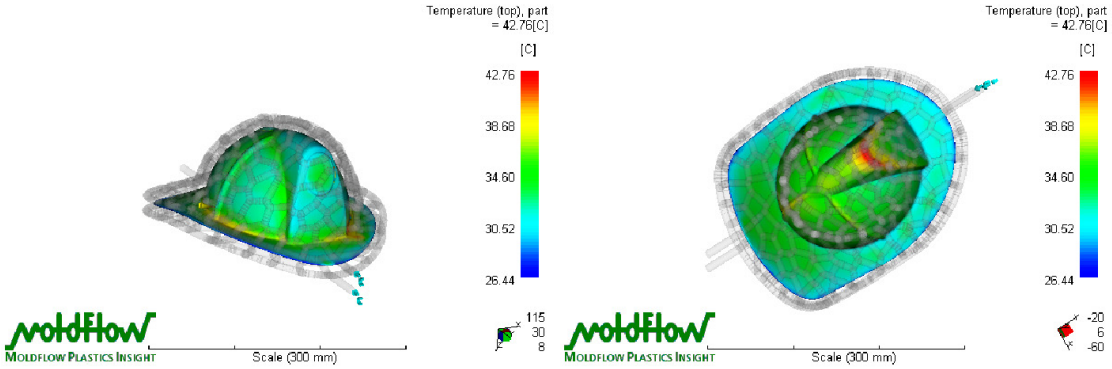

(b) Channels generated by our approach

Figure 1.1: Example of conformal cooling applied to injection molding [2]

pressure drop. This might require a more powerful pump to move the same mass flow around the cooling circuit.

1.1 Previous work

Siemens Energy AB in Finspång (Sweden) has profound experience with additive manufacturing, and now it is investigating how much the AM roughness is affecting the heat exchange and the pressure drop. In 2022 Linda Yang designed a test rig to investigate this phenomenon for her Master's Thesis, using a heated copper block to warm up the test object at the external radius via thermal conduction. The TO then transmits the heat to the water flow at the channel's inner radius; the difference in temperature and pressure drop are then recorded and further analyzed.
In 2023 Luca Cozzarolo discovered that the setup was having too much uncertainty due to the thermal contact resistance between copper and the TO being of the same order of magnitude as the resistance between the TO and the water, so he tried

different test methodologies until he applied the *Joule Heating* method. The rig works by flowing deionized water inside the test channels. These metal components are heated by the Joule effect thanks to an electrical current flowing into them: this energy is then transmitted into the water via convection. By measuring the pressure and temperature difference of the water and the external wall temperature distribution, it is possible to evaluate both the Nusselt number and the Darcy friction factor at the same time.

1.2 Project goals

The target of this work is to evaluate the effect that additive manufacturing production has on cooling channels, regarding thermal and hydraulic performance. AM technology offers an easy way to produce complex parts, but the main drawbacks are poorer surface quality and lower thermal conductivity of the part. Because of these differences from conventionally machined parts, new correlations have to be developed to better mimic the behavior of AM channels. The focus on this thesis' dissertation is on how the effect of the Prandtl number changes with these new manufacturing techniques.

1.3 Limitations

This work has encountered some issues that changed the initial plans for gathering the desired results:

- Research to build a more accurate numerical model for the experiment: the previous model was created in a short time, assigning a fixed heat loss on the copper clamps and a constant heat transfer coefficient along the channel. A new loss model has been implemented to fit better the rig behavior.

- New testing methodology: the Joule Heating rig was developed one month before the start of this work, therefore there were new phenomena like the electrical contact resistance between solids that were not known yet.

- The whole work was 7 months long, with one month of overlap with the previous student and one with the next one. This factor has limited the amount of channels that were possible to test.

- The hydraulic diameter of the test object has been measured via microscope pictures of the inlet/outlet. This method does not account for clogging or different internal geometries due to the SLM manufacturing.

- The surface roughness has been measured on a clipped sample of the TO using a contact stylus. Roughness on SLM components is strongly 3-dimensional, so it is better to use more appropriate tools.
- Only one profilometer test per material has been performed, and only one parameter has been used to describe the relative roughness of the channels. A comparison between different parameters has to be performed.

1.4 Literature Review

The flow behavior inside channels is severely affected by the wall's roughness, impacting the boundary layer development and the transition point between laminar and turbulent flow. The first part of the review focuses on the status of the research about flow development in a rough channel, and the second part is a review of the heat exchange performance.

1.4.1 Flow behavior

The study of surface roughness in channels has started more than a century ago. Initially, the studies were focused on the flow characteristics, like the results obtained by Hagen [3] and Darcy [4]. They concluded that there is a relation between surface roughness and pressure drop, indicating a higher drag in rough pipes when compared to smooth ones. Stanton [5] found out that the flow in rough pipes follows a law of similarity. Based on these investigations, Nikuradse [6] studied the pressure losses, recreating various roughnesses by using circular test channels with different sizes of sand grains lacquered to the wall. To compare his results he used a similarity parameter called *relative roughness* k/r, where k in this case is the sand grain's size and r is the channel's internal radius. This relative roughness is still being used today in a similar way, for example R_z/d_h, where R_z is the maximum peak to valley height of the surface and d_h is the hydraulic diameter of the channel. He found a sudden variation of the friction factor in the transition region, when the boundary layer starts to become turbulent. With Nikuradse's experimental results, Von Karman [7] developed a correlation between the friction factor defined by Darcy and the pipe roughness in a fully turbulent flow regime. This correlation has been used in the Colebrook-White equation [8] and Cheng's formula [9] to describe the effect that roughness and Reynolds numbers have on the friction factor. A rough channel in a turbulent flow condition has an initial decrease of the friction factor, until a certain Reynolds number where the friction factor f_d stays constant with the Re. Moody [10] grouped in a diagram the results. It is a log-log graph with Re on the x-axis and f_d on the y-axis. There is a second y-axis indicating the relative roughness of the pipe, which influences directly the

friction factor when the flow is fully turbulent.
Schlichting [11] linked other types of roughnesses that can be encountered in final components' surfaces (e.g. rivet joints) with the sand-grain results of Nikuradse, and found out that the previous results can still be applied. Huang et al. [12] experimented on channels with high relative roughness, and found out that they behave differently than the Moody diagram:

- The transition from laminar to turbulent starts at an earlier Re when the roughness is higher than a certain threshold;
- There is a deviation in the laminar flow from the theoretical line. It is a quadratic function of the relative roughness.

Dai et al. [13] confirmed these results and suggested a threshold of $R_z/d_h = 1\%$ for separating "smooth" channels and rough micro-channels.

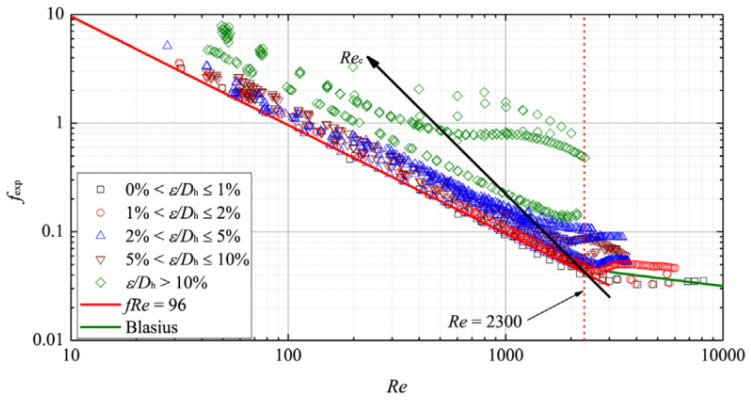

Figure 1.2: Dai's friction factor results on rectangular channels, with different relative roughness [13]

1.4.2 Heat transfer

Cope [14] was one of the first to study heat transfer in rough pipes, using water as a medium, and evaluating the enhancement obtained when comparing with smooth specimens. The design that he chose was made to enhance as much as possible heat transfer, so it was not mimicking realistic pipe roughness geometries.
Dipprey and Sabersky [15] experimented using sand grain roughness and obtained both friction factor and heat transfer results, testing at high Re and different Pr, using distilled water as medium. The result has been an heat transfer enhancement of 270%, when compared to smooth channels. They also made a first tentative on correlating surface roughness with heat transfer performance, using a similar

methodology that Nikuradse used with the friction factor.
Channels with a hydraulic diameter smaller than 1mm are called "Microchannels". Their small size makes the fluid inside them behave differently from the conventional channels, due to the higher relative roughness.
In 2004, Morini [16] reviewed the current knowledge of how heat is exchanged between fluid flow and a rough pipe and found inconsistent results: the experimental data obtained was differing with the conventional theory and different tests were giving discrepant results.
Pennsylvania State University recently accomplished several studies ([17], [18], [19]) on friction factor and heat transfer of SLS (Selective Laser Sintering) cooling channels. They have found a significant increase in Darcy friction factor for the printed test channels, but this was not proportional to the increase in heat transfer performance. Penn State work defined its test specimens roughness using the

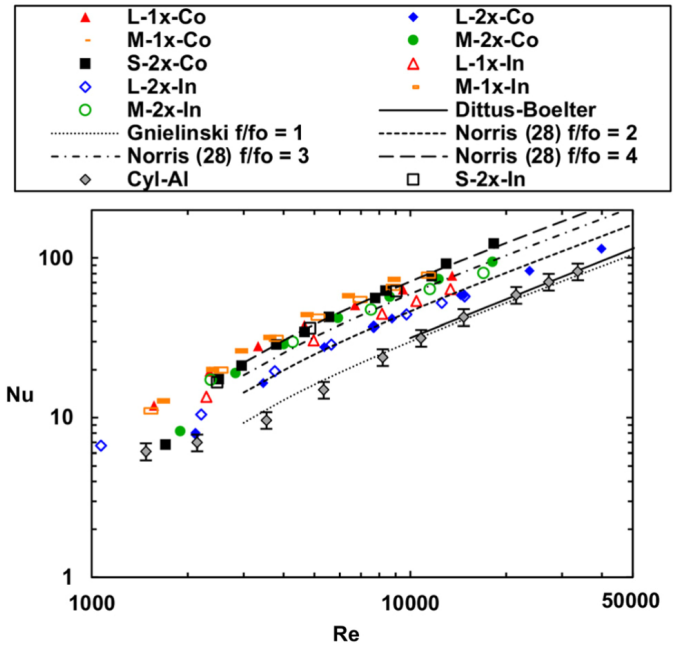

Figure 1.3: Stimpson et al. Nusselt results on rectangular channels with changing relative roughness [18]

arithmetic mean R_a; this has been chosen to be the closest to Nikuradse's sand-grain roughness definition. Townsend et al. [20] and Han et al. [21], however, found out that the arithmetic mean is not the best method to describe the surface finish of AM components. The parameter that suited best the condition in their study is the mean roughness depth (R_z).

Chapter 2

Theoretical background

This chapter extends the previous literature review, focusing on the phenomena required to understand the thesis' goals and results.

2.1 Surface roughness

At a microscopical level every surface is not completely smooth, but it has random or uniform irregularities, with peeks and valleys. This pattern is called *roughness*, and it depends on the manufacturing process of the part. The roughness can

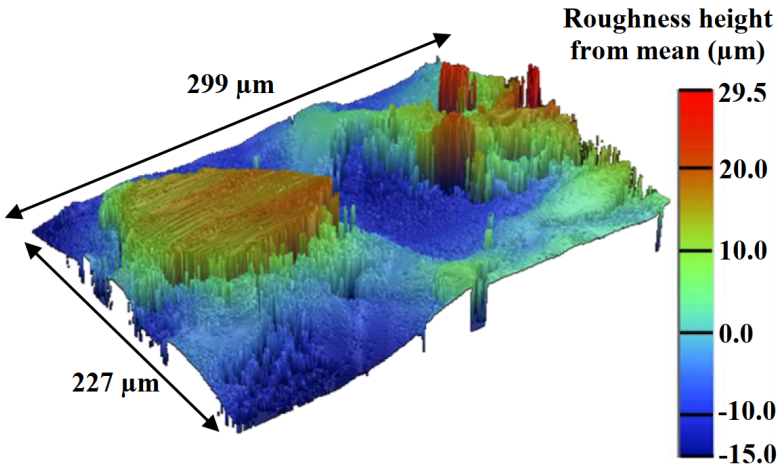

Figure 2.1: Three-dimensional profilometry of an AM surface [19]

be measured in different ways, commonly with a 2D profilometer or, for a more advanced analysis, with 3D scanners (fig. 2.1).
The profile can be defined using statistical properties; the most common ones are

Parameter	Description	Expression
R_a	Arithmetic mean deviation	$\frac{1}{l}\int \lvert y\rvert dx$
R_q	Root-mean-square roughness	$\sqrt{\frac{1}{l}\int \lvert y\rvert dx}$
R_v	Max valley depth	$\lvert\min y(x)\rvert$
R_p	Max peak height	$\max y(x)$
R_z	Max peak to valley height	$R_v + R_p$
s_k	Skewness	$\frac{1}{(R_q)^3}\frac{1}{l}\int \lvert y\rvert^3 dx$
k_u	Kurtosis	$\frac{1}{(R_q)^4}\frac{1}{l}\int \lvert y\rvert^4 dx$

Table 2.1: Roughness parameters

indicated on table 2.1. The R parameters indicate the amplitude of the roughness, and can be used to create a map to show rough spots on the surface. The amplitude is already normalized with the mean height of the sampling surface l. $R_a$is not usually able to distinguish one surface from another, as different profiles can have the same R_a. For this reason it is more useful to evaluate the standard deviation R_q and/or the peak to valley height R_z. The skewness s_k describes the profile

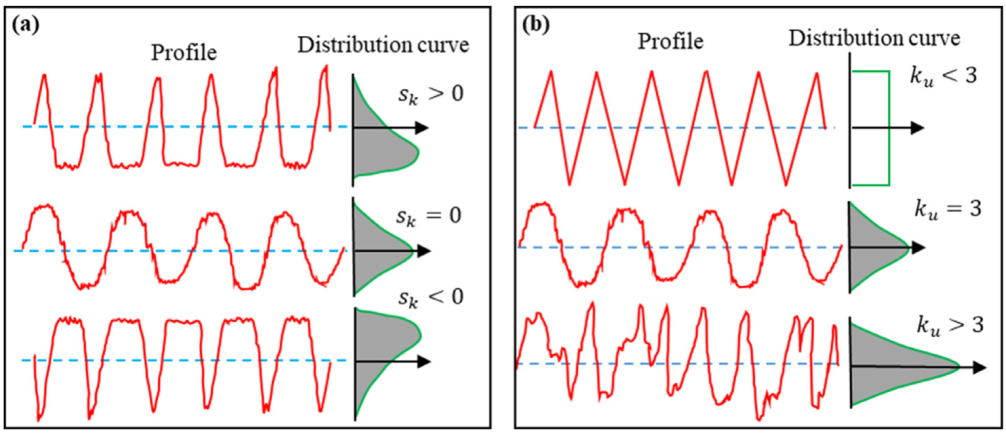

Figure 2.2: Visualization of skewness and Kurtosis parameters [22]

symmetry when compared to a Gaussian distribution. If the skewness is positive,

the valleys are larger than the peeks and vice versa. The kurtosis is a measure of the distribution of the height in the profile, so it expresses how sharp is the geometry. It is always positive and $k_u < 3$ means that the profile has generally a low number of high peeks and valleys, while if $k_u > 3$ has a high number of them.

2.1.1 Equivalency model

The necessity of an equivalence model for roughness profiles has come up when the first hydraulic tests on rough pipes were made. Nikuradse [6] started testing the surfaces scaling sand particles (lacquered to the pipe wall) with one of the previously introduced parameters (tab. 2.1) to mimic the real component. In

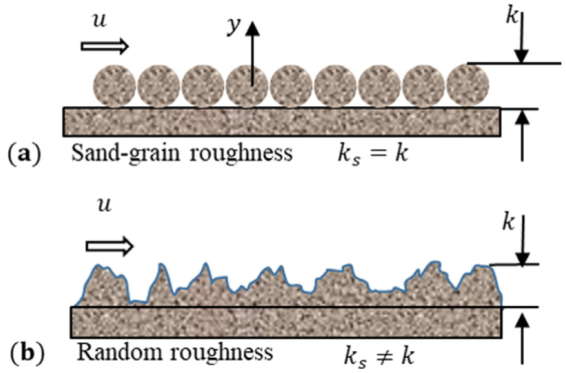

Figure 2.3: Sand grain roughness compared to a real profile [22]

figure 2.3 there is an example of sand-grain equivalent surface. In this case the parameter R_z has been used to determine the grains size $k_s = R_z$. Due to the different peak and valley distribution, the other parameters are not conserved on the sand-grain surface, because of the different shape of the grains. Colebrook and White [8] defined the *equivalent sand-grain roughness* k_s via experimental testing: two surfaces have the same k_s if their fully developed flow regime has the same characteristics.

2.2 Additive Manufacturing

Additive Manufacturing (AM) is a technique that consist in depositing and fusing material to achieve the final component shape, instead of shaving material off a bigger block like the conventional CNC milling and turning manufacturing methods. There are different AM processes, the most common for mechanical components are:

- *Fused Deposition Modeling (FDM)*: commonly found on consumer 3D printers, uses an extruder to melt a polymeric filament following the desired geometry in a 2D layer. The final component is created by stacking more layers one on top of the previous. The overall component strength is lower than the other techniques, but there are filaments with carbon or metallic particles to overcome partially this problem.

- *Stereo-lithography (SLA)*: the components are extracted layer by layer from a vat of a liquid photo-reacting polymer. A UV laser is able to activate photo-chemical reactions that solidify the polymer in specific points. This allows high geometrical precision, but the resins have a low mechanical strength and usually the dimensions of the components are limited.

- *Powder bed fusion (PBF)*: commonly used in industrial application due to its better mechanical properties and material choice, but higher cost, uses a laser to melt (Selective Laser Melting) or sinter (Selective Laser Sintering) a layer of powder. Another layer of powder is spread on top and the process repeats, as seen with FDM.

The test objects and the test rig are all manufactured using SLS technique, using different materials and printers. Siemens Energy Additive Manufacturing workshop has a set of EOS SLS printers to fast prototype and repair important engine components such as burners.

Figure 2.4: EOSINT M 280 metal 3D printer, used by Siemens Energy AM workshop

2.2.1 Powder bed fusion

PBF is a type of AM 3D-printing technique that allows to manufacture of parts directly from its computer design. It consists of melting a metallic powder layer by layer, using a laser that precisely melts the powder (SLM method). When the laser has finished its welding, another layer of powder gets deposited on top and the laser starts melting again. This method allows the realization of complex geometries like lattice structures, which can reduce the overall weight of the part while keeping its structural requirements. For this reason, there is a strong demand in aerospace companies and in industries where complex geometries are beneficial for improving greatly the final products.

PBF presents some limitations on the surface roughness and the material's

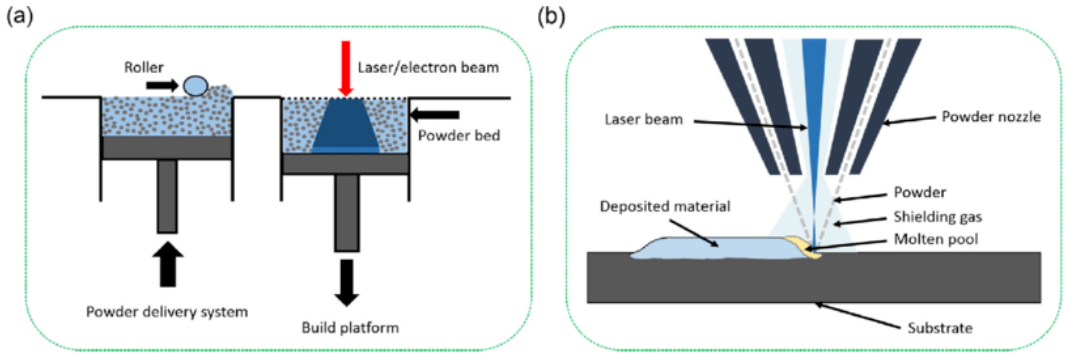

Figure 2.5: Powder bed fusion. (a) side view; (b) magnified view on the single solder point[23]

resistance to fatigue when compared to machined parts. The parameters affecting the print surface quality are related to the heat accumulation in the part [24] that can make unwanted powder particles adhere to the part surface. In particular:

- Part location on the build plate: if two parts are too close to each other, they can conduct heat to the powder between them and melt it. This can cause clogging of small cooling channels for example;
- Angle between the feature and the build plate: it can change the roughness of parts due to different layer overlap;
- Upskin/downskin direction of the print: the downskin print has worse surface roughness because the heat is transferred to the previous layer, which is thinner than the top one and therefore it receives too much heat. The overheated bottom layer causes unwanted powder particles to adhere to the component surface;

- Wiper's capability to distribute uniformly the next powder layer. If there are heterogeneous zones the roughness may vary in those places;
- Argon stream direction. All the process is done in an inert atmosphere to avoid oxidation. The argon is flowing from one side of the build plate to the other, dragging spatter and oxide formations. This makes the outflow side of the plate rougher than the other side.

This technique is not limited to metallic components, but it can be used also with polymers. An example is the creation of the plastic components for this rig: they are made with SLS using EOS PA2200 Polyamide 12 powder. It is more expensive than the traditional Fused Deposition Modeling (FDM) used commonly on consumer 3D printers, but the upside is the higher component resistance to structural stress. In the test rig the printed inlet was able to resist to 20 bars of water pressure, with a large safety margin.

2.3 Fluid dynamics

In this section the flow behavior inside a channel will be briefly explained, focusing on the boundary layer and how it is affected by the surface roughness.

2.3.1 Velocity Boundary Layer

Close to the wall, the flow encounters a strong velocity gradient due to friction. Moving away from it, this gradient decreases until it becomes negligible. This last condition is commonly referred as *external flow*. In the near-wall zone, these strong gradients generate shear stress between fluid layers; the zone where these stresses have a significant impact on the flow is called *Boundary layer* [25].
The following explanation will use a flat plate as an example, but these conditions can be found also on a channel's walls. The difference between an open flow and a closed flow (channel) will be explained at the end of the section.
The momentum boundary layer phenomenon is driven by the fluid's viscosity. On the solid surface, the flow velocity has to be zero (*no-slip condition*, $u_{wall} = 0$). The velocity rises when the distance from the surface increases, until it reaches the external conditions u_e. The boundary layer composition depends mainly on the free stream velocity because of the variation of the velocity gradients. When the speed is low, the boundary layer is called *laminar*, and the streamlines are parallel to the wall. At increasing tangential speed, the velocity gradient becomes stronger and it causes reverse flow close to the wall. This induces vortices in the boundary layer, which now is called *turbulent*. On figure 2.6 it is possible to see the boundary layer evolution, from the free stream to the fully turbulent velocity distribution

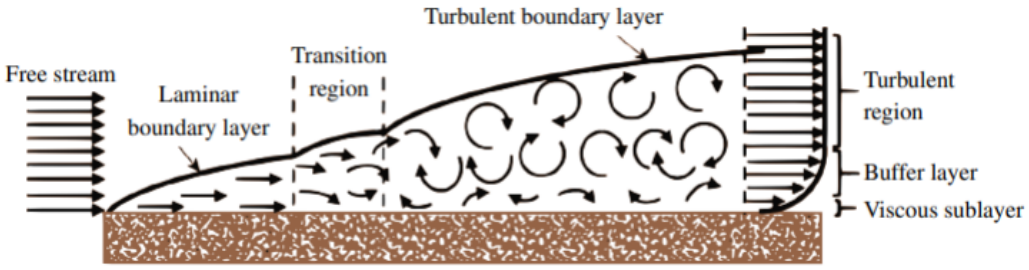

Figure 2.6: Momentum boundary layer

on the right. The indicated thickness of the boundary layer δ is defined at the y position where $u = 0.99u_\infty$.
The boundary layer is important when dealing with rough surfaces, because its effect do not propagate into the external flow. An important parameter is the *friction velocity* u_τ, which is defined as the ratio between the wall friction and the flow density:

$$u_\tau = \sqrt{\frac{\tau_w}{\rho}} \tag{2.1}$$

The shear stress for a Newtonian fluid is:

$$\tau = \mu \frac{\partial u}{\partial y} \Rightarrow \tau_w = \mu \left.\frac{\partial u}{\partial y}\right|_{y=0} \tag{2.2}$$

This value is obtained through experimental correlations. The shear velocity is used for non-dimensional analysis of the boundary layer: flow speed u and distance from the wall y then become u^+ and y^+.
The boundary layer can then be divided in two main regions, *inner* and *outer* when $y^+ > 30$. The inner region can be sub divided into two zones: *viscous sublayer* ($y^+ < 5$) and a *buffer layer*. The outer region is also called *logarithmic layer*, because there is a log relationship between u^+ and y^+.

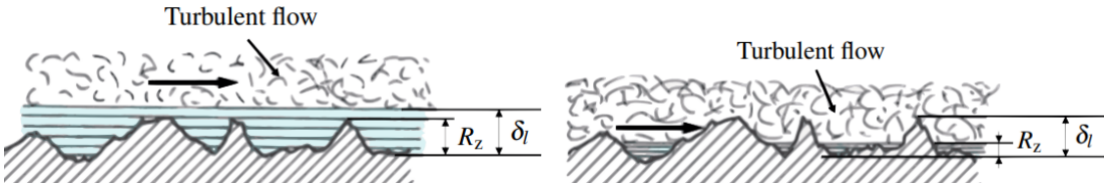

Figure 2.7: Hydraulically smooth (left) and rough (right) surfaces

From a flow mechanics perspective, a surface is usually defined as rough if its peek to valley roughness is higher than the thickness of the viscous sublayer (fig. 2.7).

An important number for defining the flow regime is the *Reynolds number*, which is defined in details in the next section. For a smooth circular channel, the transition from laminar to turbulent flow is commonly found at $Re \approx 2300$.

2.3.2 Reynolds number

The flow characteristics can be expressed with a non-dimensional number called *Reynolds number*, that for a channel is defined as:

$$Re = \frac{\rho u_\infty d_h}{\mu} \tag{2.3}$$

From the equation 2.3, the Reynolds number is the ratio between intertial and viscous forces of the fluid. Thanks to this number is possible to compare flows inside different sized channels and fluid characteristics, thus conserving dynamic similarity. This is not a precise reference, as seen in the previous section the transition is a

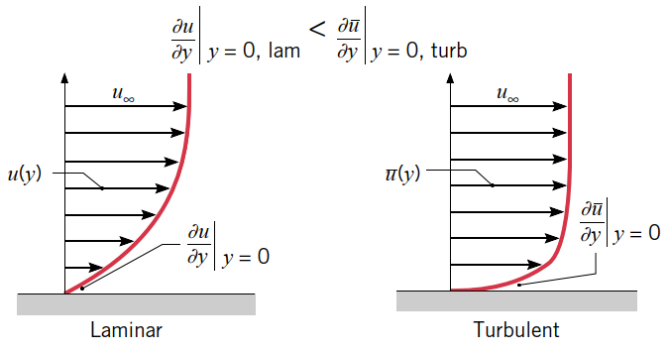

Figure 2.8: Laminar and Turbulent boundary layer profile [26]

gradual process between the two boundary layer profiles seen on figure 2.8.

2.3.3 Darcy friction factor and Moody diagram

The viscous stresses on the channel's wall cause distributed pressure losses. Darcy [4] created a friction factor to evaluate them:

$$\Delta P = \frac{1}{2}\rho u^2 f_d \frac{L}{d_h} \tag{2.4}$$

In equation 2.4 the coefficient f_d is called *Darcy friction factor*. The pressure drop depends linearly with the channel's length and is inversely proportional to the hydraulic diameter.

A laminar flow follows Poiseuille's law, so the friction factor does not depend on the relative roughness:

$$f_{d,laminar} = \frac{64}{Re} \tag{2.5}$$

For turbulent flows there are many correlations available. The most common is the implicit *Colebrook-White* correlation [8]:

$$\frac{1}{\sqrt{f_d}} = -2\log\left(\frac{\epsilon}{3.7d_h} + \frac{2.51}{Re\sqrt{f_d}}\right) \tag{2.6}$$

The results for straight channels are usually read on log-log diagrams, with Re on the x and f_d on the y. Moody [10] found that rough channels have a constant

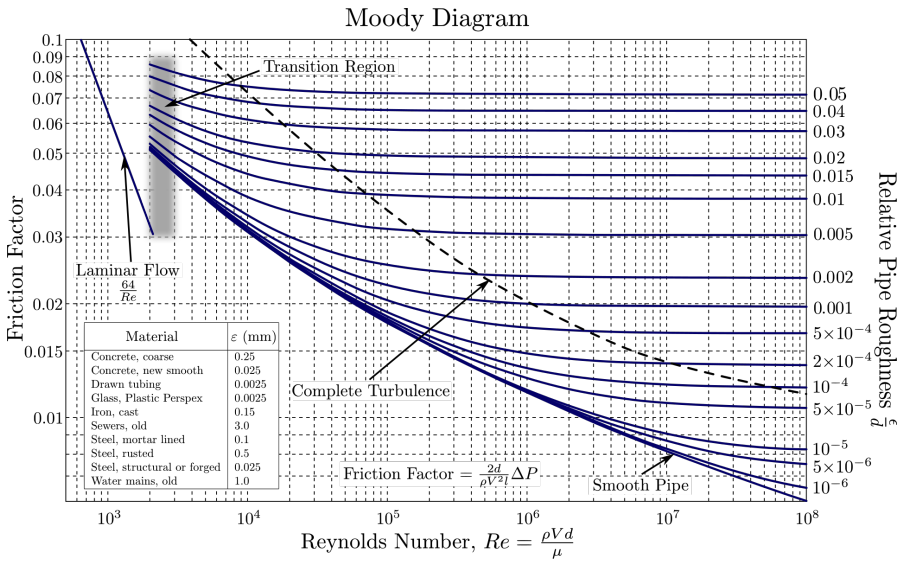

Figure 2.9: Moody diagram [27]

friction factor at high Re. For this reason, a second y axis was added to indicate the relative roughness effect on the friction factor.

2.3.4 Notch effect

When entering and exiting the test object, the water flow meets a 90° sharp edge. This geometric feature is an abrupt variation in the hydraulic diameter that creates shock losses and flow recirculation, as seen in figure 2.10 for the outlet. Idel'chik [28] states that there are localized dynamic pressure drops where the flow encounters sharp edges:

$$q_{loss,in} = c_1\frac{1}{2}\rho_{in}u^2 \qquad q_{loss,out} = c_2\frac{1}{2}\rho_{out}u^2 \tag{2.7}$$

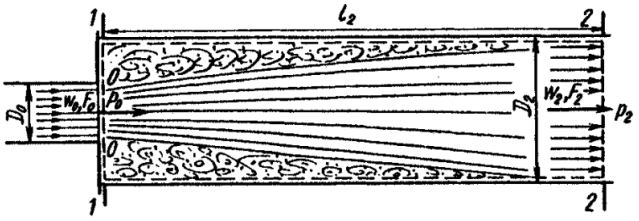

Figure 2.10: Outlet notch effect [28]

The coefficients $c_1,\ c_2$ depend on the flow regime and the area ratios. For the qSSHT test, the coefficients found are represented in table 2.2.

Coefficient	*Laminar*	*Turbulent*
c_1	0.5	0.5
c_2	2	1

Table 2.2: Notch effect correction coefficients [28]

2.4 Heat transfer

In this section the focus will be heat exchange mechanics, specifically forced convective heat transfer and the effects that roughness may have on it.

2.4.1 Conduction

Conduction is a heat transfer mechanism that happens at atomic scale: the atoms bump into each other, and atoms with higher random translational motion (higher temperature) transfer their energy to atoms at lower temperature [26]. On a macroscopic scale, it is seen as a diffusion of energy from the hottest part to the coldest. This phenomenon happens in all physical states, but it is the prevalent heat transfer mechanism between solids.
It is possible to quantify the heat transfer via conduction using *Fourier's Law*, which for one-dimensional heat transfer is:

$$\dot{q} = -\kappa \frac{dT}{dx} \tag{2.8}$$

κ is the material's conductivity, and depends on the bonding of the material's atoms freedom of movement. For this reason, metals usually have high thermal conductivity and plastics/ceramics a low one.

For the test channels in this experiment, the most significant conductive heat transfer happens internally in the TO, in radial direction.

2.4.2 Convection

For fluids there is another heat transfer mechanic, called convection. This combines conduction with fluid dynamics, and is evaluated at the contact surface between a fluid and a solid [26]. The motion of the fluid contributes to heat transfer, bringing away hot particles from the contact surface and mixing them with the cold ones. This phenomenon can be called *natural* or *forced*. It is natural if the motion of the fluid is done by gravity, where the hotter particles move up because their density is lower. Forced convection happens when the flow is moving by an external force applied to it, e.g. a pressure differential created by a pump before the channel. The convective heat transfer can be modeled with *Newton's Law of cooling*:

$$\dot{q} = htc(T_s - T_\infty) \tag{2.9}$$

Where T_s is the surface temperature, T_∞ is the outer flow temperature, and htc is called *heat transfer coefficient*, that depends on the flow conditions and on the material and fluid characteristics.

2.4.3 Thermal Boundary Layer

In a similar way than the velocity boundary layer, a *thermal boundary layer* (figure 2.11) develops on the contact surface between the solid and the fluid. On the

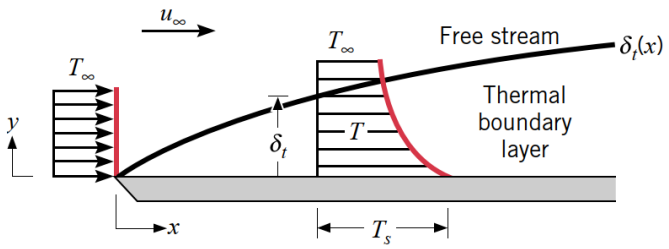

Figure 2.11: Thermal Boundary Layer development [26]

surface the temperature has to be the same as the wall T_s, while in the outer stream it reaches the bulk fluid temperature T_∞. The thickness δ_T is the y where:

$$\frac{T_s - T}{T_s - T_\infty} = 0.99$$

It is possible to obtain the local heat transfer coefficient combining Fourier's law (eq. 2.8) in the fluid at wall surface with Newton's law of cooling (eq. 2.9):

$$htc = \frac{-k_f \left.\frac{\partial T}{\partial y}\right|_{y=0}}{T_s - T_\infty} \tag{2.10}$$

$(T_s - T_\infty)$ is constant, and δ_T increases with x. This means that $\left.\frac{\partial T}{\partial y}\right|_{y=0}$ decreases with x, therefore the htc also decreases along the channel.

2.4.4 Nusselt number

Convective heat transfer can then be studied using a non-dimensional parameter, in a similar way than what was reported before for the Darcy friction factor. The *Nusselt number* is defined as:

$$Nu = \frac{htc\ d_h}{k_f} = + \left.\frac{\partial T^*}{\partial y^*}\right|_{y^*=0} \tag{2.11}$$

The "*" parameters are dimensionless temperatures and distance from the wall: $T^* = (T - T_s)/(T_\infty - T_s)$, $y^* = y/d_h$.
For a turbulent boundary layer in smooth channels there are many correlations based on experimental data. The most famous one is *Dittus-Boelter equation* for smooth channels under fully-developed turbulent flow:

$$Nu = 0.023 Re^{4/5} Pr^{0.4} \tag{2.12}$$

This correlation is valid for:

$$\begin{cases} 0.7 \leq Pr \leq 160 \\ Re_d \geq 10000 \\ \frac{L}{d_h} \geq 10 \end{cases}$$

This correlation, when confronted with experimental data, has an uncertainty as big as 25%. More modern and complex correlation try to expand the range of validity and lower the error. Gnielinski [29] introduced one of these correlations:

$$Nu = \frac{\left(\frac{f}{8}\right)(Re - 1000)Pr}{1 + 12.7\left(\frac{f}{8}\right)^{0.5}(Pr^{2/3} - 1)} \tag{2.13}$$

Gnielinski's correlation extends the validity to:

$$\begin{cases} 0.5 \leq Pr \leq 2000 \\ 3000 \leq Re \leq 5 \cdot 10^6 \\ \frac{L}{d_h} \geq 10 \end{cases}$$

This correlation depends on the turbulent boundary layer development, so the initial Re of validity is not a fixed value. In this thesis project, Gnielinski's correlation will be used as a reference smooth channel.

2.4.5 Thermal notch effect

A. F. Mills [30] investigated the behavior of turbulent heat transfer at the entrance of a circular channel. In particular, he studied the *Uniform heat flux*.
His experimental setup was composed of a brass pipe 90 diameters long, that is heated up by an electrical resistor placed around it. Air is flowing inside the pipe and gets heated by the wall. Then, a thermocouple is moved along the pipe to gather the temperature distribution. Various inlet geometries were explored either experimentally or theoretically. In particular, a theoretical analysis was given for a sharp 90 degrees inlet, which matches the inlet condition found in the Joule Heating rig.
Mills found out that there is a formation of air pockets right after the sharp edge, implying the existence of a *vena contracta* in the channel's center. In figure 2.12

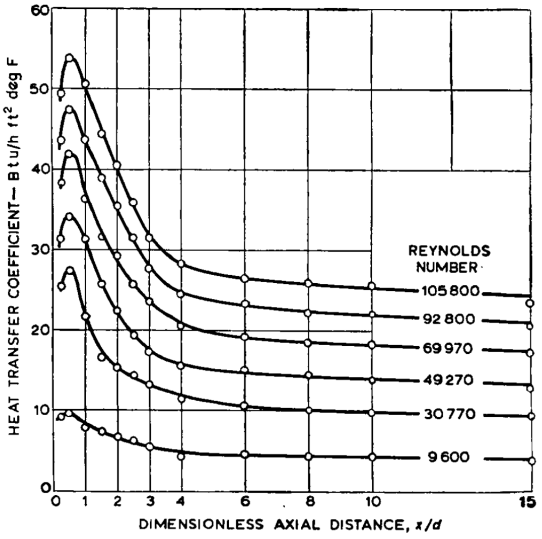

Figure 2.12: Local heat transfer coefficients for 90 degrees edge entrance [30]

is possible to see that the edge affects heat exchange at any velocity, even when the flow is in low turbulent regime. This increase in the heat transfer coefficient has to be taken into consideration when testing short channels. The effect can be plotted by normalizing the Nusselt number: Nu_{av}/Nu_{∞}, where Nu_{av} is the integral mean of the Nusselt number, measured over the entire length of the pipe and Nu_{∞} is the Nusselt number under full developed conditions, far away from

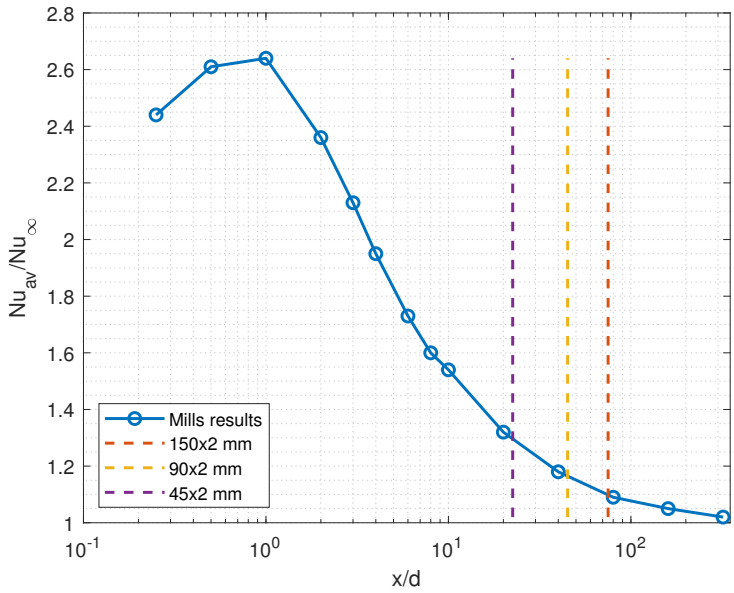

Figure 2.13: Comparison of Mills [30] entrance effect with some TO examples

the entrance. Comparison of the experimental results with some example specimen lengths for the Joule heating rig shows how much the entrance effect changes the heat exchange performance of the channel (figure 2.13).
The most critical test object is the shortest one: 45 mm long with a hydraulic diameter of 2 mm taken as a worst-case scenario. The average Nusselt for this TO is about 30% higher than the fully developed flow. Because of this difference, it is difficult to evaluate the roughness effect of the TO and find an improvement in heat exchange due to the entry effect.
An important note on this research is that all of these results were obtained using air as medium. The qSSHT rig uses water, which has a completely different Pr that also is not constant with temperature. This effect may change a lot with the Pr.

2.5 Joule heating

Heat in the metallic TO is generated by converting electrical energy into thermal one, exploiting *Joule effect*. The power generated is:

$$P_{el} = V \cdot I \tag{2.14}$$

There is a relation between voltage and current, using *Ohm's Law*:

$$V = RI \tag{2.15}$$

The resistance R is proportional to the length of the channel and inversely proportional to the cross-section area. R also depends on the material, for example Aluminum has a resistivity ρ that is one thousandth than the ones of Stainless Steel and Inconel 939.
The circuit in the test rig is voltage regulated, so the total power is expressed as:

$$P_{el} = \frac{V^2}{R} \tag{2.16}$$

This power is generated internally in the TO's volume and will be evaluated in 3D by *Star-CCM+* solver. There is also another generation localized at the contact surfaces between the TO and the copper clamps, where a localized voltage drop due to the material discontinuity is created.
The power supply of the test rig uses alternate current $P(t) = V(t)I(t)$. The important power generated is the average one, evaluated using Root Mean Square (RMS) values $P_{avg} = V_{rms}^2/R$.

Chapter 3

Experimental setup and methodology

This chapter describes the physical setup used to gather the experimental data, and how to operate the test rig. The setup is divided in flow path, electrical path and sensors descriptions. A brief description on the test objects is presented, more info about the TOs can be found in Appendix A.
The test procedure is then described only physically, leaving the numerical solver in the appendix 4.
Finally, an analysis of the results' uncertainty is conducted, to understand if the data can be trusted.

3.1 Test rig

The Joule Heating rig consists of heating up the test object by using an electrical current flowing into it. Water flowing into the test object channel is heated up by the solid wall and the temperature difference between the inlet and the outlet is measured.
On figure 3.1 is represented the test section of the Joule heating rig. The test object is covered in a thick neoprene insulator for achieving adiabatic wall conditions.

3.1.1 Water loop

The fluid used in the test rig has to be non-conductive due to the current flowing inside the test object. Therefore the choice has fallen on de-ionized water. The water flows inside a closed loop as depicted in figure 3.2.

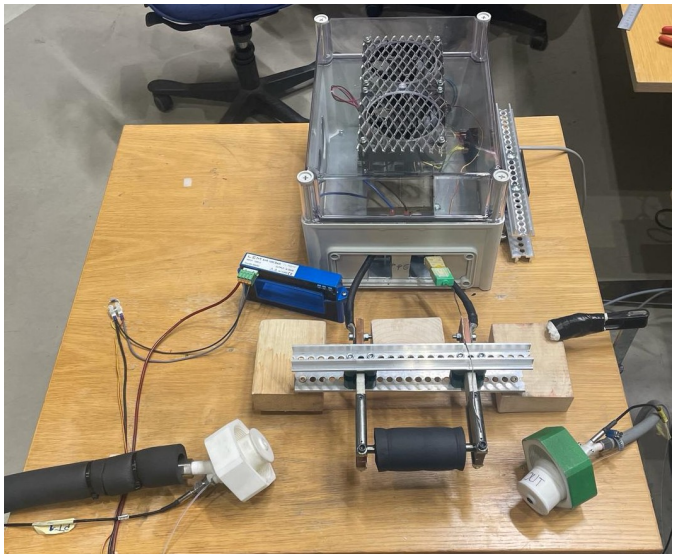

Figure 3.1: Joule heating rig open for test object replacement

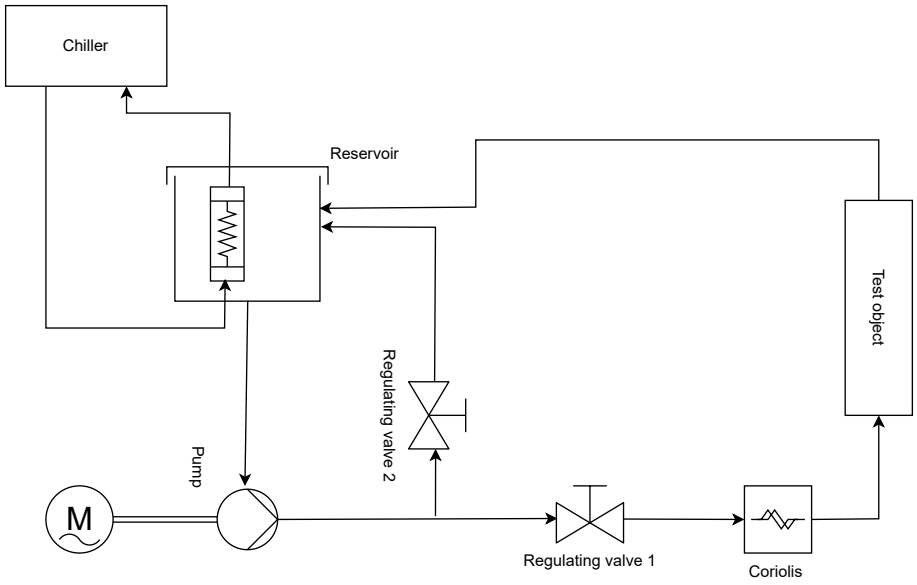

Figure 3.2: Hydraulic scheme of the Joule Heating rig

- *Water reservoir*: used to keep the inlet temperature fixed with the help of the chiller and to dampen vibrations. In case of leaks during testing, it also provides extra time for shutting off the heater without damaging the rig.
- *Chiller*: Uses a mixture 1:1 of water-glycol to set the water temperature at a certain target. The mixture flows inside a copper winding inside the water tank

to exchange heat. Typical testing is done by setting the water temperature at 10, 20, and 30 °C.

- *Pump*: Volumetric pump rated for a maximum pressure of 20 bar, moved by a three-phase electric motor.
- *Regulating valves*: manual conic valves used to regulate the mass flow coming into the test object. #1 is used along the flow, so opening it equals a higher mass flow, while #2 is a bypass valve, so it has to be operated oppositely.
- *Coriolis*: mass flow meter that uses Coriolis acceleration to get a precise mass flow measure.
- *Connections*: all the connections between the components are made by flexible hoses, rated for a maximum of 20 bars of pressure.

3.1.2 Electrical connection

To keep the circuit as simple as possible, the test object is heated up by a 50 Hz AC, the same as the power plug frequency. The voltage is regulated via two transformers: one variable autotransformer and one with a fixed ratio between windings of 230:2.

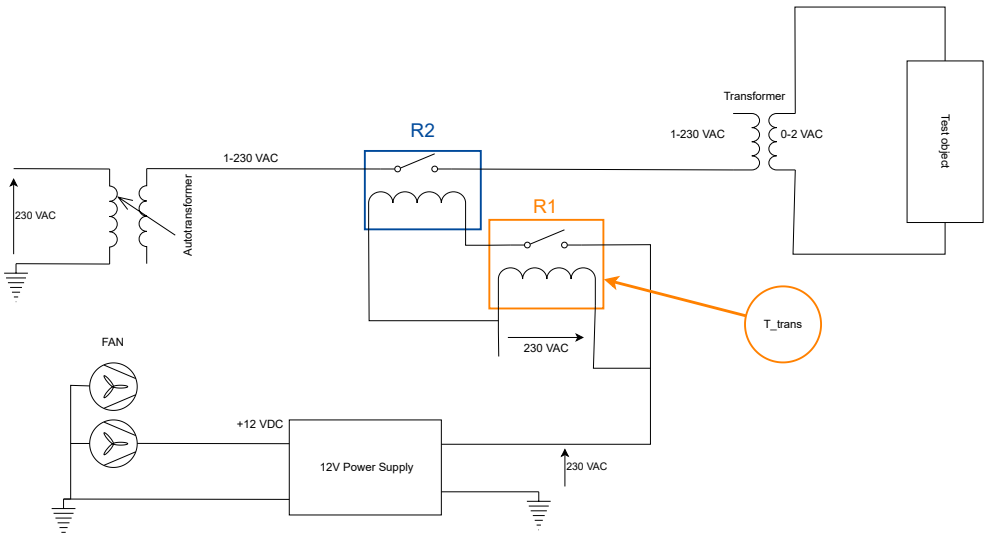

Figure 3.3: Electrical scheme of the Joule Heating rig

- *Autotransformer*: the number of windings on the secondary coil of the transformer can be selected to regulate the output voltage from 0 to the same input

voltage. The autotransformer used can hold up to 8A of current, therefore a circuit breaker is installed before it.

- *Fixed transformer*: It is a custom-made transformer based on a model found in a common microwave. The first model used 230 windings on the primary coil and a copper bar on the secondary coil, providing an output of 1V max. A newer version has been developed using a $35mm^2$ cable that does two windings on the secondary coil, permitting a max output of 2V.
- *Copper bars/cables*: Two copper bars with a cross-section of 10 x 30 mm are used to keep the test object in position and transmit the electrical current, without heating up from the current passing through them.
- *Induction Ammeter*: Measures the current flowing into the test object using a current transformer connected to the acquisition board. The current transformer is a ferromagnetic core with a winding around it, all together installed around the cable to measure. The magnetic field induces a current into the windings and these are connected to an acquisition board.
- *Safety relays*: R1 is a thermal relay that opens the circuit when the thermocouple installed on the copper bar surpasses $50°C$. This relay switches the relay R2, which is a normal circuit breaker rated for 16A.
- *Power supply*: AC-DC transformer that converts the line 230VAC to 12VDC for powering up the cooling fans.
- *Cooling fans*: 2 x 120mm fans used to cool down the transformer and the power cables to deliver safely the maximum electrical power.

An improvement made in this project is the ability to change the transformer ratio. Previously, the copper bars were part of the secondary winding of the transformer, giving a ratio of 230:1. By clamping some connections to a thick electrical cable, rated for 240 A, it was possible to bend two windings around and obtain the ratio of 230:2. This allows for the testing of low-conductive materials, like Stainless Steel and IN939. The electrical power is greatly increased by this modification, this is because it depends by the voltage squared:

$$P_{el} = V \cdot I = \frac{V^2}{R} \Longrightarrow V \rightarrow 2V \Rightarrow P \rightarrow 4P \tag{3.1}$$

This cable winding is rated only for 240 A, however it can be pushed at 300-340 A thanks to active cooling of the cables. Nonetheless, a test object made out of aluminum has a resistivity that is 10 times lower than the others, this would mean that there can be currents up to 3000 A flowing into the secondary circuit. In these cases, the original copper bar is installed again to allow full range testing.

3.1.3 Measurement instrumentation

All the instruments used for gathering data during the experiments are connected to the test rig following this scheme:

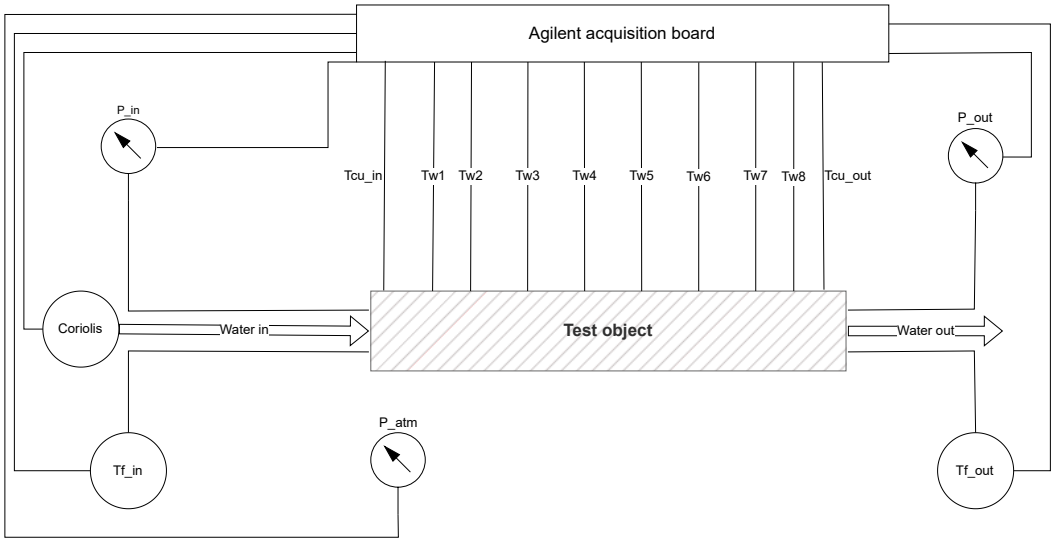

Figure 3.4: Instrumentation scheme

In the following table there is a brief description of the measuring devices used in the rig:

Parameter	**Device**	**Range**	**Uncertainty**	**Unit**
Mass flow	Siemens MASS2100	0-75 g/s	0.53 %	g/s
In/Out P water	Rosemount 3051	0-2000 kPa	$10^{-4}P + 0.048$	kPa
P ambient	Rosemount 3051	80-200 kPa	$10^{-4}P + 0.75$	kPa
In/Out T water	Pentronic PT-100	0-200 °C	0.08	°C
In/Out T copper	Type-K TC	0-500 °C	0.2	°C
T wall	RS PT-100	0-500 °C	0.15	°C

Table 3.1: Measurement devices

Each device gets calibrated once a year, to ensure the reliability of the measure and the correct functioning. Next, each device type will be briefly described.

Temperature probes

Figure 3.5: Pentronic PT-100, used for water inlet/outlet temperature

The most common way used to measure the temperature is done by exploiting the change of resistance in a material with the temperature. By measuring this variation and comparing it with a reference, it is possible to obtain the real temperature with a good accuracy. The two types of thermal elements used are:

- *PT-100*: the resistance is made out of platinum, and the reference resistance is 100 Ω at $0°C$. IEC 60751 [31] classifies them based on the accuracy. In this project all the PT100s are Class A (example on figure 3.5);

- *Thermocouple type-K*: thermocouples are cheaper than PT100s, have faster response time to changes and can withstand a wider range of temperatures. However, thermocouples were used for the copper bars temperature due to their smaller format, shaped like a thin wire. They need to be calibrated before use, have the positive and negative terminals made out of two different materials, so their junction is the sensitive element. A type-K thermocouple has the positive made of Ni-Cr alloy and the negative of Ni-Al alloy [32].

Pressure transducers

The pressure transducers are usually diaphragms with each side connected to a different pressure source. An absolute transducer on one side is connected to ambient pressure or an internal reference, while a differential needs to be connected on both sides to the test. The diaphragm can be made either with a piezoresistive strain gauge (resistive transducer) connected to a Wheatstone bridge or a capacitive plate placed next to a fixed electrode. The Rosemount 3051 (fig. 3.6) uses the capacitive method, with an internal circuitry that converts the pressure difference in a voltage signal for the acquisition board.

Figure 3.6: Rosemount 3051 pressure transducer. It can measure absolute or differential pressure.

Coriolis mass flow meter

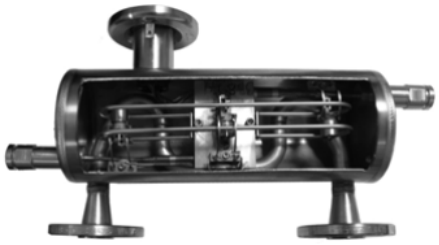

Figure 3.7: Siemens SITRANS F C 2100 Coriolis mass flow meter

A Coriolis mass flow meter measures the flow using its inertia. An actuator vibrates the internal pipe at a certain frequency. This induces a Coriolis acceleration in the flowing stream, and the latter impresses a twisting force on the tube that causes a phase shift of the response. This force is proportional to the mass, so a sensor measures the angular momentum of the tube and obtains the corresponding mass flow. In figure 3.7 is possible to see the internal structure of the MASS 2100 used for this project. The Coriolis has been mounted on rubber supports to dampen external vibration (such as the pump's) that can alter the measurement.

Acquisition system

All of the devices previously described output a voltage signal that has to be converted into a digital signal and saved on a computer. The device that makes this possible is the *Keysight Agilent 34972A* data acquisition system. The Agilent is connected to a pc via TCP-IP protocol, and the computer uses an in-house software based on NI LabView called *RigView* (figure 3.8). The Agilent acquires the data at 2 Hz sample rate, while the data is saved on a text file at 1 Hz rate. RigView also

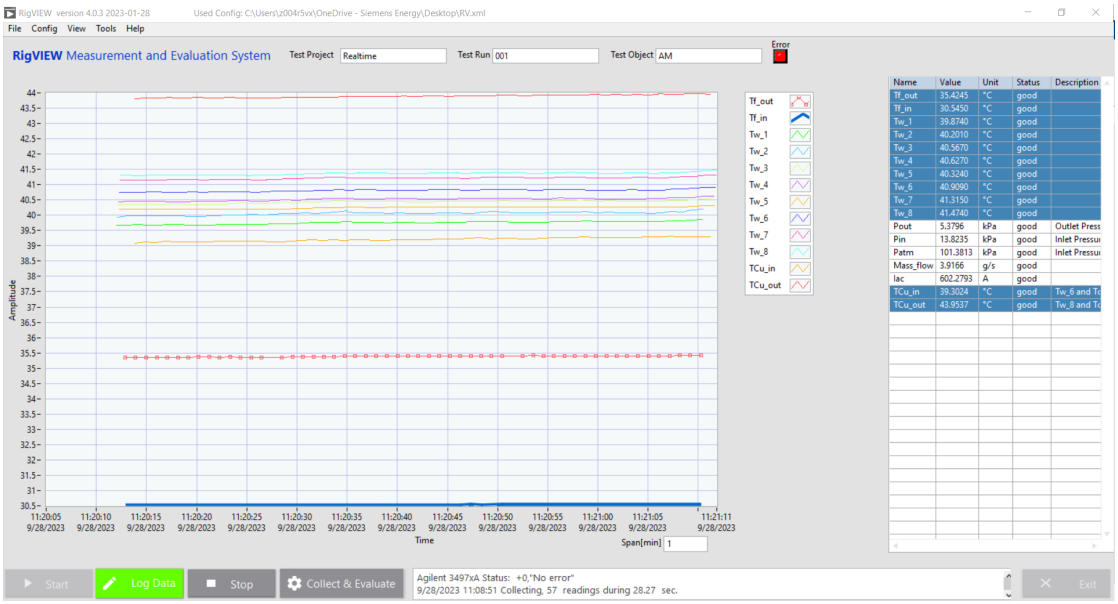

Figure 3.8: RigView interface during a test

converts the voltage measurements from the devices into a dimensional value (e.g. for a pressure measure $mV \rightarrow kPa$), using a linear relation: $Value = G * mV + O$. The gain G and offset O are given by the calibration department.

3.2 Test objects

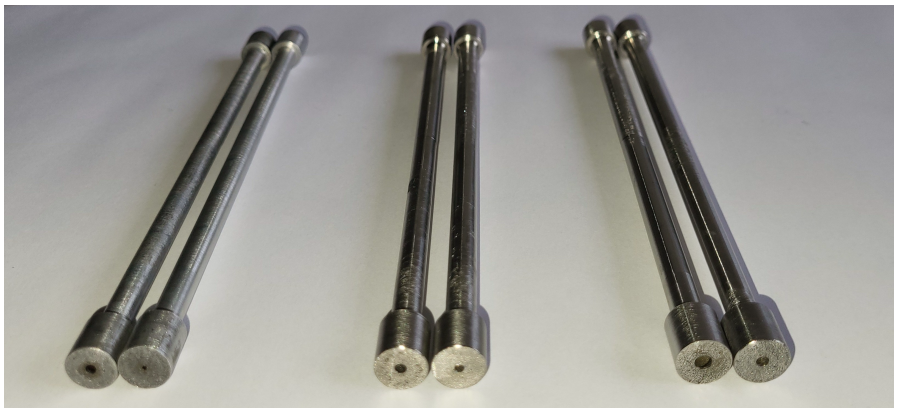

Figure 3.9: Machined test objects: *Aluminum*, *Inconel 939* and *Stainless Steel*

The standard test objects are cylinders with a channel inside where the water is flowing. They are printed with different specifications, like the channel cross-section

shape and dimensions and the overall length of the TOs. Some test objects have been machined on the outer side to obtain a higher electrical resistance (smaller cross-section). This increase allows the generation of a bigger heat power due to the Joule effect, where the dissipated power is $P_{el} = I^2R$ and R is inversely proportional to the cross-section.
The outer dimensions of the test objects are: 90mm/150mm long, 10mm outer diameter and 6mm outer diameter if machined, leaving the 10mm diameter at the edges for the copper clamps. The internal hydraulic diameter and area are obtained with an imaging procedure explained in Appendix B.
The complete list of test objects and their specifications can be found in Appendix A.

3.2.1 Materials

The materials used for manufacturing the TOs are these:

Name	**Technical name**	**Powder size** $[\mu m]$	$\boldsymbol{k}$ $[\frac{W}{mK}]$	σ $[\frac{S}{m}]$
Aluminum	AlSi10Mg	25-70	100	$2.87 \cdot 10^7$
Stainless Steel	316L	20-65	14	$1 \cdot 10^6$
Inconel 939	IN939	35-75	12	$8.15 \cdot 10^5$

Table 3.2: Test object materials

Note that the electrical conductivity is an estimate and it is not needed for the numerical solver, but it is still assigned in the code. The solver focuses on total power generated $P_{el} = VI$ and the voltage is iterated to match the experimental P_{el} needed to achieve power balance.

3.3 Flow path and sensor positioning

The inlet and outlet sections of the rig have to be designed to avoid turbulence before the TO's entrance. At the same time, the pressure taps and the temperature probes must be positioned as close as possible to the inlet/outlet, in zones with a cross-section area way bigger than the TO's so the velocity of the flow is not affecting the sensors' measurements. In figure 3.10 a cross-section of the previous inlet design is presented. This geometry had problems with the pressure measurements: during the print, the bottom channel was clogged by trapped powder. Another issue was leakage of the inlet pressure tap when reaching more than ~ 8 bars. This happened because the pressure tap was only kept in place by superglue, so a

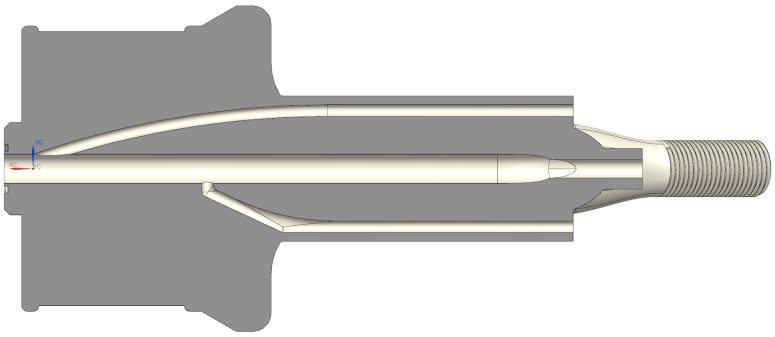

Figure 3.10: Previous inlet/outlet design

threaded insert was needed for getting accurate measurements at higher pressures. The last improvement has been increasing wall thickness to prepare the rig to sustain more than 20 bars of pressure (reaching higher Re). The improved design

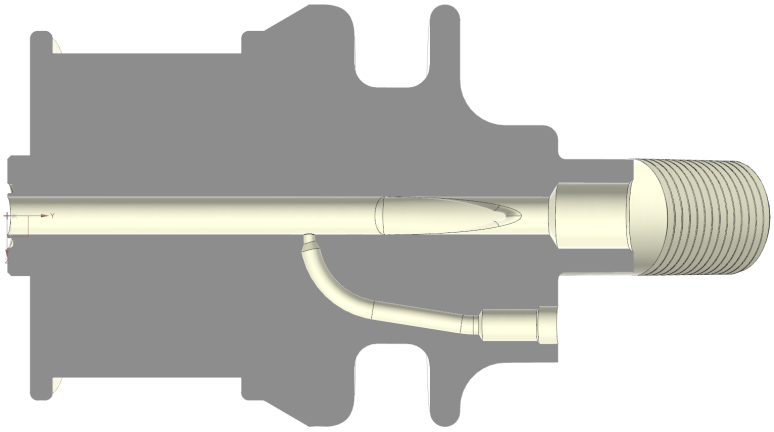

Figure 3.11: Current inlet/outlet design

(fig. 3.11) has threaded inserts for both the PT100 holder and the pressure tap. This one has a shorter channel to avoid print problems, and has a thicker wall to resist higher pressure. This new inlet/outlet setup has been validated comparing the friction factor and Nusselt results of a smooth channel with Colebrook-White and Gnielinski's correlations respectively (defined in chapter 5). In figure 3.12 is possible to see the flow path of the test section. On the left, the purple probe is the PT100 temperature sensor, kept in place by the threaded insert. On the right it was removed to show the pressure tap hole. Between the test object and the inlet/outlet components a thick o-ring seals the connection, and axial pressure is applied by screwing the green nut on the central part. The test object is also held in place by the copper bars, with two screws to apply the correct pressure. In the

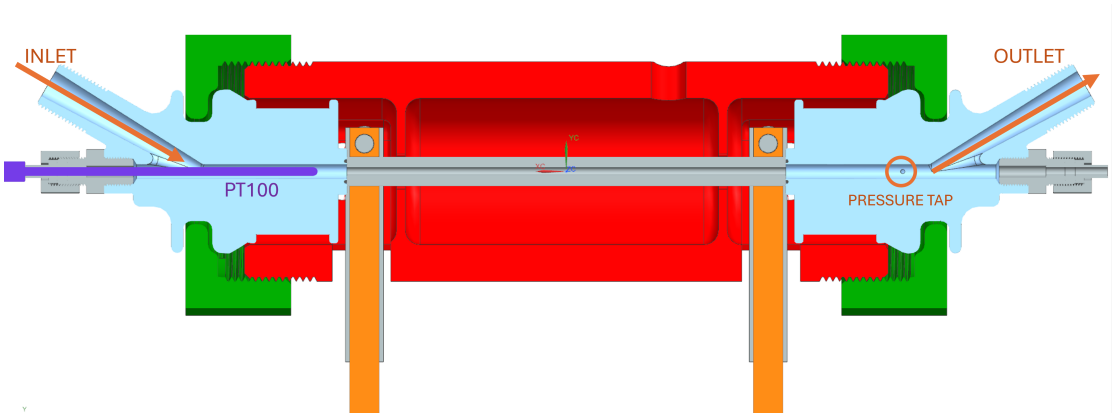

Figure 3.12: Section view of the rig

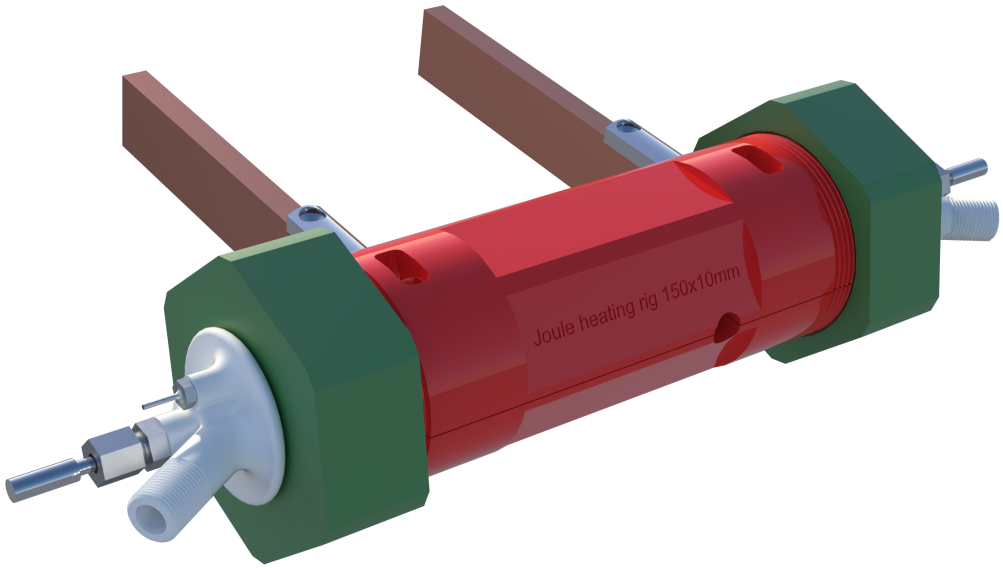

Figure 3.13: Rendering of the assembled test section with the new inlet/outlet design

3D render (figure 3.13) the pressure tap insert and the PT100 holder are clearly visible. This setup did not present any kind of leakage, even at pressures reaching 20 bars.

One last note is on the copper clamps: they are reinforced with stainless steel inserts close to the TO clamps because copper is a ductile material, and it deforms with repeated TO replacements. The inserts redistribute the clamping pressure and help with the durability of the bars.

3.4 Testing procedure

The experiment involves different risks for the operator and the environment, mainly electrical shock, fire and high pressures. For this reason a detailed risk analysis was developed and reviewed before operating the rig.

The first operation is to fill up the water tank with deionized water. The water loop does not have a filter, so a weekly replacement of the water is necessary to avoid the accumulation of pollution and to make sure it does not conduct electricity, damaging the test rig. During the filling procedure the feedback valve is fully open and the direct valve is fully closed (if the test section is disassembled for a TO change).

At least one hour before testing, the chiller has to be turned on and set at a temperature slightly higher or lower than the desired inlet one for the test. As an example: for Pr ~ 5 the inlet temperature has to be $\sim 30°C$; the chiller is set to $32°C$. In this way we compensate for the thermal loses throughout the piping of the system, achieving the desired temperature at the inlet. Turning on the pump speeds up the process.

3.4.1 Test object installation

The TO is cleaned to avoid the presence of debris stuck inside the channel. It is submerged into an alcohol bath and agitated by an ultrasound cleaning machine. When clean the next step is the installation of PT100s onto the external wall. This is the most delicate operation when setting up the rig, because the PT100s are 1x2 mm large and the electrical cables are really thin. They are fixed in position with two pieces of electrical tape, chosen for its elasticity that allows good contact pressure between the PT100 and the TO.

The TO's sides are then clamped in the copper bar. The screws are tightened with the torque wrench, so the contact pressure is always the same in all tests. The o-rings are installed in the inlet and outlet slots with the help of some vaseline to keep them in place and the plastic part of the test section is assembled.

With the rig assembled, all valves are opened and the pump is turned on. The test section gets slightly pressurized ($\sim 2-3$ bars) by partially closing the bypass valve. At this point the air bubbles present in the pressure taps connections are drained, otherwise the measurement would be incorrect.

The last step is pressurizing the loop by almost fully closing the bypass valve and inspecting every part looking for water leakages, especially close to the pressure taps and temperature probes. If no leakages are detected the test can start.

3.4.2 Heater preparation

The heater relay box and its power source have to be both connected to the mains of electricity. As a safety feature, there is a thermocouple into the outlet copper bar that shuts off the system if there is a overheating. The thermal limit for the rig is $\sim 85°C$ because of the electrical tape that is keeping the PT100s in place.

3.4.3 Darcy and Nusselt test

After the rig is prepared we can proceed to test. The step-by-step procedure is the following:

1. Turn the heater auto-transformer in the off position to avoid rig overheating;
2. Regulate the valves until a desired and stable Re is reached;
3. Power up the heater slowly, until the water ΔT is $\sim 4°C$;
4. Wait for the temperatures to stabilize;
5. Acquire the data for 30 seconds and average it. If the standard deviation is higher than 2% of the mean value, discard the data and acquire again;

This procedure is repeated starting from $Re \approx 500$ until one of the limiting factors of the rig are reached. This means that one of the following have been registered:

- Max pressure $P_{in} \approx 20\ bar$
- Max wall temperature $T_{wall} = 85°C$
- Max electrical power, thus not enough heating capabilities $\Delta T_{water} < 4°C$

Finally, the sensor data is then processed with the solvers as explained in Appendix 4.

3.5 Uncertainty Analysis

An uncertainty analysis has been done to check if the results are reliable and the instrumental errors are not excessively amplified by the numerical solver. As a reference, JCGM 100:2008 [33] methodology has been followed.

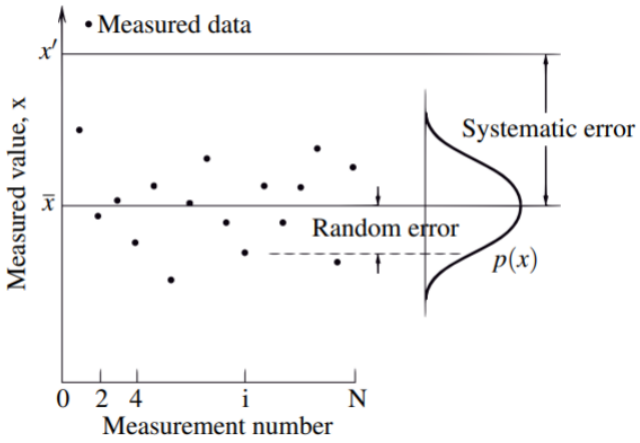

Figure 3.14: Description of different types of error

3.5.1 Error and uncertainty definition

The error is given by the imperfection of a measurement. Generally, a measurement has two types of errors, *Random error* and *Systematic error*. On figure 3.14 is possible to understand better the difference between the two types of error.
It is important to differentiate between uncertainty and error. The former comes from the lack of knowledge of the exact true value. The difference with the error is that it is possible to get a negligible error (value close to the expected value) and a high uncertainty (or low precision).
A typical way to estimate the uncertainty in complex functions, such as the *Star Solver* build for this thesis, is to perturb the input and measure the impact on the result with a Taylor expansion formulation of error [34]. Given Y function of n independent and normally distributed variables X_i:

$$Y = f(X_1, X_2, \ldots, X_n) \tag{3.2}$$

The propagation of the perturbations in the function can be expressed as a Taylor expansion limited to first order:

$$\delta Y = \frac{\partial Y}{\partial X_1}\delta X_1 + \frac{\partial Y}{\partial X_2}\delta X_2 + \ldots + \frac{\partial Y}{\partial X_n}\delta X_n \tag{3.3}$$

In this thesis project, the deviations δX_i are the instruments' uncertainties $u(X_i)$ presented in table 3.1. This was done in order to reduce the solver's runs.
The uncertainties can be evaluated using the standard deviations, because the error

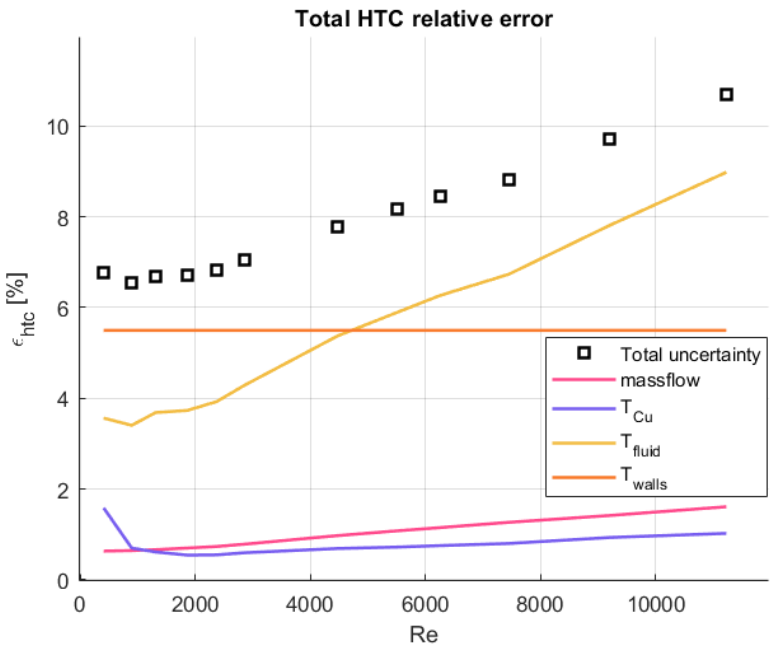

Figure 3.15: Example of an uncertainty analysis for Nusselt test

distribution of the experiment is assumed as normal:

$$u(Y) = \sqrt{\left(\frac{\partial Y}{\partial X_1}u(X_1)\right)^2 + \left(\frac{\partial Y}{\partial X_2}u(X_2)\right)^2 + \ldots + \left(\frac{\partial Y}{\partial X_n}u(X_n)\right)^2} \tag{3.4}$$

$u(X_i)$ is the maximum variation of the measurement for instrument "i". The result is then normalized with the original value of Y measured in those conditions. Overall, the uncertainties for the tests were:

- *Darcy test*: Relative uncertainty $\varepsilon_{Darcy} < 10\%$. The main contributing factors is the hydraulic diameter evaluation. The highest uncertainty is reached in the laminar region, where the pressure transducers are measuring close to their sensibility.
- *Nusselt test*: Relative uncertainty $\varepsilon_{Nusselt} < 15\%$. The main contributing factor is the temperature measurement of the water's inlet and outlet. Even a small difference at high Re can mean a great difference in heat flux on the channel's wall. An example of the Nusselt test's uncertainty can be seen in figure 3.15.

Chapter 4

Pseudo-code of the numerical solver

In this appendix is explained how the Nusselt number is calculated from the experimental data acquired during the test. The base software used is Siemens Simcenter StarCCM+, but this software is limited to 2D and 3D simulations. A macro has been written in Java, where the 3D model has been simplified by doing an energy balance in the test object's radial direction.

4.1 Setup

The test object is modeled in 3D using the real external dimensions. The internal channel is a round hole with a smooth wall. The internal diameter is the hydraulic diameter of the tested channel. Inside the channel there are no fluid models, the heat transfer is modeled only as a boundary condition to remove unnecessary and heavy to compute fluid dynamics calculation.

4.1.1 Boundary conditions

Figure 4.1: Meshed test object with boundary conditions

The test object boundary conditions are represented on the meshed test object on figure 4.1. In detail:

- *External walls (purple)*: adiabatic wall condition, no heat transfer
- *Internal wall (green)*: convective heat transfer, with imposed water temperature distribution and htc along the axis. Note: these distributions will be iterated in the calculations to achieve the final result.
- *Copper clamps (red)*: conductive heat transfer, fixed htc and external copper temperature from the thermocouple measurement. An electrical voltage difference is imposed between the two copper bars, which will also be iterated by the solver.
- *PT100 locations (dark blue)*: they are a stopping criterion for the solver, forcing the htc distribution on the internal wall.

The htc distribution along the axis is split in 8 segments, where each segment has constant htc. The split point of the segments corresponds to the midpoint between two PT100s: therefore the first and last segments are longer than the central ones. The water temperature distribution is discretised by dividing the length of the wall in 200 elements. Both values are calculated using radial symmetry, thus every element is a 1D branch. To extend the values to the 3D model the 1D branch is extended along the circumference to cover the whole internal wall of the channel. The value for the heat transfer coefficient on the copper clamps has been fixed at $htc_{Cu} = 15000\ W/m^2K$. Higher values have low effect on the final result.

4.1.2 Initial conditions

To start the solver it is necessary to assign a tentative value for the variables that will be iterated:

- *Water temperature distribution*: linear distribution between the real measurements at the inlet and outlet of the channel
- *Voltage differential*: the initial value strongly depends on the electrical conductivity of the material (which is kept constant).
- *Htc distribution*: similar to the water temperature, the value is set in a linear distribution from inlet to outlet, and it depends on the material thermal conductivity.

If a wrong initial voltage and/or htc distribution are chosen, the solver will crash after some iterations. An optimal value is one that lets the solver find a solution in the least amount of time.
These other properties of the test object are fixed:

- Thermal conductivity κ

- Electrical conductivity σ
- Geometry (via parameters)
- Experimental values:
  - Mass flow
  - Fluid temperature: T_{in} and T_{out}
  - Wall temperatures: $T_1, \ldots, T_8$
  - Copper temperature: $T_{Cu,in},\ T_{Cu,out}$

This code can run for only a fixed mass flow, so there is a loop in the code that changes the data points for calculating the whole test. The test points are sorted from the lowest flow to the highest. When there is a change of mass flow, the previous voltage and htc distribution are used as initialization values to speed up the simulation.

4.2 Initial calculation (for each Reynolds)

The first important step is converting all the experimental data into SI units. Afterwards, some fluid properties are obtained using *CoolProp* library [36], using mean values of the water temperature and pressure:

- Dynamic viscosity μ
- Specific heat capacity C_p
- Water heat conductivity k_{H_2O}

The water density is calculated from the ITS-90 standard [37]:

$$\begin{aligned}\rho =& 999.85308 + 6.32693 \cdot 10^{-2}T - 8.523829 \cdot 10^{-3}T^2 + \\ &+ 6.943248 \cdot 10^{-5}T^3 - 3.82126 \cdot 10^{-7}T^4\ [kg/m^3]\end{aligned} \tag{4.1}$$

Then, bulk velocity of the flow is calculated from the mass flow, along with Reynolds and Prandtl numbers:

$$u = \frac{\dot{m}}{\rho\pi\frac{d_h^2}{4}} \tag{4.2}$$

$$Re_D = \frac{\rho u d_h}{\mu} \tag{4.3}$$

$$Pr = \frac{\mu C_p}{k_{H_2O}} \tag{4.4}$$

4.2.1 Entrance effect corrections

The pressure measurements are corrected because the pressure taps are outside of the test object. As seen in chapter 2.3.4, for the 90° angle entrance end exit, the corrective coefficients are:

- In the laminar region:
  - $Loss_{in} = 0.5$
  - $Loss_{out} = 2$
- In the transition/turbulent region:
  - $Loss_{in} = 0.5$
  - $Loss_{out} = 1$

The transition is determined with a numerical sensor: a non-corrected Darcy friction factor is calculated; when the slope of the Darcy results becomes positive, the turbulent coefficients are applied. The final pressure differential is:

$$\Delta P = (P_{in} - P_{out}) - 0.5 \cdot \rho u^2 (Loss_{in} + Loss_{out}) \tag{4.5}$$

4.3 Darcy friction factor

The code until the end of this paragraph can be run separately to have instantaneous friction factor results, without the need for running StarCCM+.
With the corrected ΔP from the previous paragraph, the Darcy friction factor is obtained:

$$f_d = \frac{2 d_h \Delta P}{\rho u^2 L} \tag{4.6}$$

4.3.1 Colebrook-White correlation

The friction factor is compared with the smooth channel, represented by the Colebrook-White equation:

$$\frac{1}{\sqrt{f_d}} = -2 \log \left(\frac{\varepsilon}{3.7 d_h} + \frac{2.51}{Re\sqrt{f}} \right) \tag{4.7}$$

For a smooth channel $\varepsilon = 0$, and then the equation is solved using an iterative method to get f at various Re numbers.

4.4 Nusselt number

This part of the code is written in Java as a StarCCM+ macro. The first step is to import the experimental results (sensors measurements) and the test object properties into the Star file. With the parametric geometry created, the test object geometry is discretised in a mesh. This process is done only once per test, because the geometry does not change. Outside of the loops the heat flux entering the water is calculated. This is the final stopping criteria for the solver:

$$\dot{Q}_{water(real)} = \dot{m} C_p (T_{f,out} - T_{f,in}) - \frac{\dot{m}}{\rho} \Delta P \tag{4.8}$$

4.4.1 Solver loops

Outer loop

This loop runs until the calculated water heat flux on the solver matches the measured one. It is used to balance the overall power of the system.
The first thing to run is the internal loop until its own convergence:

Inner loop

This loop runs until the temperature distribution on the outer wall is matching the experimental PT100 measurements in their respective locations.
The first action is the calculation of the temperature's residual:

$$res(i) = \left| \frac{T_{wall(real)}(i) - T_{wall(calc)}(i)}{T_{wall(real)}(i)} \right| \tag{4.9}$$

If all the residuals (e.g. 8 if the channel is 150mm long) are less than the tolerance, then exit the inner loop.
The second action that the solver does is integrating the water temperature along the cylinder axis. For each water branch, this routine is executed on Star:

1. Select the internal channel's area surrounding the branch by moving a threshold to the position $[x, x + dx]$;
2. At this threshold, get area of the wall's partition, T_{wall} and htc;
3. Calculate water temperature from solving this energy balance:

$$T_{water}(i+1) = T_{water}(i) + \frac{htc \cdot A}{\dot{m} C_p} \left(T_{wall}(i) - T_{water}(i) \right) + \frac{P(i+1) - P(i)}{\rho C_p} \tag{4.10}$$

4. Update the temperature distribution table with the new calculated temperatures.

With the updated table, iterate the htc distribution. For each PT100:

1. Move a threshold to the PT100 position, selecting the outer wall of the TO;
2. Read external T_{wall} value calculated by the simulation;
3. Update the htc value by modifying it proportionally to the temperature error. Note: the "20" relaxation factor has been achieved after trying various values. This is a good compromise between convergence speed and code stability.

$$htc_{new}(i) = htc_{old}(i) \cdot \left(1 + 20\frac{T_{wall}(i) - T_{wall(real)}(i)}{T_{wall(real)}(i)}\right) \tag{4.11}$$

4. Update the htc distribution table

With the tables updated, run StarCCM+ simulation (combined thermal and Joule Heating models) for 50 iterations; these are enough for the solvers to converge.

Outer loop (when inner has converged)

When the conditions to exit the inner loop are achieved, enter the outer loop again. First the water temperature is integrated again following equation 4.10, as seen in the inner loop. Subsequently, update the electrical voltage differential on the copper clamps to reach power balance:

1. Define the power imbalance between the simulation (calc) and the real one calculated previously in eq. 4.8:

$$res_P = \frac{\dot{Q}_{water(calc)} - \dot{Q}_{water(real)}}{\dot{Q}_{water(real)}} \tag{4.12}$$

2. Update the voltage differential iterating with the previously calculated residual:

$$V_{new} = V_{old}\,(1 - 0.3 \cdot res_P) \tag{4.13}$$

Run the simulation for 50 steps to introduce the new electrical power. If the residual of the total power is less than a tolerance $res_P < TOL_P$, exit the outer loop and save the results. If the residual is higher than the tolerance, enter again the inner loop with the new voltage and repeat the cycle.

Chapter 5

Results

In this chapter all the experimental results are presented. First, a validation of the whole rig was ran, using a test object that had previously been tested and validated. Then, individual results for friction factor and heat transfer will be presented and discussed, focusing on the effects that material and roughness parameter have.

5.1 Validation

For this thesis project the experimental rig was slightly changed and the numerical solver was created almost from scratch. These structural modifications require a validation with some known correlations, like Colebrook-White [8] and Gnielinski [29]. A smooth 90mm channel made out of machined aluminum is used. Its internal hydraulic diameter is $d_h = 2.1183\ mm$.

5.1.1 Rig validation

The first test done with the new rig inlet/outlet geometry is with the smooth channel described previously, to be compared in the turbulent region with the Colebrook-White correlation [8].

From figure 5.1 it is possible to understand that the rig is returning correct results: the points follow Poiseuille's laminar flow and Colebrook-White turbulent regime correlation. In the transition region, the points are separated from the lines; this is a normal behavior, because in the transition zone there is no possibility to predict the flow behavior accurately, and the TO may have some small imperfections that make its results differ from an ideal smooth channel.

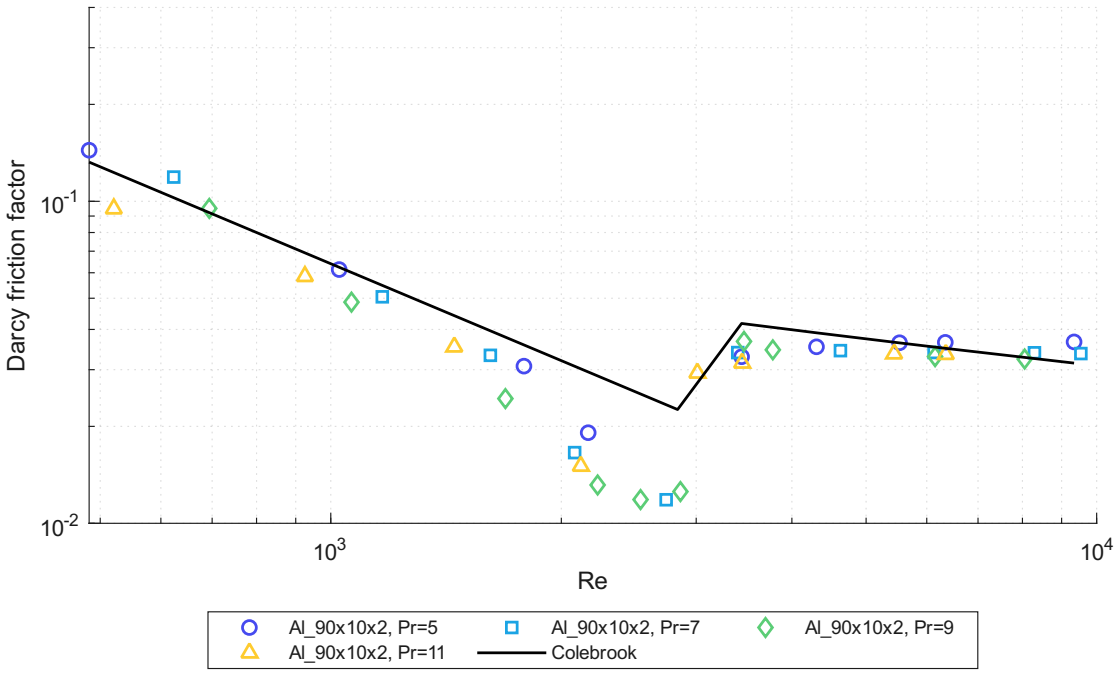

Figure 5.1: AL_90x10x2 smooth channel, Darcy friction factor

5.1.2 Code validation

To validate the code, a Nusselt test on the smooth channel has been performed. If the solver behaves properly, its output should follow Gnielinski's correlation [29]. On figure 5.2 is reported the Nusselt trend at different Prandtl numbers, and Gnielinski's correlation at $Pr = 5$ for reference. The lines follow the same trend as Gnielinski, and the Nu increases with the Pr. The lines overlap because with $Re < 10000$ the flow is still transitioning to fully turbulent, and Dittus-Boelter is no longer valid.
The enhancement (fig. 5.3) is between $0.9 \leq Nu/Nu_0 \leq 1.25$ for all results. Before interpreting the results, an uncertainty of $\varepsilon_{StarSolver} \lesssim 15\%$ for the experimental measurement and $\varepsilon_{Gnielinski} \approx 15\%$ for the correlation ($> 15\%$ for low turbulent regime) have to be acknowledged. After these considerations the measured values fall within the correlations' results, thus the Nusselt trend is correct and the experimental methodology is validated.

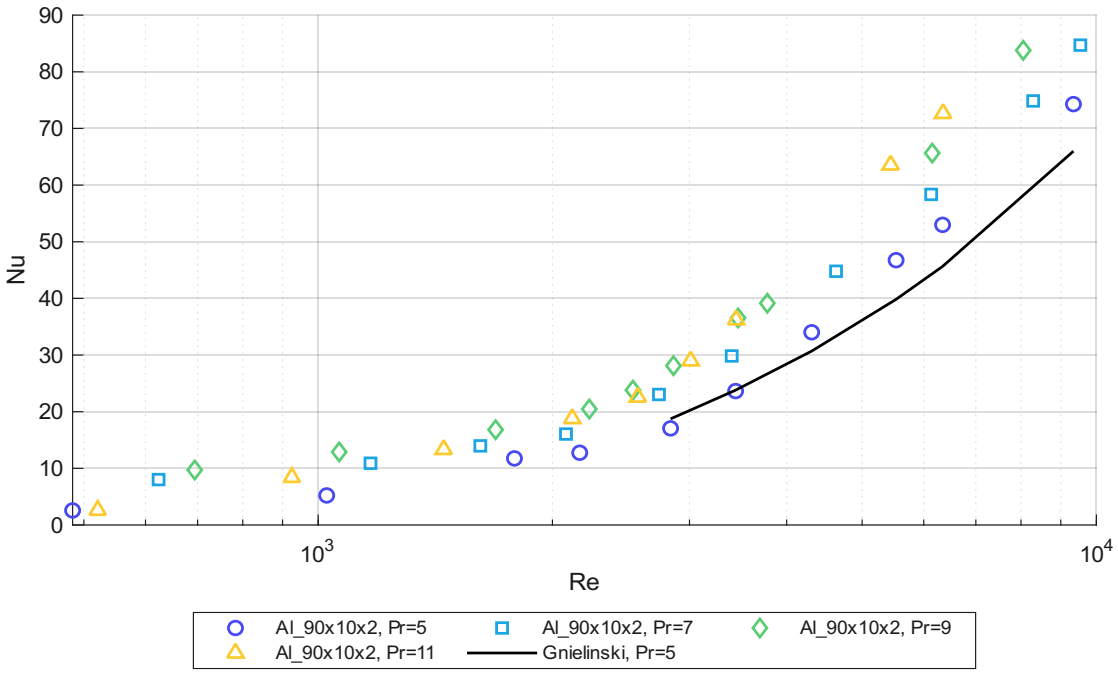

Figure 5.2: AL_90x10x2 smooth channel, Nusselt number

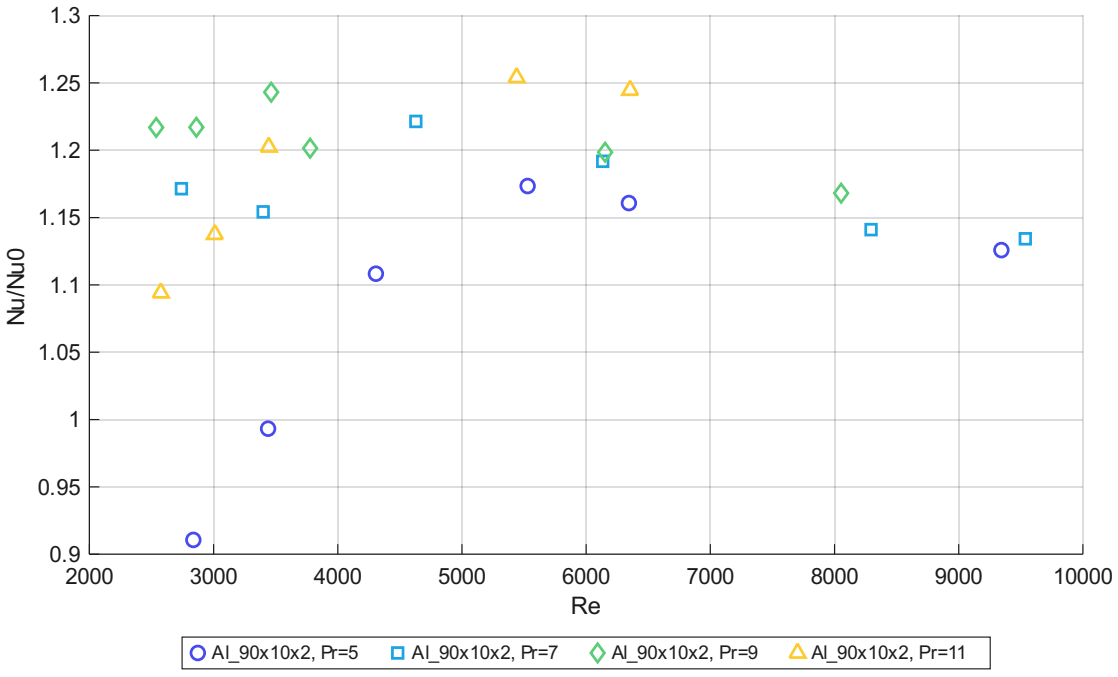

Figure 5.3: AL_90x10x2 smooth channel, Nusselt enhancement

5.2 Friction factor

In this section the results of the friction factors are plotted and commented. In each plot there is a line representing the smooth channel with the same hydraulic diameter, using Poiseuille's law for the laminar region and the Colebrook-White correlation [8] for the turbulent flow, introduced in section 2.3.3. Only the Darcy results of the Al TO1 are commented singularly so as to prove the independence of Prandtl number; however, for the other TOs the same conclusions apply.

5.2.1 Aluminum

From the profilometer measurements found on table 2.1, aluminum printed components have the lowest absolute roughness. However, the important parameter is the roughness relative to the hydraulic diameter ε. This is particularly true for

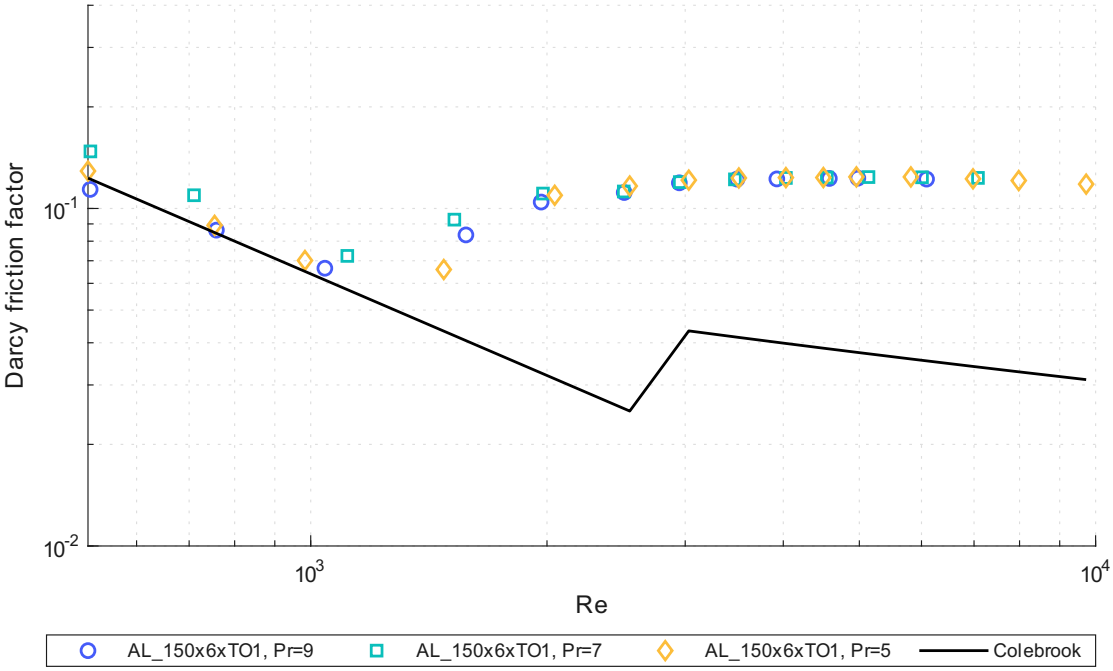

Figure 5.4: AL_150x6xTO1 Darcy friction factor

the smallest test object, the TO1, which has a relative roughness of $\varepsilon = 0.0627$. The transition from laminar to turbulent flow starts way earlier than the smooth channel correlation, at about $Re \approx 1000$. As expected, the friction factor does not depend on the Prandtl number, so the results are overlapped. Being a really small test object, it was difficult to achieve steady state conditions at low Re, because the mass flow was $\dot{m} < 0.3g/s$ and it is difficult to adjust this with cone valves

rated for high mass flows.

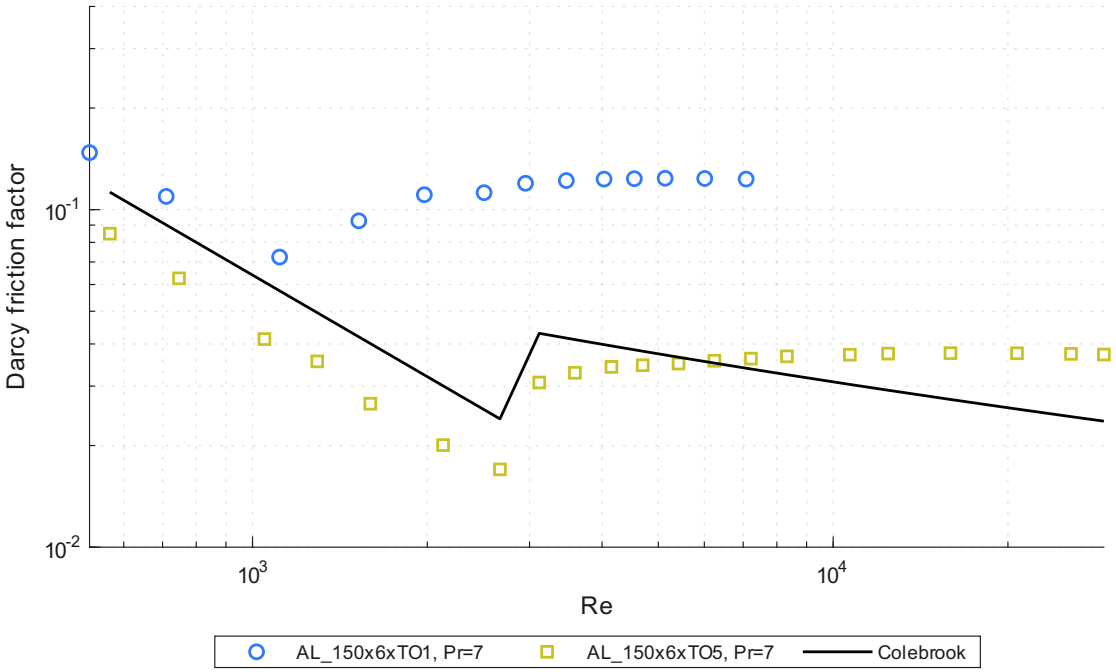

Figure 5.5: Aluminum TOs Darcy friction factor

In the laminar region (fig. 5.5), the TO5's friction factor is lower than the smooth channel. This is probably due to an issue in the hydraulic diameter's evaluation as the inlet of the TO is damaged, as can be observed in figure B.1.
Still, the transition of the TO5 is almost the same as a smooth channel because its relative roughness is low. However, in the turbulent region it behaves like a rough channel, because the friction factor becomes constant with the Re.

5.2.2 Stainless Steel

The test objects made out of stainless steel are the ones with the highest hydraulic diameter of the batch. On table A.3 it can be seen that both SS_2 ans SS_3 have a similar relative roughness to AL_TO5, so the same Darcy friction factor is expected. The results differ from what was expected, especially for the 3mm test object. The offset between laminar points and the Poiseuille flow (fig. 5.6) indicate that the evaluation of the hydraulic diameter could be incorrect. The channel may not have a constant diameter, and the strong dependency of the friction factor on it affects the results.
For both cases the only valuable data is the transition Re number, which is close to the smooth channel one. In both cases, the jump between laminar and turbulent

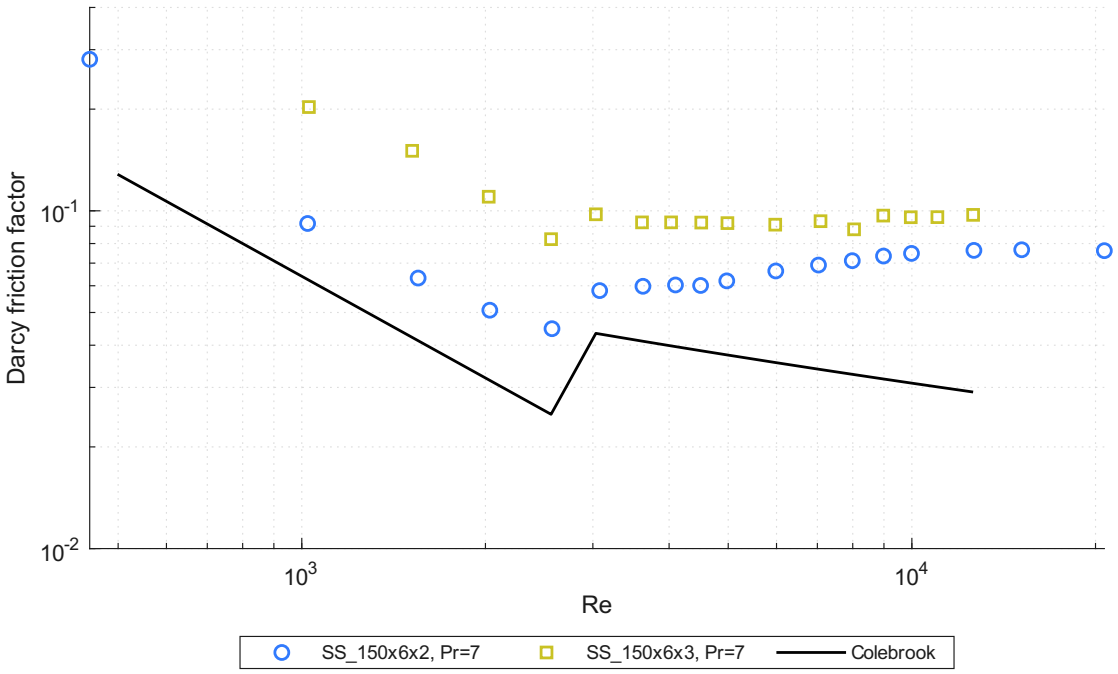

Figure 5.6: Stainless Steel TOs Darcy friction factor

is smaller than the smooth channel. Being a transition zone, the lowest friction factor point was not found during the experiment; this happened because the boundary layer is in a unsteady transition between laminar and turbulent, making it impossible to gather steady-state results.

5.2.3 Inconel 939

The IN939 TOs have the highest R_z and a wide range of hydraulic diameters, so these tests were the most significant ones for observing the effect of relative roughness on the friction factor. Also in this case the laminar line is not the same as the smooth channel, but all the test objects are following the same laminar trend. This problem could be due to an insufficient sensibility of the transducers, reading a pressure differential higher than the real one. When the Re increases, the ΔP also grows and the relative error on the measurement lowers.

All of the friction factor trends are constant in turbulent flow, and it increases with the relative roughness. At the same time, the transition point is at lower Re.

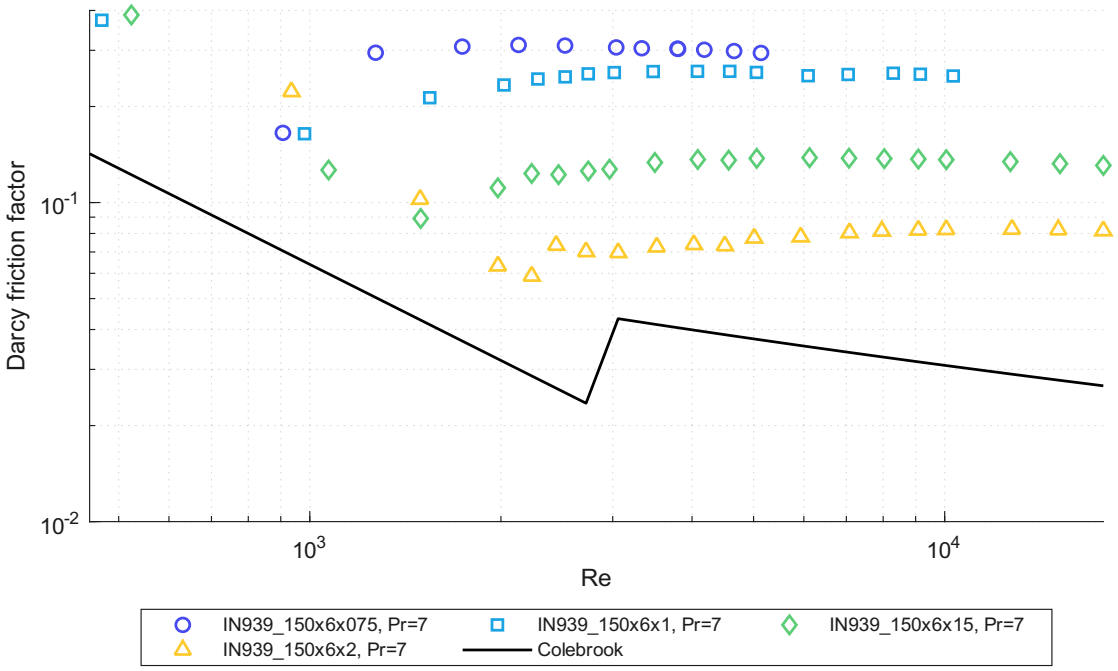

Figure 5.7: Inconel 939 TOs Darcy friction factor

5.2.4 Material effect

To further validate the results, a comparison has been made between IN939 1.5mm and Aluminum TO5. Those test objects have almost the same relative roughness, so their Darcy friction factor should be the same. In fact, by looking at fig. 5.8 it is clear that in the turbulent region both test objects behave in the same way, but in the laminar flow region only the TO1 is following Poiseuille's flow. This issue can also be addressed at faulty pressure transducers, because the Inconel test object has double the hydraulic diameter, therefore lower pressure difference to measure.

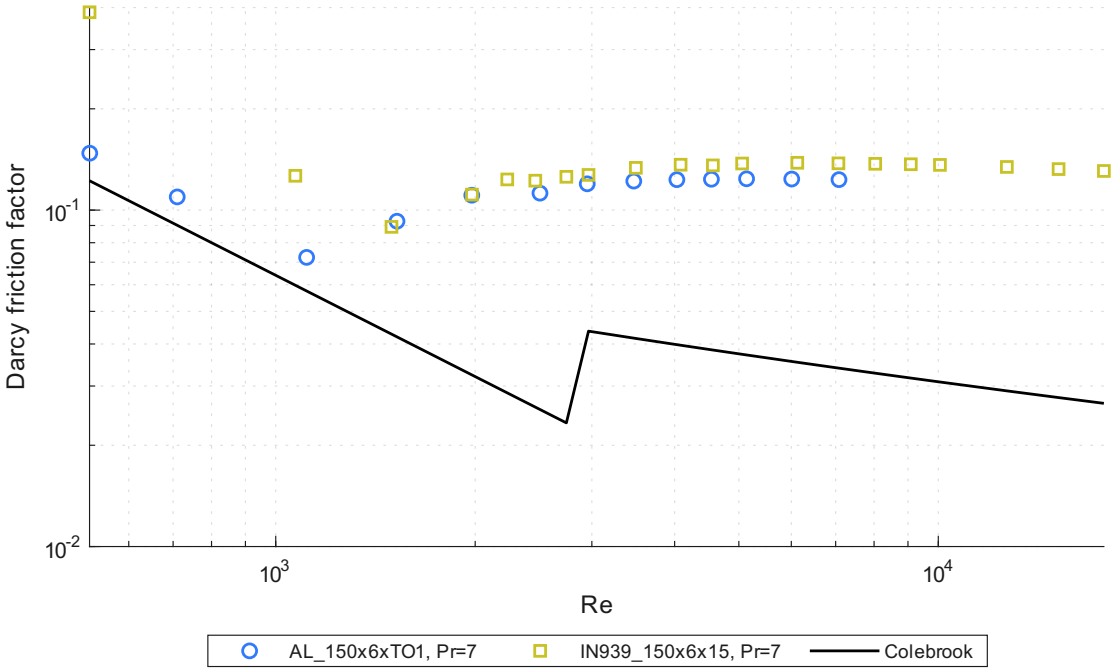

Figure 5.8: Material comparison, Darcy friction factor

5.3 Nusselt number

In this section the heat transfer performance of the TOs is illustrated, in non-dimensional form with Re on the x axis and Nu on the y. A logarithmic scale has been adopted for showing better the transition between laminar and turbulent flow. Another plot has been created by normalizing the Nu results with the smooth channel correlation at the same Re and Pr.

5.3.1 Aluminum

Aluminum has a conductivity an order of magnitude higher than Inconel or Stainless steel, which changes completely its test behavior. The limit during the testing of aluminum channels was the inlet pressure and the current flowing into the primary loop, which was triggering the safety relay.
Being a small test object with high relative roughness, the TO1 has an early transition from laminar to turbulent flow $Re \approx 1500$, this can be identified by the substantial increase in heat transfer performance in figure 5.9. As stated by Dittus-Boelter, a higher Pr has a positive effect on non-dimensional heat transfer Nu.
Normalizing the results with Gnielinski's correlation [29] (figure 5.10 is visible a

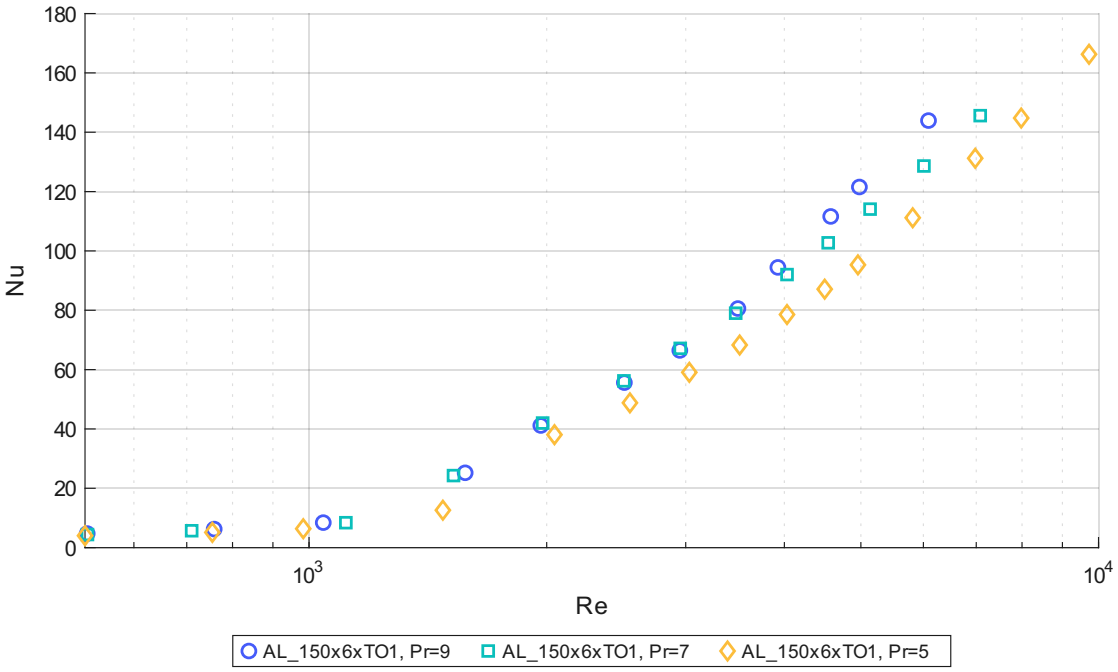

Figure 5.9: AL_150x6xTO1 Nusselt number

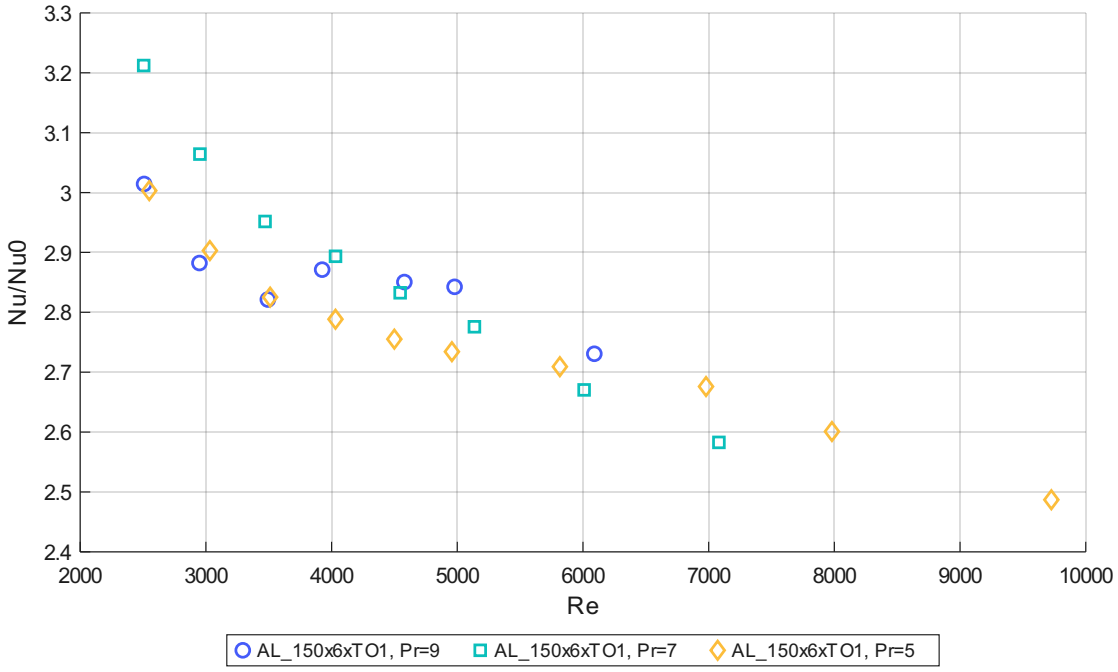

Figure 5.10: AL_150x6xTO1 Nusselt enhancement

decreasing trend in Nusselt enhancement. When the flow becomes fully turbulent, the enhancements of the rough surface become less evident. Still, in absolute values, heat transfer on TO1 is at least twice more effective than a smooth channel.

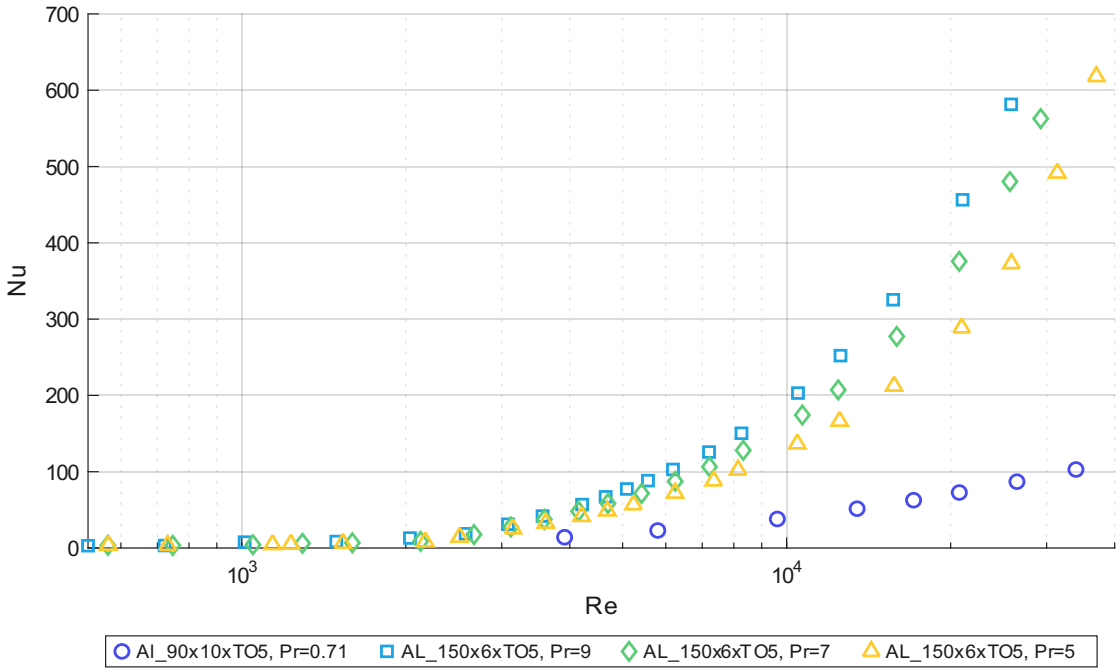

Figure 5.11: AL_150x6xTO5 Nusselt number

The TO5 (fig. 5.11) has almost one third of the TO1's relative roughness. This changes its heat transfer behavior, with a laminar to turbulent transition close to the smooth channel $Re \approx 2000$. In absolute values, the Nu seems to grow exponentially for the aluminum test objects. The Pr effect is clearly visible in the last points, again with a higher Pr that means higher heat transfer.
In this graph it was possible to add the comparison with a similar test object used in the qSSHT Air Rig (AL_90x10xTO5) so as to extend the Pr range. Despite having a different length and a slightly different hydraulic diameter, a similar trend can be seen between the two rigs.
The enhancement on the TO5 (fig. 5.12) has an opposite trend than the TO1: initially it rapidly grows, then the growth slows down, almost reaching a plateau. Only with the air rig is possible to identify this behavior, which suggests that at higher Re the same phenomenon may be observed on the water rig.
Comparing the aluminum test objects' enhancements (fig. 5.13), they have an opposite trend: the TO5 is slowly increasing, while the TO1 is decreasing. Due to its higher relative roughness, the TO1 has an earlier flow transition $Re \approx 1500$. However, Gnielinski's correlation is valid for $Re > 2500$, so it is not possible to see

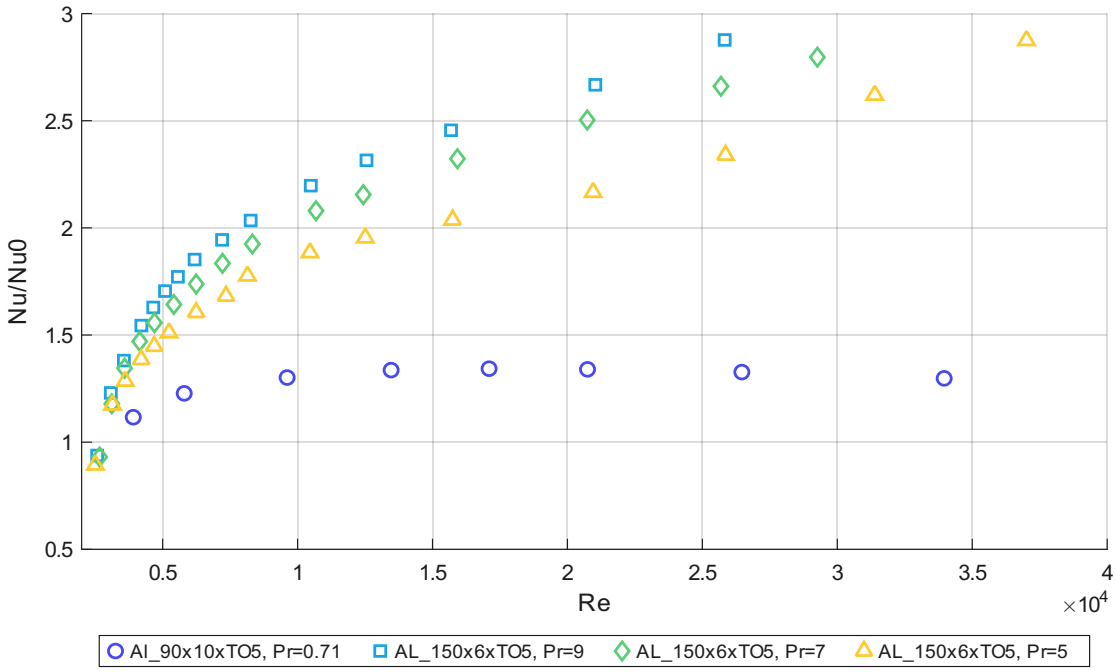

Figure 5.12: AL_150x6xTO5 Nusselt enhancement

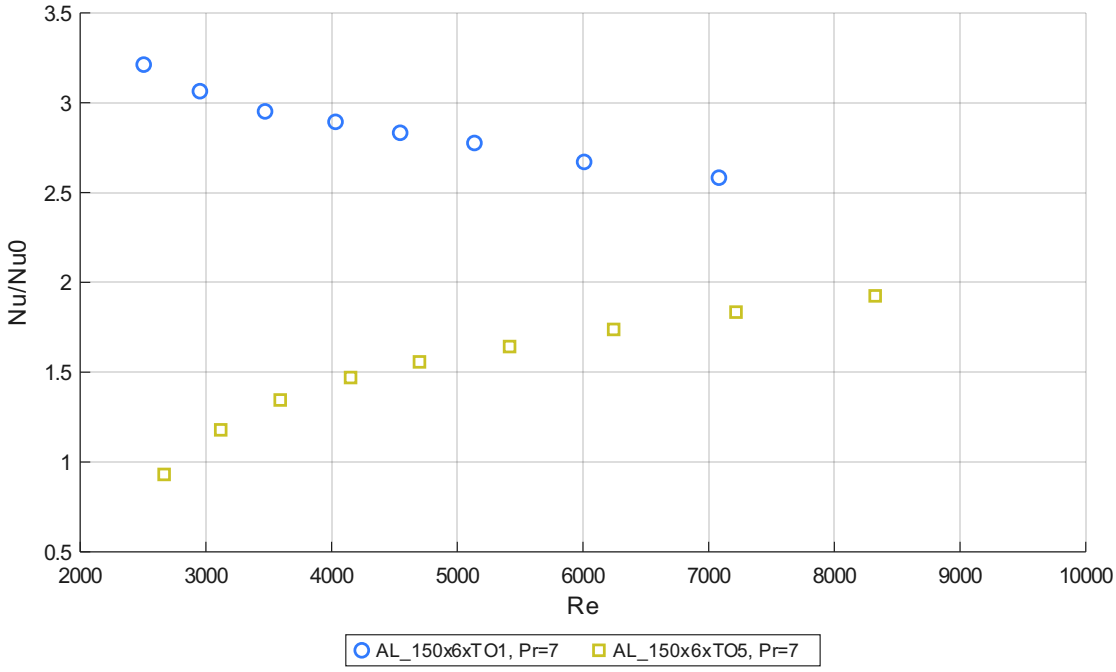

Figure 5.13: Aluminum TOs Nusselt enhancement

the enhancement at low Re. An hypothesis is that the TO1 behaves similarly to the TO5 right after the transition; when the plateau is reached it starts to have a decreasing trend, as seen in the 90mm TO5 in the air rig (fig. 5.12).

5.3.2 Stainless Steel

The TOs made in Stainless Steel had a similar behavior when evaluating the Nusselt. The relative roughness for this TO is really low, due to its bigger d_h. At high Re

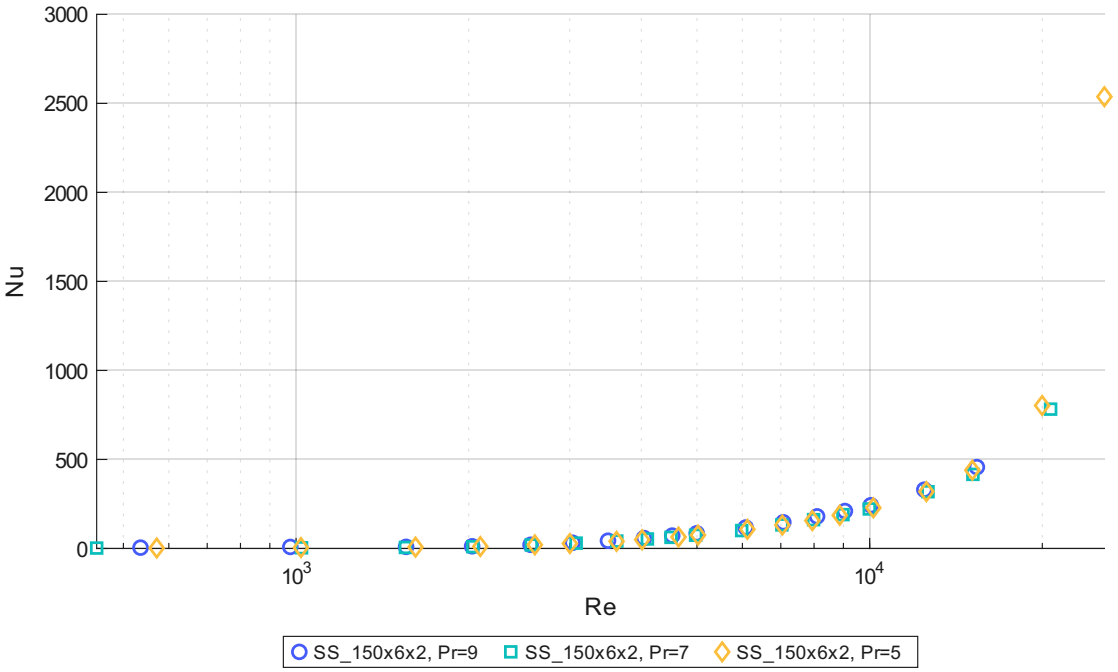

Figure 5.14: SS_150x6x2 Nusselt number

numbers (figure 5.14), the Nu tends to infinite: this is a physical limit of the test object, since its internal temperature tends to match the water's and it stops to exchange heat effectively. This phenomenon is visible in the Nusselt - x plot (figure 5.15): the internal wall temperature (blue line) becomes too close to the water temperature (yellow line). To achieve power balance, the code assigns an htc value that tends to infinite. Looking at the first points (fig. 5.16), the flow transition is at $Re \approx 2200$, almost the same as a smooth channel. Also, the transition gradually changes flow behavior until $Re = 10000$.
The enhancement (fig. 5.17) is growing with the Re, but at higher mass flows it tends to reach a plateau. Due to the heat saturation issue seen on figure 5.15, the plateau was not observed in the test results.
In the enhancement the Pr effect is reversed, with the enhancement decreasing with

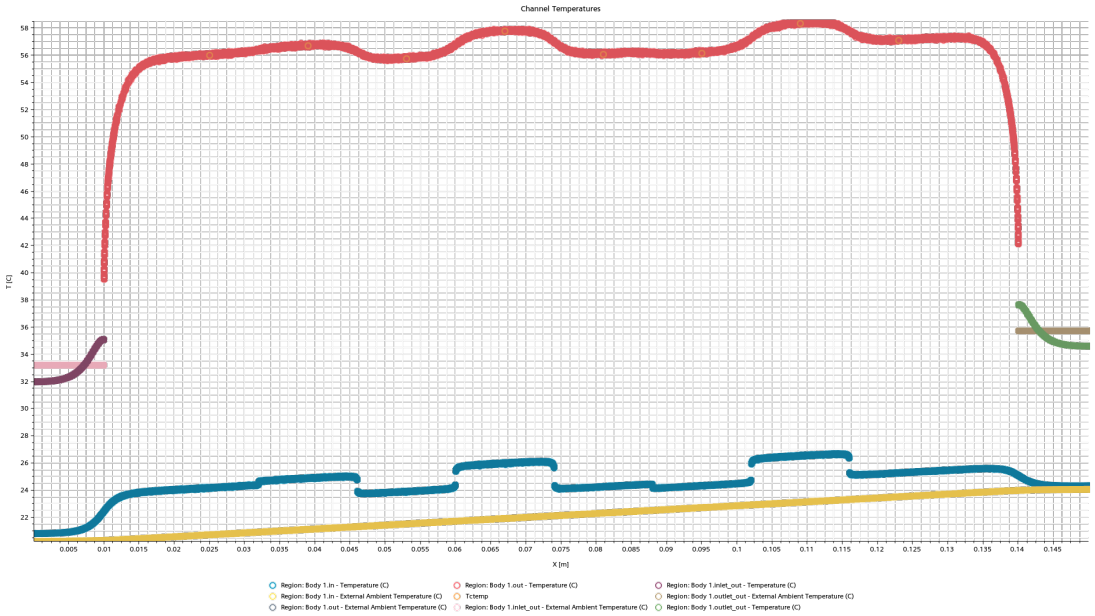

Figure 5.15: SS_150x6x2 Nusselt distribution, $Re = 20700,\ Pr = 7$

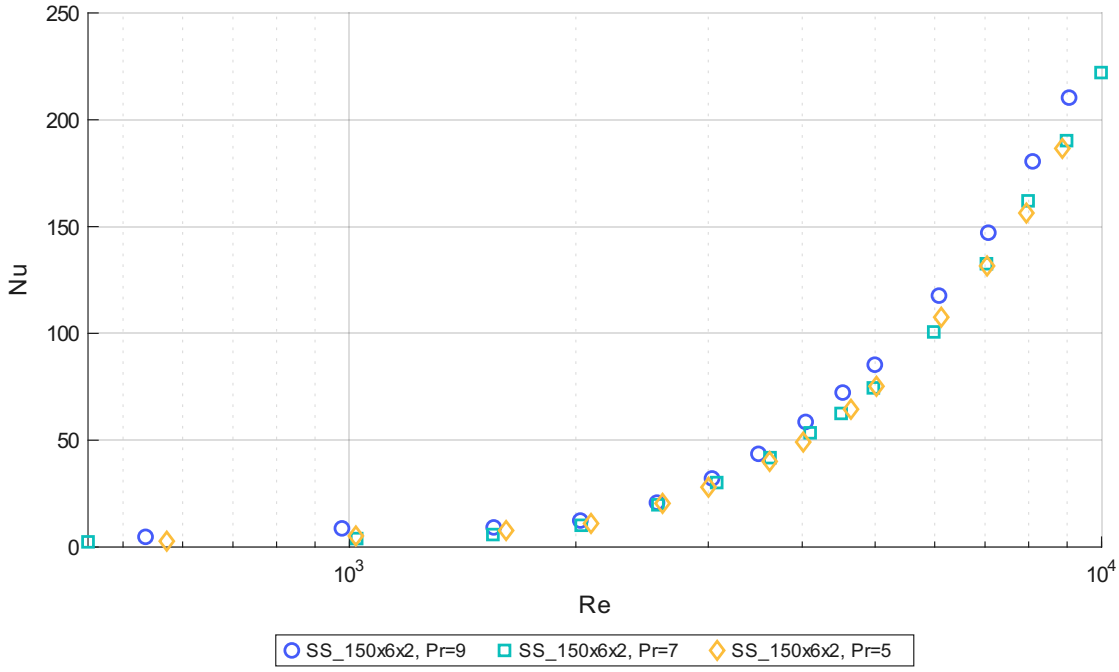

Figure 5.16: SS_150x6x2 Nusselt number (cropped)

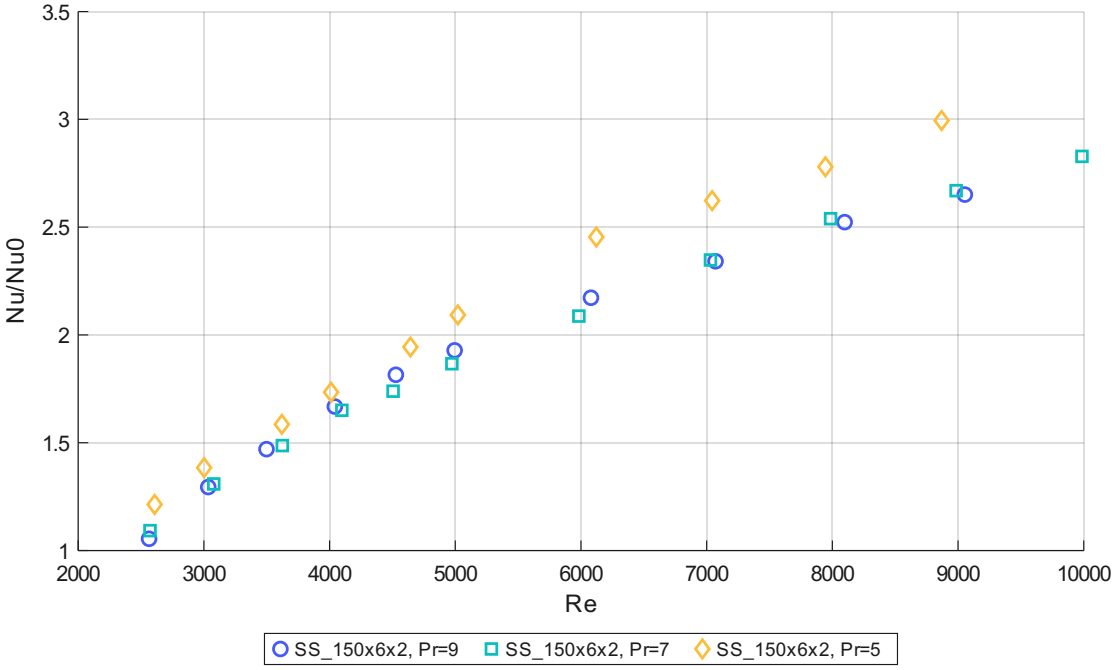

Figure 5.17: SS_150x6x2 Nusselt enhancement (cropped)

an increasing Pr. This may be caused by the vicinity of the curves of the absolute Nu values (fig. 5.16). When evaluating the enhancement, each Nusselt result is divided by the smooth channel value. Gnielinki's correlation is an extension of Dittus-Boelter, which is proportional to the Prandtl by an exponent of 0.4. The Nu results are less dependent on Pr and this causes the curve order to be reversed. The 3mm test object has the same trend, but at the same Re the Nusselt number is lower. Also in this test object the saturation effect made the Nusselt number tend to infinite. These points were discarded from the graph.
The same behavior is observed for the 2mm test object, but with two key differences: the enhancement is lower than the previous TO, and the flow requires a higher speed to reach the plateau Nu.

5.3.3 Inconel 939

Similar to the friction factor results, the Inconel-made test objects were the most significant ones for this project. The large variation in relative roughness allowed better its effect on heat transfer.
The 0.75mm nominal diameter was the most difficult test object, because of its small d_h and the highest relative roughness encountered. The transition happens at $Re \approx 1000$ (fig. 5.20), and the resulting points are really close to each other. It

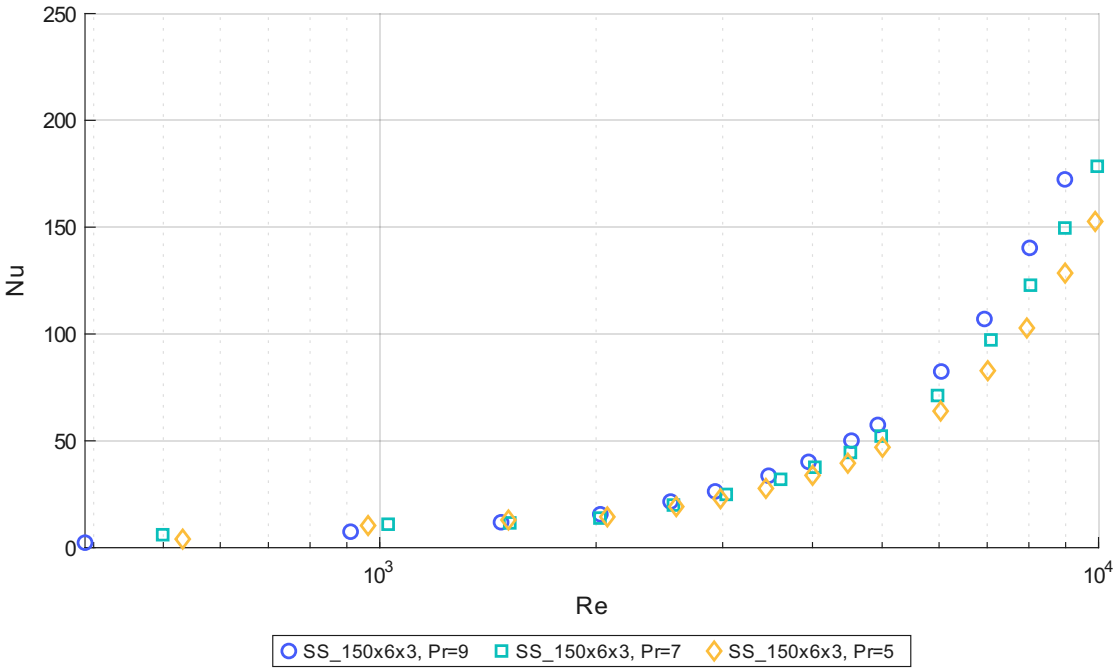

Figure 5.18: SS_150x6x3 Nusselt number (cropped)

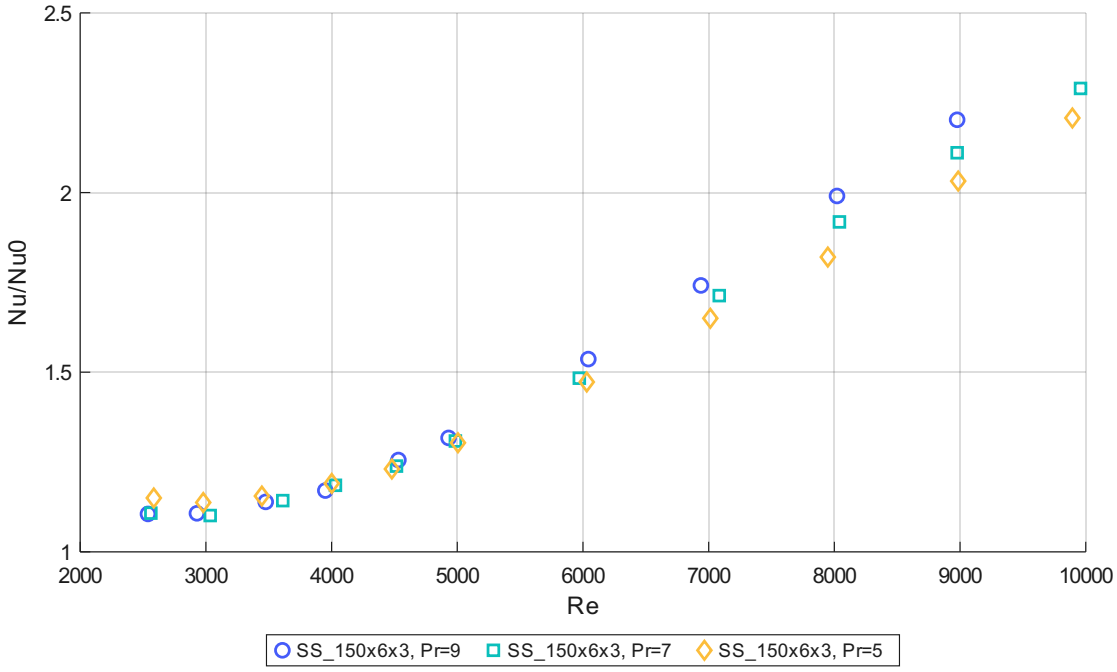

Figure 5.19: SS_150x6x3 Nusselt enhancement (cropped)

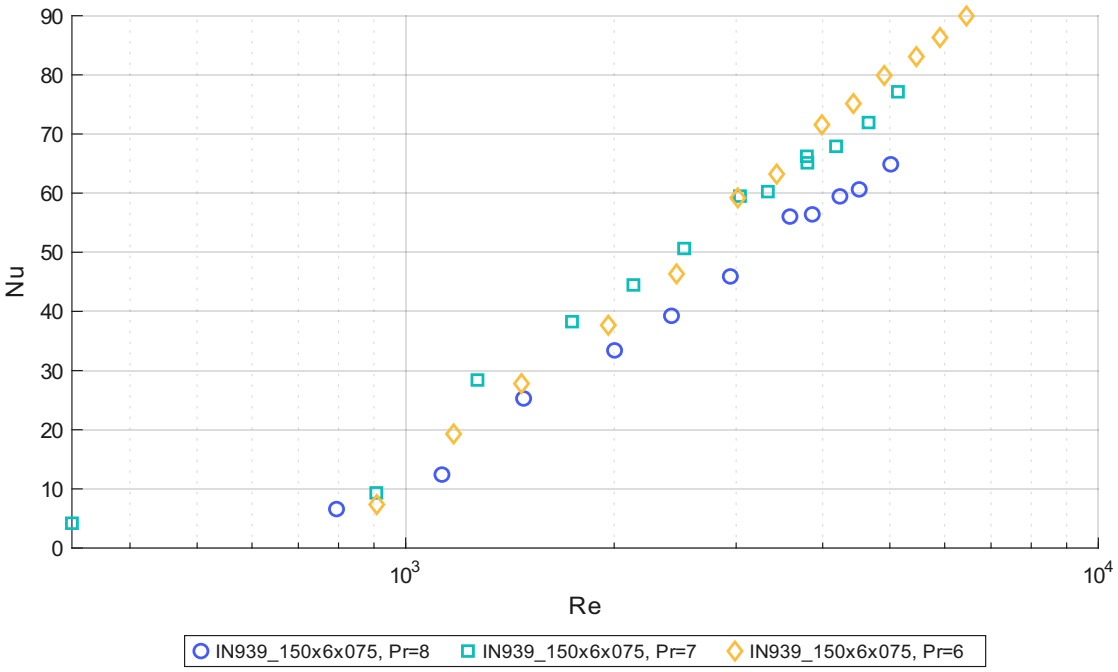

Figure 5.20: IN939_150x6x075 Nusselt number

was not possible to test at $Pr = 5$ or $Pr = 9$ because the TO was exchanging heat with the environment more than internally with the water, making the adiabatic walls assumption non valid.
The problematic test was reflected also on the enhancement results (fig. 5.21). The Pr effect is again reversed, like the Stainles Steel 3mm (fig. 5.19). In this case, the distance between $Pr = 6$ and 7 was higher than $Pr = 7$ and 8.
From the 1mm Inconel (fig. 5.22) it is possible to see that the transition point is moving towards the smooth channel one. Also in this case, the Pr effect is reversed. The vicinity of the curves could mean that they are overlapped, with the differences being only due to the instruments' and solver's uncertainties.
From figure 5.23 it is visible that the enhancement is decreasing. At high Re the channel's heat transfer performance is even lower than Gnielinski's correlation. The plateau has not been reached yet, so a rig that can sustain higher inlet pressure should be used to draw better conclusions.
The 1.5 mm Inconel transitions at $Re \approx 1500$. The effect of the Pr on the curves is even lower than the previous TOs and all the results fall into the rig's uncertainty. The enhancement seen in figure 5.25 is similar to the previous Inconel channels discussed, but the final plateau seems to stabilize at a higher Nu.
The 2mm test object had a similar channel tested with the air rig. Its results were added to the plot, but it should be kept in mind that it is long $90mm$ and has a

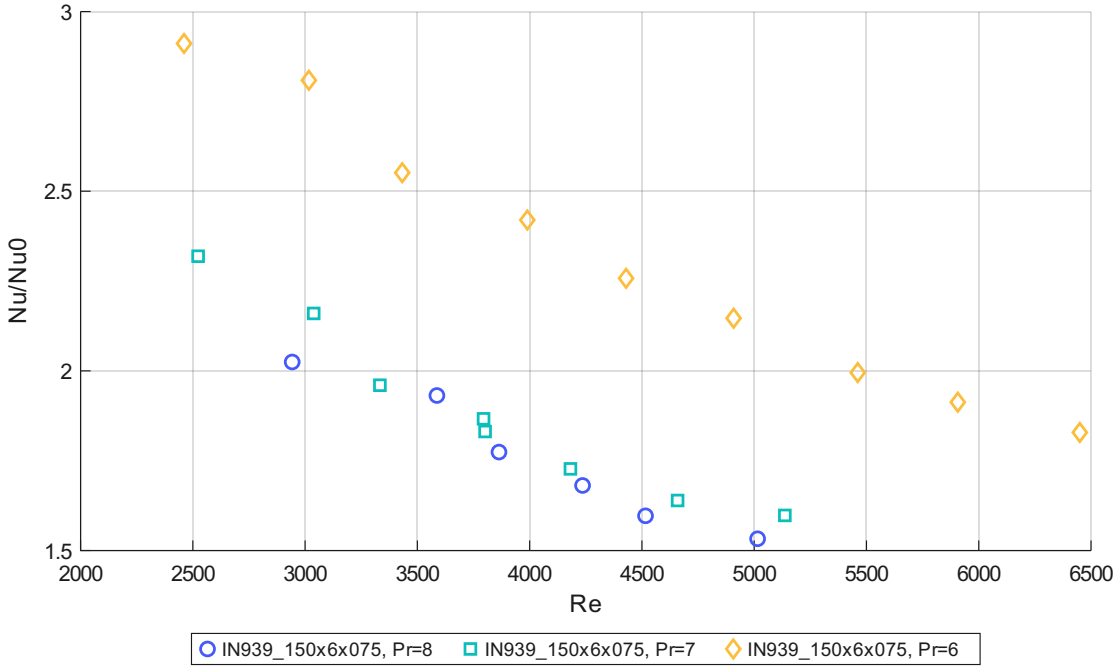

Figure 5.21: IN939_150x6x075 Nusselt enhancement

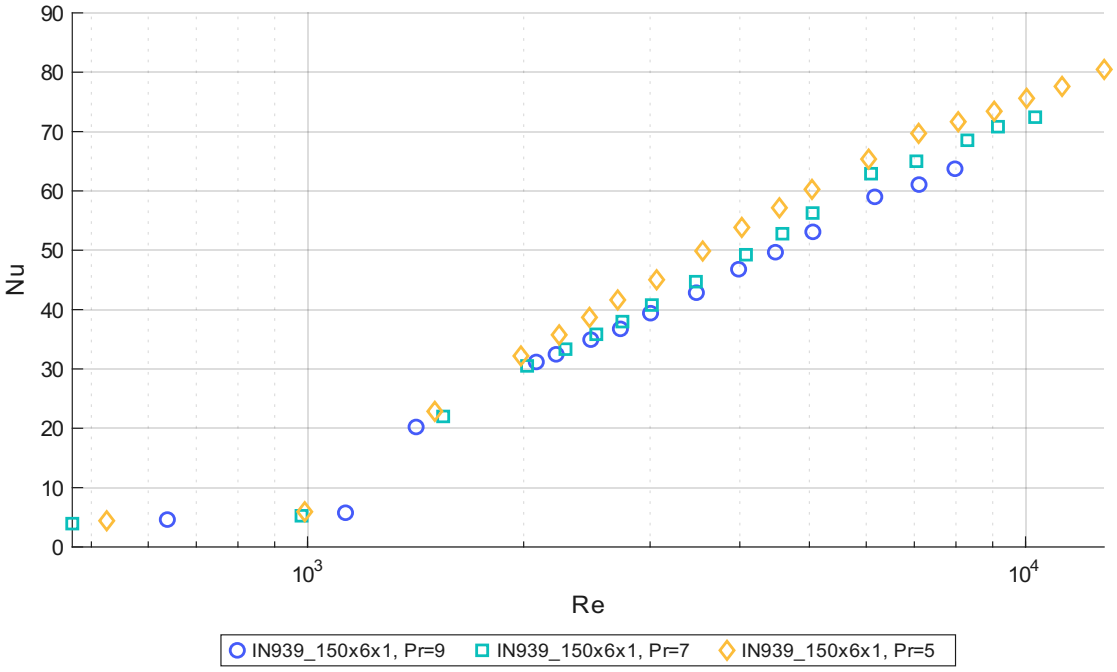

Figure 5.22: IN939_150x6x1 Nusselt number

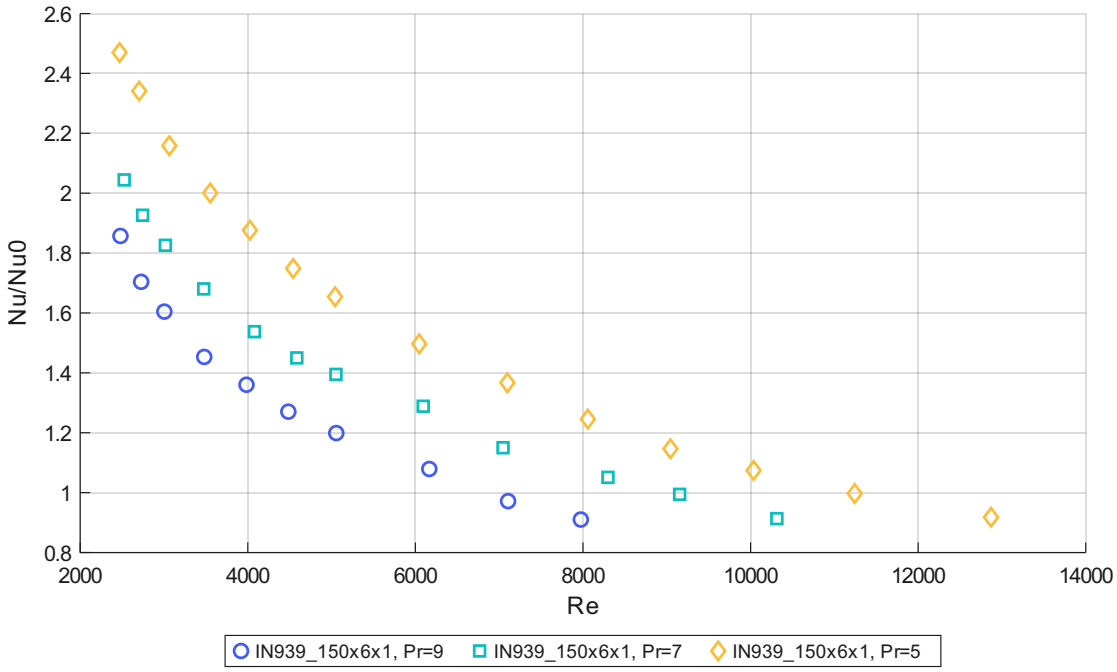

Figure 5.23: IN939_150x6x1 Nusselt enhancement

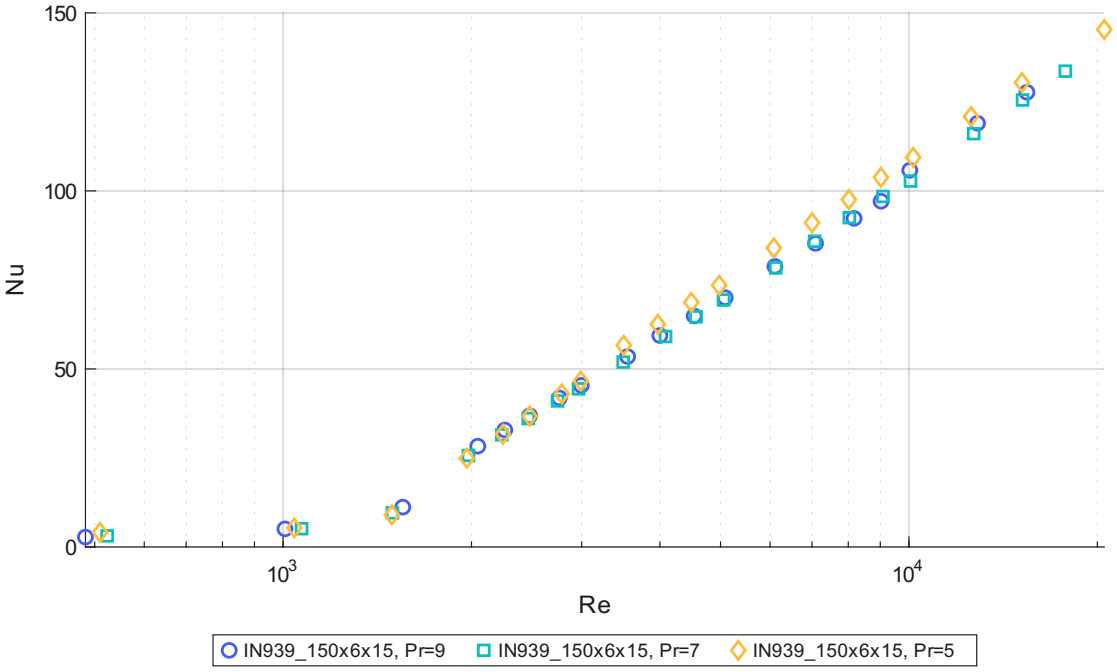

Figure 5.24: IN939_150x6x15 Nusselt number

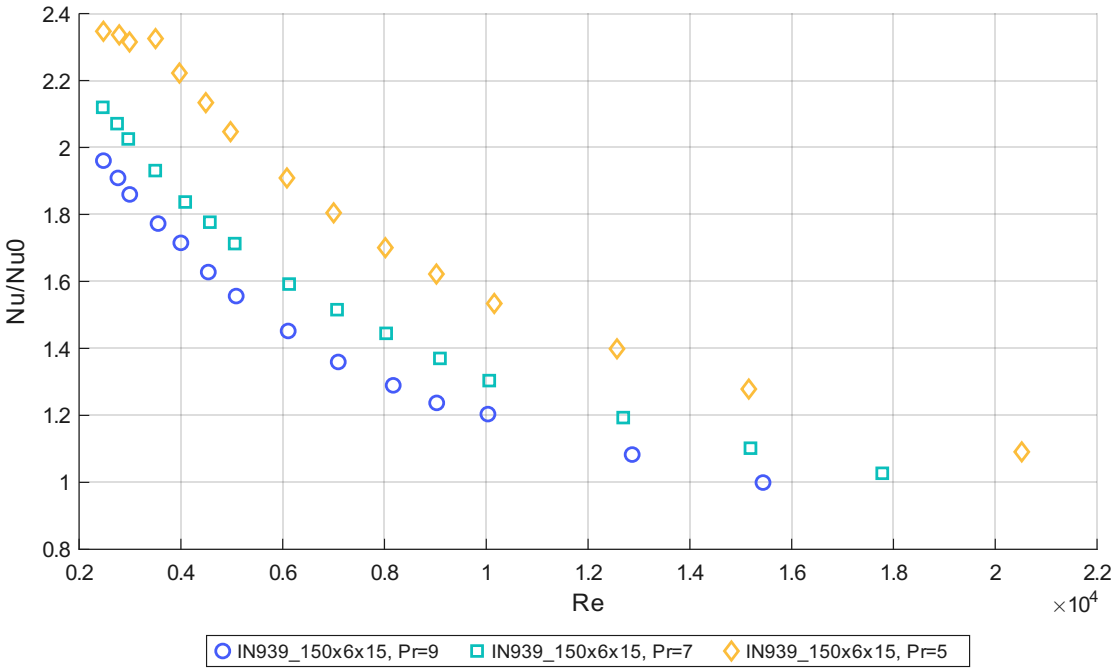

Figure 5.25: IN939_150x6x15 Nusselt enhancement

slightly different d_h. This test object has a transition close to the smooth, and it is visible from the thermal results that the behavior is similar to Stainless Steel and Aluminum TO5. In this case the Pr effect is again following Dittus-Boelter correlation.

The enhancement plot of the Inconel 2mm is the one that merges the different results found in the previous TOs: the first part at low turbulence has an increasing enhancement as seen with Stainless Steel and Aluminum TO5, and the high turbulence has a decrease in Nu/Nu_0 like the high-roughness test objects. The air rig's results indicate that Pr has an effect on the Nu slopes in both low and high turbulence regions. This effect is also slightly visible when comparing $Pr = 5$ with $Pr = 9$.

The Pr effect on the enhancement is unclear: Nu/Nu_0 decreases with increasing Pr, with the exception of the $90mm$ test object.

Comparing the results of all the Inconel test objects (fig. 5.28), it is possible to see that at low Re a higher relative roughness means higher heat transfer. When the smallest test objects reach high turbulence flow, their Nu growth slows down and bigger TOs can have better heat transfer performance. This is especially true for $1mm$ test object, which at $Re > 2000$ has poorer performance than both $1.5mm$ and $2mm$ ones.

On figure 5.29 is possible to distinguish the high-roughness TOs (0.75, 1 and 1.5

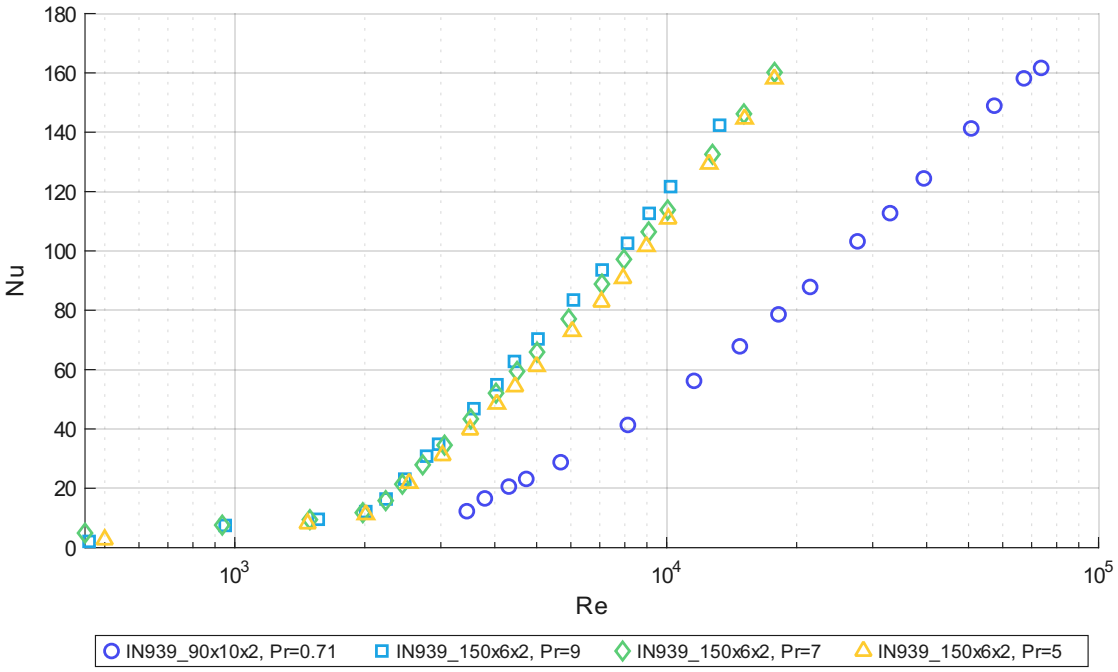

Figure 5.26: IN939_150x6x2 Nusselt number

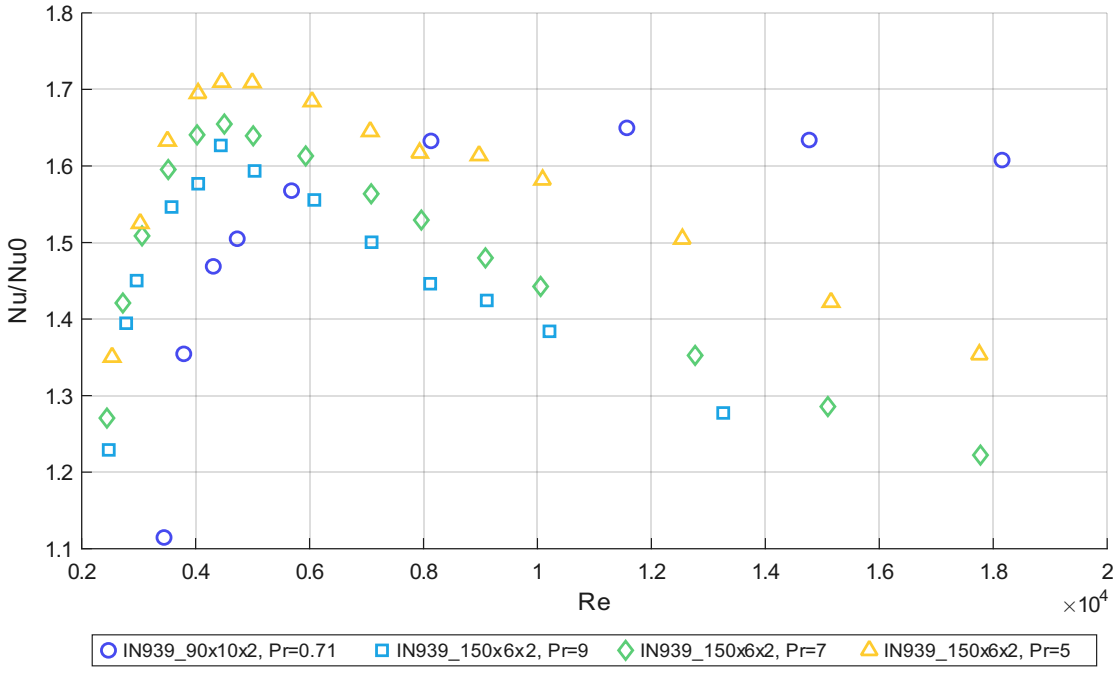

Figure 5.27: IN939_150x6x2 Nusselt enhancement

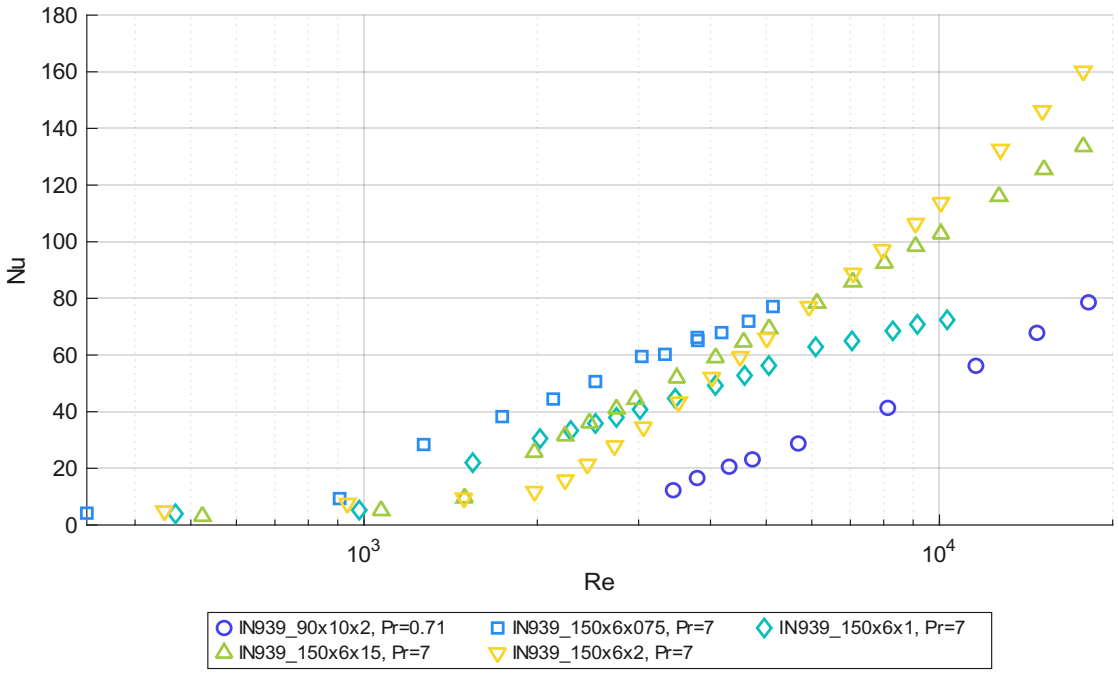

Figure 5.28: IN939 Nusselt number

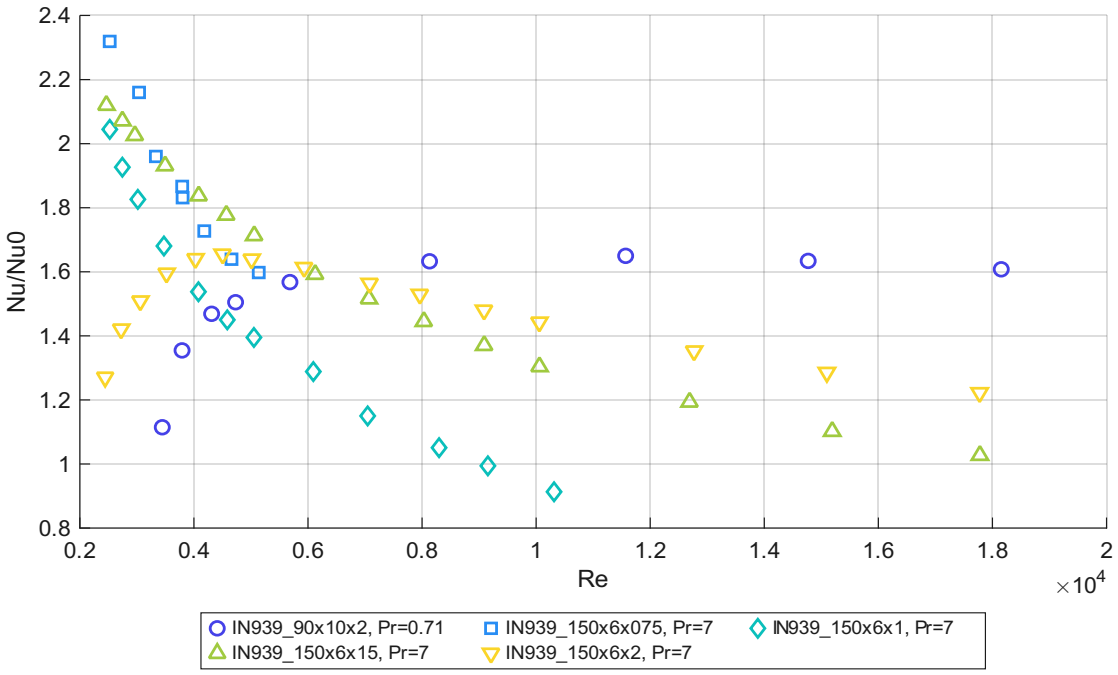

Figure 5.29: IN939 Nusselt enhancement

mm), that have only a decreasing enhancement trend, with the 2 mm test object that reaches the fully developed flow at higher Re.

5.3.4 Material effect

An interesting confront can be made between Aluminum TO1 and Inconel939 1.5mm: they have a similar relative roughness, but their metal conductivity is different by one order of magnitude.
The different conductivity of the solid affects the $Nu-Re$ gradient in turbulent flow (fig. 5.30): Aluminum test object has consistently a higher Nu, and the difference between the two TOs increases with Re.

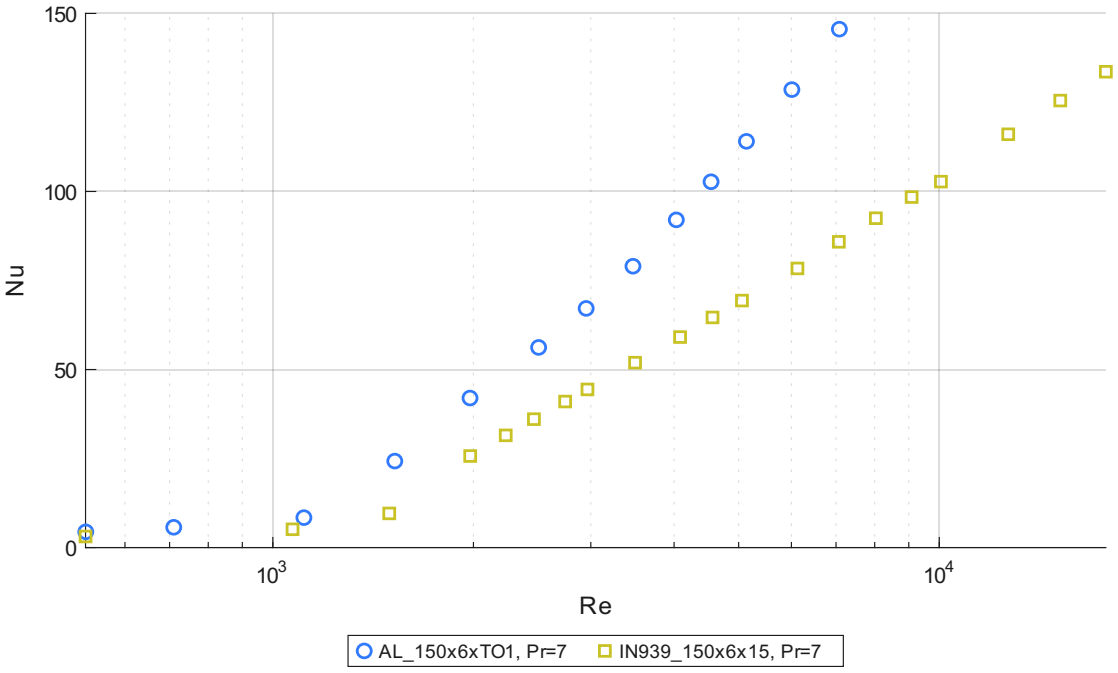

Figure 5.30: Material comparison, Nusselt number

When looking at the enhancement (fig. 5.31), the curves are almost parallel, which may be exclusively due to the thermal conductivity of the TOs: a different surface topology would have affected the flow behavior, which alters the Re effect on the Nu and the curves may not have been parallel between each other.

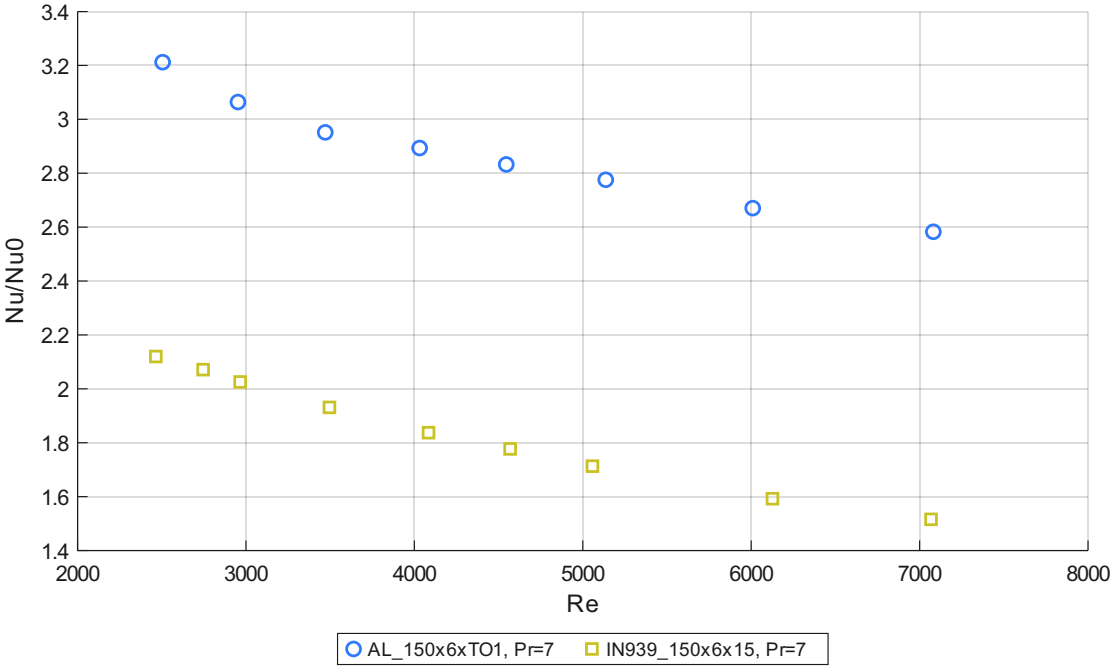

Figure 5.31: Material comparison, Nusselt enhancement

5.4 Local Nusselt analysis

An advantage of the new solver is the ability to evaluate the Nusselt number locally, where the PT100s are placed along the channel's wall. With this setup is possible to see where the transition from laminar to turbulent happens.

5.4.1 Aluminum

In this subsection the focus will be on the TO5 test object at $Pr = 7$.
In laminar flow the heat transfer coefficient is really low. This is visible on figure 5.32, where the distance between water temperature (yellow) and internal wall temperature (blue) is almost $30°C$. The test object has negligible thermal gradient in radial direction, the external temperature (red) is the same as the internal one. When the flow is fully developed (fig. 5.34), the internal wall tends to the water's temperature. At $Re = 28500$ the electrical current in the test object exceeds 2000 A. This generates a lot of heat and it is visible in the graph as a radial thermal gradient. For an aluminum test object, this current causes the copper clamps on the sides to reach temperatures close to the safety limit of the rig.
In the transition region (fig. 5.33), is is clearly visible that the flow is laminar until $x = 60mm$, where the wall's temperature grows as seen in figure 5.32. From that

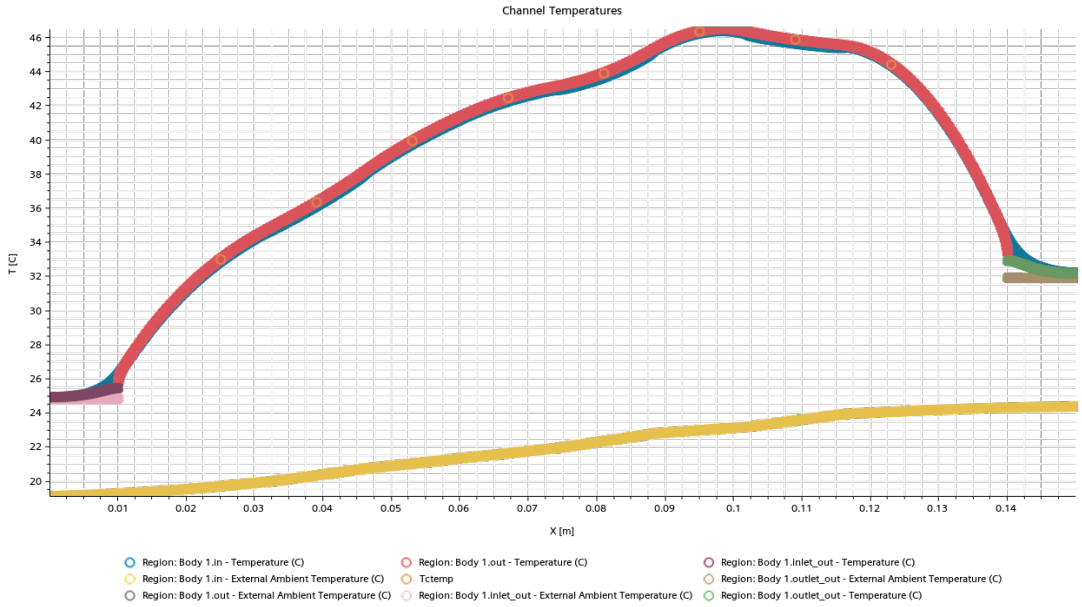

Figure 5.32: Aluminum TO5, $Pr = 7$, $Re = 550$, Channel temperatures

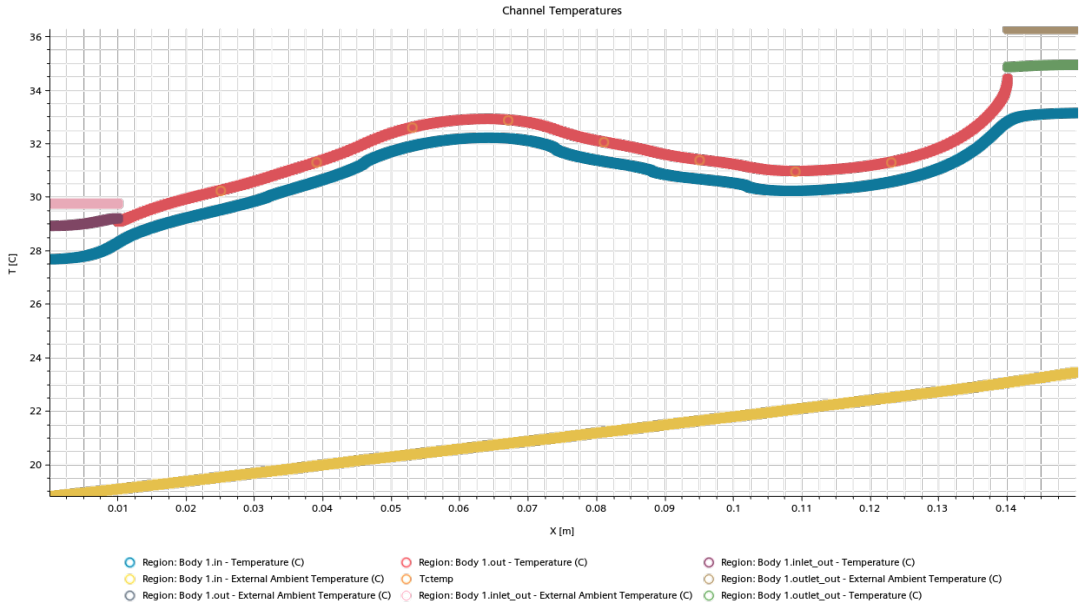

Figure 5.33: Aluminum TO5, $Pr = 7$, $Re = 3000$, Channel temperatures

point, the wall temperature drops because of the better heat transfer properties of turbulent flow, and at the end of the channel reaches a trend similar to what can

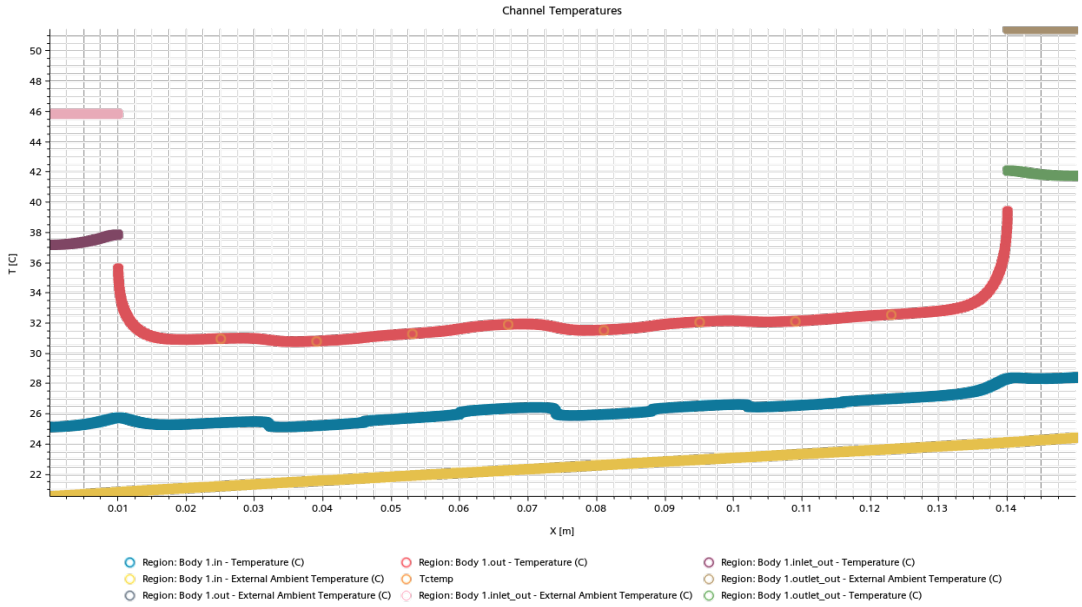

Figure 5.34: Aluminum TO5, $Pr = 7$, $Re = 28500$, Channel temperatures

be seen in figure 5.34.
Calculating the local Nu at the PT100s' positions, there are two distinct behaviors:

- *Laminar flow*: the Nu is decreasing exponentially (linear in the log plot on the right, figure 5.35);
- *Turbulent flow*: the Nu increases almost linearly.

From figure 5.35 on the right the distinction between laminar and turbulent flow is evident: a gap is present in the range $10 \leq Nu \leq 30$, indicating how much better turbulent flow is for heat transfer. In the middle of the gap there are the points in transition, where a part of the channel is laminar and a part is becoming turbulent.

5.4.2 Inconel 939

The test object chosen for local Nusselt analysis was Inconel 939 1.5mm. The behavior in the center of the channel is similar to what was seen with the Aluminum (figure 5.32), so it is not reported again.
However, when the flow becomes fully turbulent, the temperature plot (figure 5.36) is different from the Aluminum test on the copper clamps: the current is $I \approx 300A$, ten times lower than what was achieved with the TO5. When the current is this low there is not enough heat generated in the clamps, so their temperature stays lower than the rest of the TO. Inconel is also less thermal conductive, and this

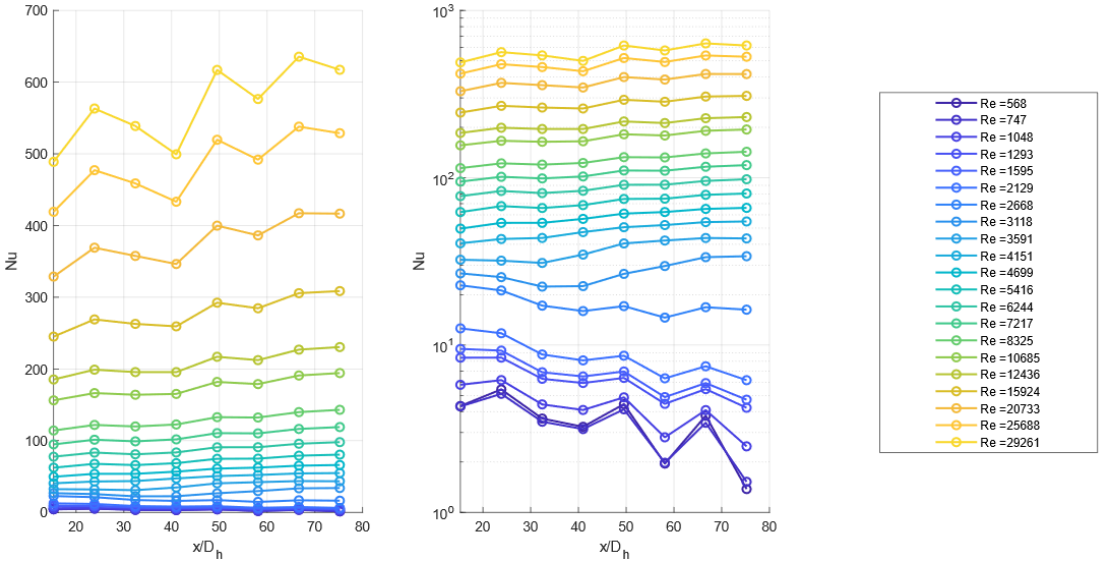

Figure 5.35: Aluminum TO5, $Pr = 7$, Local Nusselt number

is visible in the middle of the plot: the external wall reaches temperatures close to $65°C$ while the inner wall is at $T_{wall} \approx 33°C$. For this reason, the temperature gradient in radial direction is approximately 5 times stronger than the Aluminum's one.

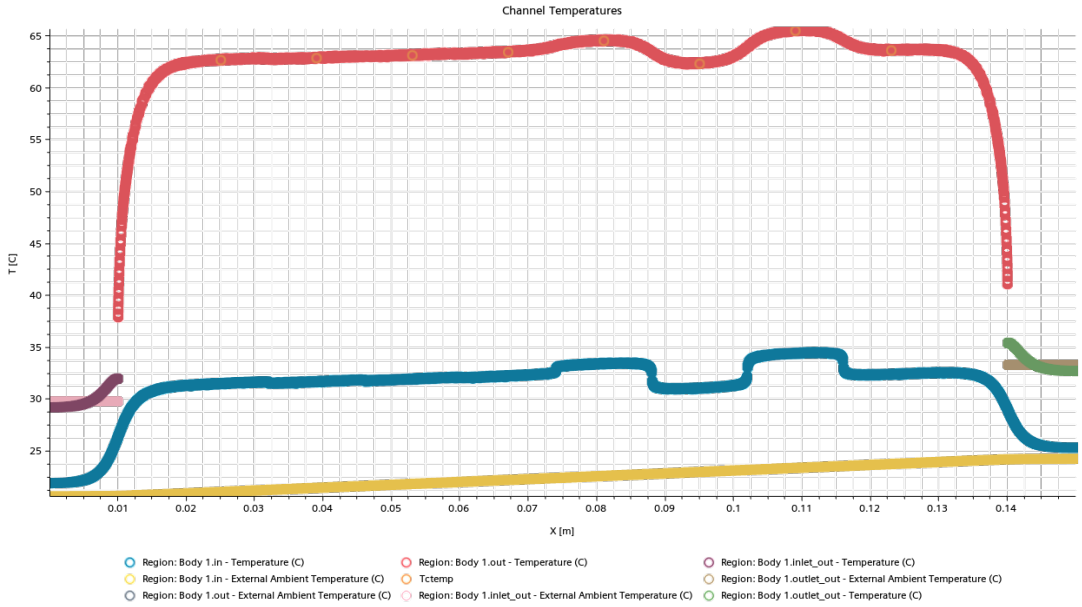

Figure 5.36: Inconel 939 1.5mm, $Pr = 7$, $Re = 18000$, Channel temperatures

On figure 5.37 the local Nusselt number for the test object is presented. The same conclusions of Aluminum TO apply, but in this case there are less points in the laminar region due to the earlier transition to turbulent. Even at high Re there is an initial drop in local Nusselt. This behavior will be discussed in the conclusion as possible limitation of the test procedure.

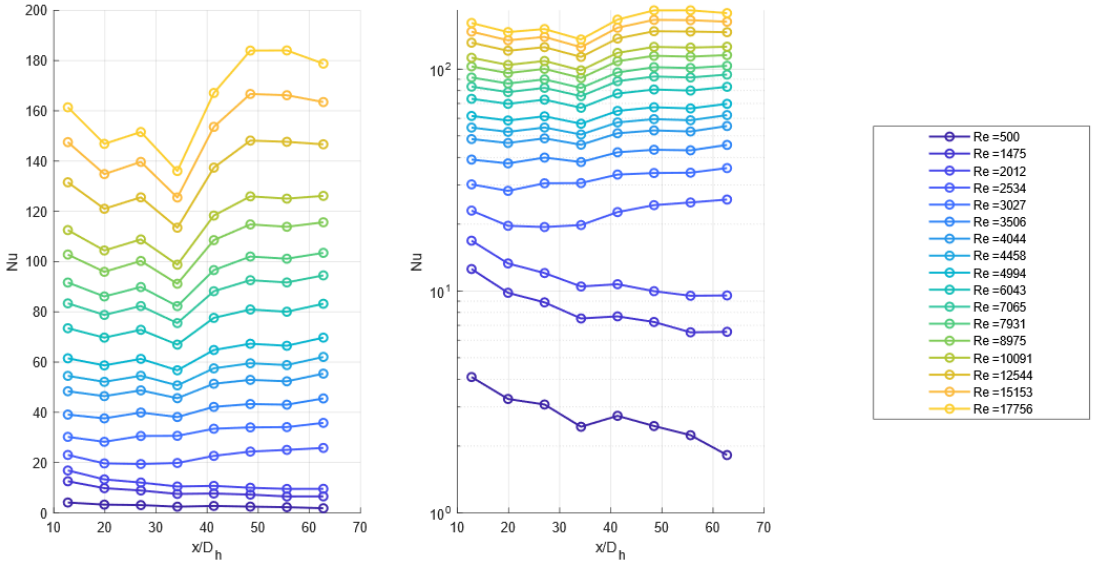

Figure 5.37: Inconel 939 1.5mm, $Pr = 7$, Local Nusselt number

Chapter 6

Conclusions

Friction factor

Confronting all the TOs, the AL_TO1 and the IN939_15 have almost the same relative roughness. In the turbulent region they both reach a Darcy friction factor close to 0.15, meaning that R_z is a valuable parameter to describe the AM roughness pattern for these types of results.
The Stainless Steel test objects had some manufacturing defects that caused the results to shift away from the expected result, therefore their results for the Darcy test were not trusted. A new test object manufacturing and testing is required to draw conclusions for this material.
The Aluminum and Inconel test objects behave consistently in the turbulent region, but in laminar flow they are not following Poiseuille's flow line $f_d = 64/Re$. Probably the hydraulic diameter estimation at the inlet/outlet is not reflecting the channel's internal geometry, but this cannot be said without cutting open the test object and scanning the inside. Another possible cause could be the low sensibility of the pressure transducers: their range is 20 bars and uncertainty is $\sim 1\%$, so they are not suited for measuring pressures as low as 0.02 bars. The same concern can be raised for the mass flow meter; a smaller Coriolis can be used in the first measurement points.

General heat transfer

Generally, the Nusselt number is growing with a different rate depending on the material's thermal conductivity and the relative roughness. Valuable data can be seen on the enhancement plots, especially on Inconel 2mm (fig. 5.27). In low turbulence there is a steep growth in enhancement until a maximum. Then, the improvement decreases until it reaches a plateau for high turbulence. Due to the rig's limitation, for most of the test objects this was not visible entirely:

low-roughness TOs only had the enhancement growth, and high-roughness ones had only the decreasing and plateau region due to their early transition.
The Stainless Steel results cannot be trusted due to the behavior at high Re: the htc tends to infinite and the numerical model breaks. This issue is not appearing on Inconel test objects, which have the same thermal conductivity. Another test object is needed to compare Inconel against Stainless Steel with the same relative roughness.
Aluminum test objects have a strong Pr effect, almost the same found on smooth channels by Dittus-Boelter. An initial correlation is found by collapsing the curves, using a least-square method with Re and Pr as free variables. The TO5 result has been used, including the air rig data:

$$Nu_{Al} = 0.069 \cdot Re^{1.201} \cdot Pr^{0.655} \tag{6.1}$$

This is significantly different from Dittus-Boelter (eq. 2.12), with both Re and Pr having a higher influence on Nu.
The same curve fit has been calculated for Inconel 939 2mm, the other TO with test data from the air rig:

$$Nu_{IN939} = 0.004 \cdot Re^{1.035} \cdot Pr^{0.375} \tag{6.2}$$

A less conductive material has a lower Pr effect, almost equal to the smooth channel correlation. These results are a good starting point, but for obtaining a final experimental correlation more data is needed, at wider Pr and Re ranges.

Local heat transfer

In all tests it was seen that, from inlet to outlet, the Nusselt is decreasing exponentially when the flow is laminar and increasing linearly when it is turbulent. This test can be used for determining the inlet notch effect, but with this experimental setup the first point was at $x/d_h > 10$, while Mills (figure 2.13) found that the effects at that distance are already negligible for the tests' Re.
Both local results have an inferior heat transfer performance in the center of the channel (4th PT100). This may be a numerical error created by how the solver compensates for overshooting the Nu in the previous points. This issue can be neglected for the global Nu result, which is an arithmetic mean of the points plotted in the local results. This mean compensates the oscillating result.

6.1 Future works

This experimental setup is still a new method for obtaining Nusselt number results on these channels. There are many defects and things that needs optimization, both on the numerical model and on the physical setup.
The experimental setup may have problems on the data acquisition, specifically:

- Wall PT100s may not have the proper contact with the test object. An improvement may be a spring-action to keep the pressure and/or the use of a thermal adhesive. Their circumferential positioning is also critical: as seen in the Nusselt along x results (fig. 5.35), the local htc varies greatly around the circumference due to a small difference in wall thickness. This has to be taken into account for gathering better local results;

- Instead of using PT100s on contact with the external wall, the possibility of observing a temperature map of the test object with an infrared camera will be explored in the future: this allows to have hundreds of temperature points on the surface, and at the same time can be used to evaluate the thermal notch effect;

- Pressure measurements are taken with absolute pressure transducers. The needed measurement is a ΔP, so the use of a dedicated differential pressure transducer halves the instrument uncertainty. For low Re measurements, another sensor with lower range and therefore higher precision can be used;

- The Coriolis mass flow meter is heavily affected by the pump's vibration. A better option would be installing it on the outlet where it is the furthest away from the pump. A smaller range Coriolis can be also used for low Re measures to improve precision.

The solver can be sped up and made more robust by implementing numerical methods on the iterator, such as Newton-Rhapson, for finding the final htc distribution. Another improvement can be made on the Nusselt - x result: interpolating the temperature measurements on the wall with a least-square curve fit can smooth out Nu peeks and valleys seen in figures 5.35 and 5.37.

Appendix A

List of test objects and relative roughness

In table A.1 are listed all the test objects evaluated for this thesis project. The IN939 parts are manufactured internally in Siemens Energy AM Workshop, while the stainless steel and aluminum ones were produced externally. All test objects are 150mm long, because there was not enough time during the project to test the 90mm ones, with the exception of the validation channel. From the original print, the test objects are machined externally, leaving only the inlet face as it was after the printing process.

Name	**Material**	D_h **[mm]**
AL_90x10x2	Aluminum (smooth)	2.1183
AL_150x6xTO1	Aluminum	0.6885
AL_150x6xTO5	Aluminum	1.6353
IN939_150x6x075	IN939	0.7849
IN939_150x6x1	IN939	1.1108
IN939_150x6x15	IN939	1.5648
IN939_150x6x2	IN939	1.9605
SS_150x6x2	Stainless steel	1.9497
SS_150x6x3	Stainless steel	2.8127

Table A.1: Test objects list

The hydraulic diameter has been estimated using microscope images of the inlet and outlet channels, as seen in Appendix B.
With the help of a profilometer, the roughness parameter for each material were obtained and reported on table A.2.

Material	**Ra** $[\mu m]$	**Ra - st.dev.** $[\mu m]$	**Rz** $[\mu m]$	**Rz - st.dev.** $[\mu m]$
Aluminum	4.97	2.29	43.18	13.22
Stainles Steel	10.08	0.96	66.83	7.48
Inconel 939	15.89	3.42	96.8	20.01

Table A.2: Roughness measurements

The relative roughness for each channel is simply obtained using the peak to valley roughness R_z:

$$\varepsilon = \frac{R_z}{d_h} \tag{A.1}$$

Name	**Relative Roughness** ε
AL_150x6xTO1	0.0627
AL_150x6xTO5	0.0264
IN939_150x6x075	0.1233
IN939_150x6x1	0.0871
IN939_150x6x15	0.0619
IN939_150x6x2	0.0494
SS_150x6x2	0.0343
SS_150x6x3	0.0234

Table A.3: Relative roughness of each test object

Appendix B

Evaluation of the hydraulic diameter

The most critical variable of the Darcy test is the *hydraulic diameter* of the TO. It is defined as:

$$d_h = \frac{4A}{P} \tag{B.1}$$

Where A is the cross-section area and P the perimeter.
In a test channel, d_h varies a lot due to the relative roughness, especially in the smaller test objects where this value is the highest. The geometry is important because the Darcy friction factor depends on it with an exponent of $(d_h)^5$ (eq. 4.6). Riccardo Pagani [35], during his thesis work on the qSSHT Air rig, developed a MATLAB script to calculate graphically d_h using microscope images of the TO's inlet and outlet.

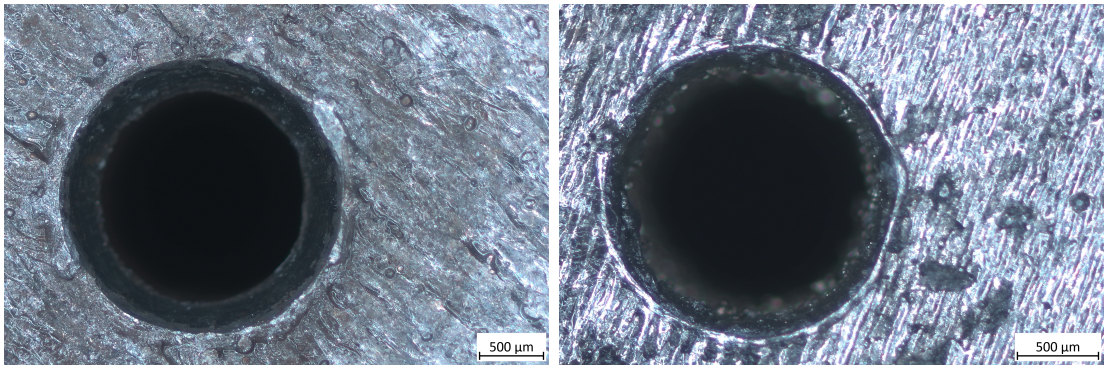

Figure B.1: Microscope pictures of the TO's inlets.
Left: AL TO5; Right: IN939 1.5

The procedure is simple, but it has to be precisely followed to have consistent

results that can be compared between each other:

1. Align the TO to the microscope's lens and take pictures of the inlet and outlet at different focus/lighting settings. Print the scale in the image as seen in figure B.1;

2. Run the MATLAB code, selecting a certain number of points around the inner diameter to get the internal channel shape. It is usually the smallest ring on focus in the image;

3. The code interpolates with a spline 23 points. This feature is done to reduce the number of points used for extracting the channel geometry. If there are too many points a fractal is created: if the points tend to infinite, the perimeter tends to infinite as well and the area tends to zero;

4. This procedure is followed for both the inlet and the outlet, also more times per image to reduce operator uncertainty. Due to the machining process, the outlet measurement is often discarded because it gets deformed by the lathe's centre.

5. At the end, an average of all the measurements is done, and these values are used for the Darcy and Nusselt evaluations.

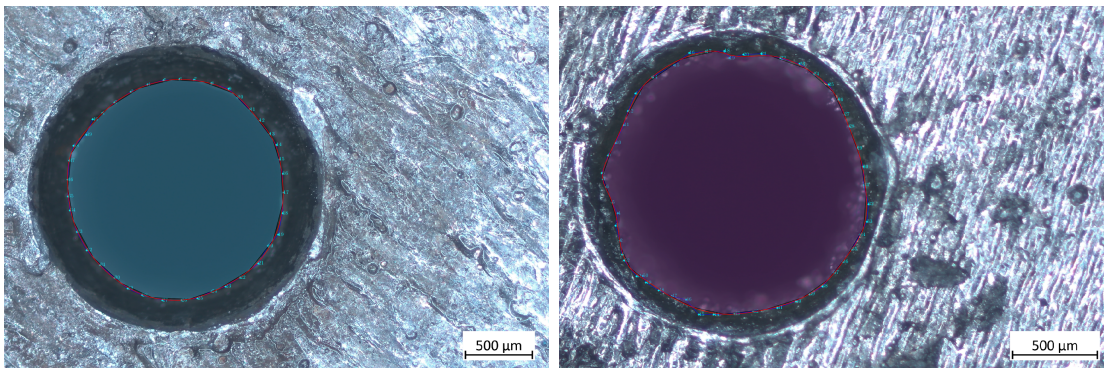

Figure B.2: Area and perimeter used for calculating d_h.
Left: AL TO5; Right: IN939 1.5

On figure B.2 there are some examples of hydraulic diameters. The Aluminum TO has a smaller diameter than the face's edge, because the machining process created a dent that did not exist at the end of the print.

Bibliography

[1] D.E. Dimla, M. Camilotto, and F. Miani. «Design and optimisation of conformal cooling channels in injection moulding tools». In: *Journal of Materials Processing Technology* 164-165 (2005). AMPT/AMME05 Part 2, pp. 1294–1300. ISSN: 0924-0136. DOI: https://doi.org/10.1016/j.jmatprotec.2005.02.162. URL: https://www.sciencedirect.com/science/article/pii/S0924013605001391 (cit. on p. 1).

[2] Yu Wang, Kai-Min Yu, Charlie C.L. Wang, and Yunbo Zhang. «Automatic design of conformal cooling circuits for rapid tooling». In: *Computer-Aided Design* 43.8 (2011), pp. 1001–1010. ISSN: 0010-4485. DOI: https://doi.org/10.1016/j.cad.2011.04.011. URL: https://www.sciencedirect.com/science/article/pii/S0010448511001060 (cit. on p. 2).

[3] Gotthlif Heinrich Ludwig Hagen. *Über den einfluss der temperatur auf die bewegung des wassers in röhren–*. Druckerei der Königl. akademie der wissenschaften, 1854 (cit. on p. 4).

[4] Henry Darcy. *Recherches expérimentales relatives au mouvement de l'eau dans les tuyaux*. Vol. 2. Mallet-Bachelier, 1857 (cit. on pp. 4, 14).

[5] Thomas Edward Stanton. «The mechanical viscosity of fluids». In: *Proceedings of the Royal Society of London. Series A, Containing Papers of a Mathematical and Physical Character* 85.579 (1911), pp. 366–376 (cit. on p. 4).

[6] Johann Nikuradse et al. «Laws of flow in rough pipes». In: (1950) (cit. on pp. 4, 9).

[7] Th Von Karman. «Turbulence and skin friction». In: *Journal of the Aeronautical Sciences* 1.1 (1934), pp. 1–20 (cit. on p. 4).

[8] Cyril F Colebrook and Curt M White. «Experiments with fluid friction in roughened pipes». In: *Proceedings of the Royal Society of London. Series A-Mathematical and Physical Sciences* 161.906 (1937), pp. 367–381 (cit. on pp. 4, 9, 15, 43, 46).

[9] Nian-Sheng Cheng. «Formulas for friction factor in transitional regimes». In: *Journal of Hydraulic Engineering* 134.9 (2008), pp. 1357–1362 (cit. on p. 4).

[10] Lewis F Moody. «Friction factors for pipe flow». In: *Transactions of the American Society of mechanical engineers* 66.8 (1944), pp. 671–678 (cit. on pp. 4, 15).

[11] Hermann Schlichting. *Experimental investigation of the problem of surface roughness*. 823. National Advisory Commitee for Aeronautics, 1937 (cit. on p. 5).

[12] Kun Huang, J. Wan, C. Chen, Y.Q. Li, D. Mao, and M.Y. Zhang. «Experimental investigation on friction factor in pipes with large roughness». In: *Experimental Thermal and Fluid Science* 50 (Oct. 2013), pp. 147–153. DOI: 10.1016/j.expthermflusci.2013.06.002 (cit. on p. 5).

[13] Baomin Dai, Minxia Li, and Yitai Ma. «Effect of surface roughness on liquid friction and transition characteristics in micro- and mini-channels». In: *Applied Thermal Engineering* 67.1 (2014), pp. 283–293. ISSN: 1359-4311. DOI: https://doi.org/10.1016/j.applthermaleng.2014.03.028. URL: https://www.sciencedirect.com/science/article/pii/S1359431114002038 (cit. on p. 5).

[14] WF Cope. «The friction and heat transmission coefficients of rough pipes». In: *Proceedings of the Institution of Mechanical Engineers* 145.1 (1941), pp. 99–105 (cit. on p. 5).

[15] Duane F Dipprey and Rolf H Sabersky. «Heat and momentum transfer in smooth and rough tubes at various Prandtl numbers». In: *International Journal of Heat and Mass Transfer* 6.5 (1963), pp. 329–353 (cit. on p. 5).

[16] Gian Luca Morini. «Single-phase convective heat transfer in microchannels: a review of experimental results». In: *International journal of thermal sciences* 43.7 (2004), pp. 631–651 (cit. on p. 6).

[17] Kathryn L Kirsch and Karen A Thole. «Heat transfer and pressure loss measurements in additively manufactured wavy microchannels». In: *Journal of turbomachinery* 139.1 (2017), p. 011007 (cit. on p. 6).

[18] Curtis K Stimpson, Jacob C Snyder, Karen A Thole, and Dominic Mongillo. «Roughness effects on flow and heat transfer for additively manufactured channels». In: *Journal of Turbomachinery* 138.5 (2016), p. 051008 (cit. on p. 6).

[19] SA Weaver, MD Barringer, and KA Thole. «Micro channels with manufacturing roughness levels». In: *Turbo Expo: Power for Land, Sea, and Air*. Vol. 43994. 2010, pp. 413–422 (cit. on pp. 6, 7).

[20] Andrew Townsend, Nicola Senin, Liam Blunt, RK Leach, and JS Taylor. «Surface texture metrology for metal additive manufacturing: a review». In: *Precision Engineering* 46 (2016), pp. 34–47 (cit. on p. 6).

[21] Sangil Han, Ferdinando Salvatore, Joël Rech, and Julien Bajolet. «Abrasive flow machining (AFM) finishing of conformal cooling channels created by selective laser melting (SLM)». In: *Precision Engineering* 64 (2020), pp. 20–33 (cit. on p. 6).

[22] Mohammadreza Kadivar, David Tormey, and Gerard McGranaghan. «A review on turbulent flow over rough surfaces: Fundamentals and theories». In: *International Journal of Thermofluids* 10 (2021), p. 100077 (cit. on pp. 8, 9).

[23] Xinyu Yang, Richard Barrett, Noel Harrison, and Sean Leen. «A physically-based structure-property model for additively manufactured Ti-6Al-4V». In: *Materials & Design* 205 (Apr. 2021), p. 109709. DOI: 10.1016/j.matdes.2021.109709 (cit. on p. 11).

[24] Sara Sendino, Silvia Martinez, Fernando Lartategui, Javier Diaz, Aitzol Lamikiz, and Eneko Ukar. «SURFACE ROUGHNESS DEPENDANT FACTORS IN METAL POWDER BED FUSION PROCESSES». In: () (cit. on p. 11).

[25] John Anderson. *Fundamentals of Aerodynamics*. McGraw hill, 2011 (cit. on p. 12).

[26] Frank P Incropera, David P DeWitt, Theodore L Bergman, Adrienne S Lavine, et al. *Fundamentals of heat and mass transfer*. Vol. 6. Wiley New York, 1996 (cit. on pp. 14, 16, 17).

[27] *Moody diagram, CC BY-SA 4.0,* URL: https://commons.wikimedia.org/w/index.php?curid=52681200 (cit. on p. 15).

[28] Isaak E Idelchik. *Handbook of hydraulic resistance*. 1986 (cit. on pp. 15, 16).

[29] Volker Gnielinski. «Neue Gleichungen für den Wärme-und den Stoffübergang in turbulent durchströmten Rohren und Kanälen». In: *Forschung im Ingenieurwesen A* 41 (1975), pp. 8–16 (cit. on pp. 18, 43, 44, 50).

[30] AF Mills. «Experimental investigation of turbulent heat transfer in the entrance region of a circular conduit». In: *Journal of Mechanical Engineering Science* 4.1 (1962), pp. 63–77 (cit. on pp. 19, 20).

[31] International Electrotechnical Commission et al. «IEC60751: Industrial platinum resistance thermometer sensors, 1.1983». In: *Website: http://www. iec. ch* () (cit. on p. 27).

[32] International Electrotechnical Commission et al. «IEC 60584-1: 2013—Thermocouples—Part 1: EMF Specifications and Tolerances». In: *International Electrotechnical Commission: Geneva, Switzerland* (2013) (cit. on p. 27).

[33] IFCC BIPM, ILAC IFCC, IUPAC ISO, and OIML IUPAP. «Evaluation of measurement data—guide to the expression of uncertainty in measurement, JCGM 100: 2008 GUM 1995 with minor corrections». In: *Joint Committee for Guides in Metrology* 98 (2008) (cit. on p. 34).

[34] Hugh W Coleman and W Glenn Steele. *Experimentation, validation, and uncertainty analysis for engineers*. John Wiley & Sons, 2018 (cit. on p. 35).

[35] Riccardo Pagani. «Experimental Analysis of the Thermal and Hydraulic Performance in Straight and Complex Additively Manufactured Mini-Channels». In: *Politecnico di Milano* (2022) (cit. on p. 75).

[36] Ian H. Bell, Jorrit Wronski, Sylvain Quoilin, and Vincent Lemort. «Pure and Pseudo-pure Fluid Thermophysical Property Evaluation and the Open-Source Thermophysical Property Library CoolProp». In: *Industrial & Engineering Chemistry Research* 53.6 (2014), pp. 2498–2508. DOI: 10.1021/ie4033999. eprint: http://pubs.acs.org/doi/pdf/10.1021/ie4033999. URL: http://pubs.acs.org/doi/abs/10.1021/ie4033999 (cit. on p. 39).

[37] Frank E Jones and Georgia L Harris. «ITS-90 density of water formulation for volumetric standards calibration». In: *Journal of research of the National Institute of Standards and Technology* 97.3 (1992), p. 335 (cit. on p. 39).